SAINT PETERSBURG STATE UNIVERSITY STUDIES IN PHYSICS

Maxim Trushin

Enhanced charge carrier thermoemission from the dislocation-related electronic states in silicon

Saint Petersburg | 2014

The series *Saint Petersburg State University Studies in Physics* presents final results of research carried out in postgraduate physical programs at St. Petersburg State University. Most of this research is here presented after publication in leading scientific journals.

The supervisors of these works are well-known scholars of St. Petersburg State University and invited foreign researchers. The material of each book has been considered by a permanent editorial board as well as a special international commission comprised of well-known Russian and international experts in their respective fields of study.

Printed in Russia by St. Petersburg University Press 11/21 6th Line, St. Petersburg, 199004

ABSTRACT

Trushin, Maxim

Enhanced charge carrier thermoemission from the dislocation-related electronic states in silicon

Saint Petersburg: Saint Petersburg State University, 2014, 45 p. (+included articles) Saint Petersburg State University Studies in Physics, Vol. 3

This work demonstrates the original results of theoretical calculations and experimental investigations of a new dislocation-related phenomenon that is the enhancement of carrier thermoemission from the local electronic core states of dislocations in Si band gap.

Performed theoretical calculations have shown that the interaction of the attractive deformation potential of dislocations with the external electric field gives rise to the thermoemission enhancement from the dislocation core states similar to the Poole-Frenkel effect originally proposed for attractive Coulomb potential but with the noticeably larger coefficient values. Detailed calculations were made for hole and electron emission from the states of screw and 60º dislocations to the valence and to the conduction band of Si, respectively. It follows from the calculations that the corresponding values of Pool-Frenkel coefficient depend strongly on dislocations type, density and on the Burgers vector orientation relative to the electric field direction. The theory predicts also the enhancement of the carrier thermoemission due to the own electric field of dislocation line charge, giving rise to the peculiar behavior of the signal detected with deep level transient spectroscopy (DLTS), in particular to the broadening of DLTS peak with the increase of the occupancy of dislocation-related states.

In order to check the key statements of the theoretical calculations the unique samples with regular dislocation network produced by Si wafers direct bonding were chosen as the model objects and were extensively investigated by means of various space charge spectroscopy techniques. The study has revealed the presence of shallow dislocation-related states near the top of valence band and the bottom of conduction band, respectively, exhibiting the thermoemission enhancement both in external electric field following the Poole-Frenkel law and with increase of the state occupancy degree. A good quantitative agreement established between the theoretical and experimental data allows to conclude that the reduction of thermoemission barrier with the increase of the trap occupancy degree and in external electric field may serve as a fingerprint of the electronic states located in the proximate vicinity of the dislocation core.

Keywords: dislocation network, Poole-Frenkel effect, deformation potential, shallow states of dislocations, band-like states, DLTS.

Supervisor Professor Oleg Vyvenko
Solid State Electronics Department
Faculty of Physics
St. Petersburg State University, Russia

Opponents

Professor Alexander Shulakov (Chairman)
Head of Solid State Electronics Department
Faculty of Physics
St. Petersburg State University, Russia

Professor Vadim Agekyan
Head of Solid State Physics Department
Faculty of Physics
St. Petersburg State University, Russia

Professor Ivan Ignatiev
Solid State Physics Department
Faculty of Physics
St. Petersburg State University, Russia

Professor Nickolay Bagraev
Experimental Physics Department
Institute of Physics, Nanotechnology and Telecommunications
St. Petersburg State Polytechnical University, Russia

Dr. Sc. Nickolay Sobolev
Head of the research group "Defect Engineering and Semiconductor Technology"
Laboratory of Semiconductor Devices Physics
Ioffe Physical Technical Institute, Russia

Professor Martin Kittler
Head of IHP/BTU Joint Lab
Brandenburgischer Technischer Universität
Cottbus-Senftenberg, Germany

Professor Michael Seibt
Head of the research group "Electronic and Atomic Structure of Defects and Interfaces"
IV. Physikalisches Institut der Georg-August Universität
Göttingen, Germany

ACKNOWLEDGEMENTS

First of all I would like to express my sincere gratitude to Prof. O. Vyvenko for his continuous encouragement and guidance throughout the research work, for his constant support and his openness for discussions.

I am deeply grateful to Prof. M. Kittler for giving me the opportunity to study and to perform the experiments in Brandenburg University of Technology.

My special thanks to SOITEC Company and especially to Dr. O. Kononchuk for kindly providing the bonded samples for the investigations.

I would like to acknowledge the Interdisciplinary Resource Center for Nanotechnology at St. Petersburg State University and personally Dr. V. Vdovin for performing the TEM measurements.

Finally, I wish to express my gratitude to all my colleagues and friends for the nice working atmosphere and the cordial spirit which we have in our group. This made my return to Saint-Petersburg really pleasant.

CONTENTS

LIST OF INCLUDED ARTICLES

PI. M. Trushin, O. Vyvenko, T. Mchedlidze, O. Kononchuk, M. Kittler, “Electronic States of Oxygen-free Dislocation Networks Produced by Direct Bonding of Silicon Wafers”, *Solid State Phenomena 156-158, p. 283, 2010* (Web of Science, Scopus) **6 pages**

PII. M. Trushin, O. Vyvenko, V. Vdovin, and M. Kittler, "Giant Poole-Frenkel effect for the shallow dislocation-related hole traps in silicon", *Journal of Physics: Conference Series 281, p. 012009, 2011* (Scopus) **10 pages**

PIII. I. Kolevatov, M. Trushin, O. Vyvenko, M. Kittler, O. Kononchuk, “Energetic spectra of dislocation networks produced by hydrophilic bonding of silicon wafers”, *Phys. Status Solidi C 10, p. 20, 2013* (Web of Science, Scopus) **4 pages**

PIV. M. Trushin, O. Vyvenko, "Impact of Electric Field on Thermoemission of Carriers from Shallow Dislocation-Related Electronic States", *Solid State Phenomena 205-206, p. 299, 2014* (Web of Science, Scopus) **6 pages**

OTHER PUBLICATIONS

AI O. Vyvenko, M. Kittler, W. Seifert, M. Trushin, Recombination activity and electrical levels of "clean" and copper contaminated dislocations in p-type Si. *Physica Status Solidi C* **2**, 1852–1858 (2005).

AII O. Vyvenko, N. Bazlov, M. Trushin, A. Nadolinski, M. Seibt, W.Schröter, G. Hahn, Impact of Hydrogenation on Electrical Properties of $NiSi_2$ Precipitates in Silicon. *Solid State Phenomena* **108-109**, 279 (2005).

AIII M. Trushin, O. Vyvenko, Electrical levels of nanoscale $NiSi_2$ precipitates in silicon band gap. *Physica Status Solidi C* **4**, 3056–3060 (2007).

AIV M. Trushin, O. Vyvenko, M. Seibt, Impact of $NiSi_2$ precipitates electronic structure on the minority carrier lifetime in n- and p- type silicon. *Solid State Phenomena* **131-133**, 155-160 (2008).

AV N. Bazlov, O. Vyvenko, A. Bondarenko, M. Trushin, A. Novikov, A. Vinogradov, M. Brzhezinskaya, R. Ovsyannikov, Capacitance Transient X-ray Absorption Spectroscopy of semiconducting structures. *Superlattices and Microstructures* **45**, 190-199 (2009).

AVI T. Mchedlidze, T. Wilhelm, T. Arguirov, M. Trushin, M. Reiche, M. Kittler, Correlation of electrical and luminescence properties of a dislocation network with its microscopic structure. *Physica Status Solidi C* **6**, 1817 (2009).

AVII W. Seifert, O. Vyvenko, T. Arguirov, A. Erko, M. Kittler, C. Rudolf, M. Salome, M. Trushin, I. Zizak, Synchrotron microscopy and spectroscopy for analysis of crystal defects in silicon. *Physica Status Solidi C* **6**, 765– 771 (2009).

AVIII W. Seifert, O. Vyvenko, T. Arguirov, M. Kittler, M. Salome, M. Seibt, M. Trushin, Synchrotron-based investigation of iron precipitation in multicrystalline silicon. *Superlattices and Microstructures* **45**, 168-176 (2009).

AIX M. Trushin, O. Vyvenko, W. Seifert, G. Jia, M. Kittler, Iron–oxygen interaction in silicon: A combined XBIC/XRF-EBIC-DLTS study of precipitation and complex building. *Physica B* **404**, 4645–4648 (2009).

AX M. Trushin, O. Vyvenko, W. Seifert, M. Kittler, I. Zizak, A. Erko, M. Seibt, C. Rudolf, Combined XBIC/μ-XRF/μ-XAS/DLTS investigation of chemical character and electrical properties of Cu and Ni precipitates in silicon. *Physica Status Solidi C* **6**, 1868– 1873 (2009).

AXI T. Mchedlidze, O. Kononchuk, T. Arguirov, M. Trushin, M. Reiche, M. Kittler, Determination of the Origin of Dislocation Related Luminescence from Silicon Using Regular Dislocation Networks. *Solid State Phenomena* **156-158**, 567-572 (2010).

AXII M. Trushin, W. Seifert, O. Vyvenko, J. Bauer, G. Martinez-Criado, M. Salome, M. Kittler, XBIC/μ-XRF/μ-XAS analysis of metals precipitation in block-cast solar silicon. *Nuclear Instruments and Methods in Physics Research B* **268**, 254–258 (2010).

AXIII O. Vyvenko, T. Arguirov, W. Seifert, I. Zizak, M. Trushin, M. Kittler, Scanning X-ray excited optical luminescence microscopy of multi-crystalline silicon. *Physica Status Solidi A*, 207(8), 1940, (2010).

AXIV T. Mchedlidze, T. Arguirov, O. Kononchuk, M. Trushin, M. Kittler, Structures responsible for radiative and non-radiative recombination activity of dislocations in silicon. *Physica Status Solidi C* **8**, 991 (2011).

AXV M. Trushin, O. Vyvenko, T. Mchedlidze, M. Reiche, M. Kittler, Characterization of dislocation network produced by silicon direct wafer bonding by means of voltage dependent light beam induced current and capacitance of Schottky diode. *Physica Status Solidi C* **8**, 1371 (2011).

AXVI M. Trushin, O. Vyvenko, W. Seifert, A. Klossek, I. Zizak, M. Kittler, Scanning X-ray Excited Optical Luminescence Microscopy as a New Tool for the Analysis of Recombination Active Defects in Multi-Crystalline Silicon. *Solid State Phenomena* **178-179**, 301 (2011).

AXVII M. Trushin, T. Arguirov, M. Kittler, W. Seifert, A. Klossek, T. Bernhard, W. Gerlach-Blumenthal, A. Hansel, O. Tober, M. Schwabe, Combined Raman-DLTS investigations of n-type Cu–In–S absorber layers grown on Cu tape substrate (CISCuT). *Phys. Status Solidi A* **210(1)**, 222, (2013).

1. INTRODUCTION

1.1 Background and actualities

Dislocations are spatially extended, quasi one-dimensional defects embedded into the crystalline matrix. In semiconductors, the most interesting and important effects are coming from the electronic states introduced by dislocations into the semiconductor band gap [1].

It is widely accepted now that in silicon most of dislocations generated at temperatures above 700°C are screw and 60° dislocations of the glide set which are dissociated into Shockley partial dislocations bounding the intrinsic stacking fault [1-3]. For such dislocations theory predicts reconstructed core structure without dangling bonds so that no deep electronic states are introduced in the band gap of silicon. Nevertheless, deep localized electronic states may arise due to: (i) core reconstruction defects and (ii) impurity atoms segregated inside the dislocation core or in the strained region around the dislocation [1-3]. Unlike to the point-like defects, dislocation-induced defect states can be occupied by many electrons or holes, so they would have a decisive influence on the performance of various electronic devices [1]. For instance, deep dislocation-related states substantially restrict the efficiency of the cost-effective solar cells made from multicrystalline silicon which contains a lot of dislocations and grain boundaries (GB) [4].

Theoretical calculations have also predicted the existence of two shallow one-dimensional (1D) bands in Si band gap caused by the dislocation strain: an empty one E_{De} splitting down from the conduction band and the occupied one E_{Dh} splitting up from the valence band, respectively [2, 5, 6]. They are stretching along the whole dislocation line so that the later can be considered as a native "quantum wire" buried in the crystalline solid. Shallow 1D bands have been related with various physical phenomena like the enhanced conductance along the dislocation line [7-9] and the dislocation-related luminescence [10, 11]. These properties of dislocations might be utilized in microelectronics to produce the all-Si light emitter with 1,5 μm wavelength for on-chip interconnection and MOSFET transistor with high conductivity channel [9, 12-14].

Thus, the dislocations in silicon may be attributed both to "beneficial" and "detrimental" types of defects. All these facts have evidenced the barest necessity of a deeper knowledge about the dislocation-related gap states in silicon, with a particular emphasis on the determination of the properties and parameters of shallow 1D core states of dislocations.

1.2 Previous and related studies.

During the last few decades, dislocation-related electronic states in the band gap of silicon were intensively studied by means of various experimental methods [1, 10]. Thus, by application of deep level transient spectroscopy (DLTS) – the direct method designed for studying the electrically active defects in semiconductors [15] (see also paragraph 3.1) – a row of deep traps was detected in n- and p-type Si samples with dislocations introduced by macroscopic plastic deformation. These traps were identified with the point-defect clusters related with the dislocation motion (so-called A and B traps in n-type Si), with the point defects/impurities located in the dislocation core and in the clouds around

related probably with oxygen impurity atoms (C and F traps) and with the dangling bonds and other reconstruction defects in the dislocation core (D trap) [16-21]. The density of these traps was found to depend strongly on sample preparation conditions.

The main well-known features of the dislocation-related DLTS-signal are the broadening of the DLTS peaks as compared with the peak due to point-like defects and the logarithmic dependence of peaks magnitude on the refilling pulse duration t_p, whereas for the point-like defects this dependence follows exponential law [1, 2, 22, 23]. These characteristic features served as fingerprints of extended defects including dislocations.

Theoretical model developed to explain the broadened DLTS peaks describes the spectrum of the dislocation-related electronic states in terms of density of states *N(E)* spreading over some energy range $E_1 \leq E_i \leq E_2$ with a total number of states N_T [1, 16, 22, 24]. The two limiting cases of band-like and localized states were specified relative to the time τ_i which is the time needed to establish the electronic equilibrium at the defect, so that for "band-like" states holds $\tau_i \ll \tau_e, \tau_c$ (emission and capture time constant) whereas for "localized" states $\tau_i \gg \tau_e, \tau_c$. A simple criterion suggested by Schröter et al. [22] allows to distinguish between these states by DLTS measurements: as the carrier emission from the band-like states towards the permitted band occurs mainly from the upper filled levels owing to the fast inter-level transition rate, the corresponding DLTS peaks would shift towards the lower temperatures with increase of number of captured carriers (i.e. with the increase of t_p), whereas the localized states emit the charge carriers almost independently so that the corresponding DLTS peak position would remain at the same temperature. The localized behavior was established for the most of deep level traps observed in plastically deformed samples (A-D and F- DLTS lines) [1, 2], whereas band-like behavior – for the core-related states of the dislocation ring bounding the $NiSi_2$ nanoprecipitates [3, 25].

Logarithmic dependence of DLTS peak magnitude was related with the potential barrier $e\Phi$ arising around the dislocation line as a result of charge carriers capture, which slows down further capturing of charge carriers and finally limits the total equilibrium occupation of dislocation states so that the total density of electrons (or holes) captured per unit length of dislocation line usually cannot exceed ~2-5*10^6 cm^{-1} even if the total number of states is larger than this value [2].

The shallow dislocation-related states appeared to be a "tough nut" for the experimental investigations by means of DLTS method. In plastically deformed samples this failure was explained by the limited number of dislocations inside the space charge region (SCR) of Schottky diode and by the influence of electric field which forced the charge carriers to drift along the dislocations crossing the SCR without thermal activation towards the permission band [2]. During long period of time only the indirect evidences concerning these shallow bands were obtained from various physical experiments, such as dependence of the EBIC (electron-beam-induced current) contrast at dislocations on temperature and injection dose [26], microwave conductance [7, 8], electric-dipole spin resonance [10, 27], and electroluminescence [28]. The only experimental observation of 1D shallow states by means of DLTS method was carried out by Castaldini et al [29] on specially prepared samples with a regular array of parallel 60° dislocations. Consistent values for the energy positions of the edges of shallow 1D bands in Si band gap were obtained by various experimental methods as $E_C - E_{De} \approx E_{Dh} - E_V \approx$ 70-90 meV where E_C and E_V are conduction and valence band edges, respectively, and E_{De} and E_{Dh} – shallow band edges [2, 10, 29].

1.3 Aim of the work

The particular drawback of the theoretical models [1, 22] suggested so far to describe the dislocation-related states in Si band gap is that the emission process of charge carriers from these states was considered without taking into account the influence of the dislocation own charge, the dislocation deformation potential and their interaction with external electric field on the carrier emission. Meanwhile, few previous experiments have already indicated a certain influence of external electric field on the carrier emission suggesting thus that the field effects need to be treated more carefully in the theoretical modeling.

So, the first evidence of the electric field influence on the carrier emission from the deep dislocation-related states was reported by Kveder et al [17] already in 1982, who has pointed out on the reduction of the activation enthalpy with increase of the external electric field (however without specification of the initiating mechanism – phonon-assisted tunneling or Poole-Frenkel effect [30]) and later by Hedemann et al [23, 31, 32], suggesting that the Poole-Frenkel barrier lowering [33] for carrier thermoemission has to be taken into account in order to simulate correctly the shapes of the broadened DLTS peaks due to $NiSi_2$ nanoprecipitates. In their simulations, Hedemann et al [23] have described the Poole-Frenkel effect by adjusting an effective point charge q^* as a free parameter and found that an unusually high value of $q^* \approx 2.7$ has to be used in the simulations in order to achieve the satisfactory fit of the experimental spectra. Nevertheless, the strict and complete theoretical description of the field enhanced emission from the dislocation-related states was not developed by the authors and still lacking.

Thus, the subject of the present work is to develop a comprehensive theoretical model describing the emission of carriers from the dislocation-related levels towards the valence and conduction bands of Si, which would account for the impact of (i) the attractive deformation potential of dislocations, (ii) the repulsive Coulomb potential of a charged dislocations and (iii) the potential of external electric field. Further, to verify the main provisions of the suggested models by extensive experimental investigations using n- and p-type Si samples with regular dislocation network (DN) as the model test objects. Moreover, since such kind of structures may find a practical application in the novel microelectronic devices, all additional scientific information about their electrical properties are of the great importance [9, 13].

1.4 Main properties of dislocation networks

The most of previous investigations were performed on the samples where the dislocations were introduced by the plastic deformation method [1]. This way of dislocation generation is though technically simple, but is inappropriate for reproducible fabrication of dislocations regarding their type, location, state of decoration with impurities, etc. In order to overcome these difficulties, the application of Si wafer bonding technology appropriate for well-controllable and reproducible fabrication of dislocations was suggested [9].

Semiconductor wafer bonding generally refers to a process where two mirror-polished wafers with high degree of flatness, parallelism and smoothness adhere to each other at room temperature without application of any macroscopic gluing layer [34-36]. The

primary attractive forces at this stage are van der Waals forces, electrostatic Coulomb forces, capillary forces and hydrogen bridge bonds. During the high-temperature annealing (T>800 °C), these weak adhesion forces are replaced by the Si-Si covalent bonds [35]. The dislocation network is formed at the bonding interface in order to compensate the mutual misorientation (intentional or unintentional) between the wafers [37].

The structure of the DN depends strongly on the wafers surface orientation, for instance, bonding of two Si (100) wafers causes a Σ1 (100) small-angle grain boundary characterized by a square-like mesh of screw dislocations compensating the twist misorientation, whereas tilt misorientation is compensated by the periodic array of 60° dislocations [37]. The spacing D between the dislocations can be approximated by the simple relation $D \sim B/\sin(\alpha)$, where α is the twist α_{TW} or tilt α_{TI} misorientation angle and B is the Burgers vector of the dislocations. Thus, spacing D ~ 10 nm is expected for a misorientation of about 2° and D ~ 1 μm for a very small misorientation of only 0.02°. By application of appropriate thinning procedure (mechanical polishing, SmartCut process, selective oxidation etc.), DN could be placed at the required depth below the surface, even less than 100 nm [38].

A big difference in dislocation core structure was reported [39] for the screw dislocations at the bonding interfaces produced with the twist angle below and above the critical one of about ~3-4°. For $\alpha_{TW} < 3°$ the screw dislocations composing the DN were found to be dissociated into partials – similar to the dislocations in Si bulk [1, 2], with the stacking fault width gradually decreasing with α_{TW}. Finally, for $\alpha_{TW}>4°$, the stacking fault width becomes smaller than typical dislocation core radius, i.e. less than 1 nm, resulting in a transformation of the "screw dislocation" to the "interfacial dislocation" with completely different core structure [39]. Nevertheless, even restricting the twist angle by 3°, the line density of screw dislocations in DNs could reach the value of 10^6 cm^{-1} and that of 60° dislocations – typically of a few 10^5 cm^{-1}. Whereas the dislocations density in plastically deformed samples usually does not exceed few 10^4 cm^{-1}.

For the investigations by means of DLTS method, samples with DN have special advantages over the samples with randomly distributed dislocations introduced by plastic deformation method: (i) DN is lying strictly parallel to the sample surface at the pre-defined depth enabling an effective modulation of electric field strength at the position of DN by application of the corresponding external bias voltage, (ii) the density and types of dislocation could be controlled by the twist and tilt misorientation angles and (iii) considerably higher density of dislocations inside the space charge region of a Schottky diode. Therefore, such DNs represent the perfect model objects well suitable for extensive experimental investigations of electrical properties of dislocations in silicon.

1.5 Present contributions

The novel scientific results presented in this work can be specified as follows:

- the exact numerical calculations of the influence of dislocation deformation potential on the carrier thermoemission from the core states of screw and 60° dislocation towards the valence and conduction bands of Si were performed for the first time. A linear dependence of activation energy for the carrier thermoemission on the square root of the electric field –

similar to the Poole-Frenkel effect for Coulomb-like potential but with higher coefficient values – was established.

- the effect of the barrier lowering due to the own electric charge of dislocation line was described theoretically also for the first time. Within the framework of developed model, the broadened DLTS peak with the 'band-like' behavior was explained as continues lowering of thermoemission barrier with the increase of the number of captured carriers.

- the main statements following from the theoretical calculations were verified by detailed experimental investigations of n- and p-type bonded samples with regular DN. Furthermore, the defect states introduced by DN in Si band gap were studied and their main parameters such as density, activation energies and the charge states were derived.

1.6 Appraisal of the work

The results included in this work were presented and discussed at six international scientific conferences: Gettering and Defect Engineering in Semiconductor Technology XIII (GADEST-2009), Berlin, Germany; Beam Injection Assessment of Microstructures in Semiconductors (BIAMS-2010), Halle (Saale), Germany; Extended Defects in Semiconductors (EDS-2010), UK; Extended Defects in Semiconductors (EDS-2012), Thessaloniki, Greece; Gettering and Defect Engineering in Semiconductor Technology XV (GADEST-2013), Oxford, UK; International Conference of Defects in Semiconductors (ICDS-2013), Bologna, Italy

2. THEORY OF THE POOLE-FRENKEL EFFECT DUE TO ELASTIC STRAIN FIELD OF DISLOCATIONS

2.1 Poole-Frenkel effect due to Coulomb potential

Generally, Poole-Frenkel effect [33, 40] describes the lowering of the potential barrier for carrier thermoemission from a localized electronic state as a result of composition of its attractive, Coulomb-like potential that is inversely proportional to the distance, *r*, and of the potential of a uniform external electrical field, *F* (see Fig. 2.1). For this phenomenon to occur, defect must acquire a net charge upon emission of the carrier, i.e. in p-type Si Poole-Frenkel effect is expected to occur for acceptor traps and in n-type Si – for donor traps [41].

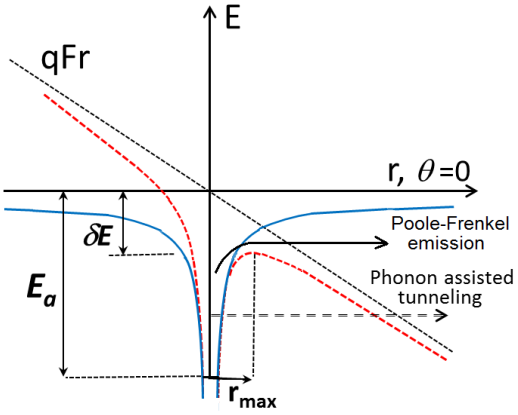

Figure 2.1 One-dimensional representation of the Coulomb attractive potential (solid line) at the defect state E_a and its changes in the presence of a uniform electric field F (dashed line). Modification of the carrier emission process by the Poole-Frenkel effect (barrier lowering by δE) and by phonon-assisted tunnelling are shown.

For the defect potential Ψ/r in electric field holds

$$V(r) = -q(\frac{\Psi}{r} + Fr\cos\theta) \tag{2.1}$$

The resulting potential is three dimensional (3D) and depends on the space angle θ between F and r. It exhibits a maximum at the distance (see Fig. 2.1):

$$r_{\max} = \sqrt{\frac{\Psi}{F\cos\theta}} = \frac{\beta}{2\sqrt{F}} \tag{2.2}$$

The change of the potential barrier height due to the presence of electric field is

$$\delta E_{PF} = -q\beta\sqrt{F} \tag{2.3}$$

and the emission enhancement is then

$$e(F)/e_0 = \exp(\beta\sqrt{F}) \tag{2.4}$$

where

$$\beta = 2\sqrt{\Psi \cos\theta} \tag{2.5}$$

is the Poole-Frenkel coefficient, q is the elemental charge and e_0 is the emission rate at zero electric field. For Coulomb potential $\Psi = q/4\pi\varepsilon$ that gives β-value of 2.22×10^{-4} $V^{-1/2}cm^{1/2}$ in one-dimensional case [33] when $cos(\theta)=1$. The calculation of the field-enhanced emission in the 3D-case needs the integration over spatial angles [40] and gives a slightly lower β-value of about 2×10^{-4} $V^{-1/2}cm^{1/2}$.

The deformation potential of dislocations is also inversely proportional to the distance. It does not exhibit radial symmetry like centered Coulomb potential but there are sectors of angles where it has an attractive character [31, 42]. Thus, a qualitatively similar field effect on the thermal emission of the carriers from electronic states located close to the dislocation core can be expected.

2.2 Poole-Frenkel effect due to attractive deformation potential of dislocations

Calculation procedure of the thermoemission enhancement from the dislocation related states consists of (i) transformation of the expressions for dislocation strains initially written in the dislocation coordinate system into those ones in natural crystal coordinate system, (ii) calculation of the deformation potential angular dependence, (iii) calculation of the Poole-Frenkel coefficient angular dependence, (iv) integration over space angle [43, 44].

The components of the deformation tensor are usually expressed in own dislocation coordinate system where x direction coincides with the dislocation line which is [110] for both screw and 60° dislocations in silicon. Two other directions are arbitrary and will be considered as z along [001] and y – along $[\bar{1}10]$ directions, see Fig. 2.2a. The direction of the external electrical field F in the chosen coordinate system was taken along [001], i.e. along z axis, to correspond with the (001)-orientation of the front surfaces of the investigated samples (see paragraph 3.1).

In this coordinate system the deformation tensor for screw dislocations consist of two non-diagonal components ε_{xz} and ε_{xy}

$$\begin{aligned} \varepsilon_{xz} = \varepsilon_{zx} &= -\frac{Br_y}{4\pi r^2} = -\frac{B}{4\pi r}\sin\theta \\ \varepsilon_{xy} = \varepsilon_{yx} &= \frac{Br_z}{4\pi r^2} = \frac{B}{4\pi r}\cos\theta \end{aligned} \tag{2.6}$$

where B is Burgers vector, r is the distance from the dislocation core and angle θ is count out from z axis [42]. Deformation tensor for edge dislocations consists of three components including also hydrostatic deformation component ε:

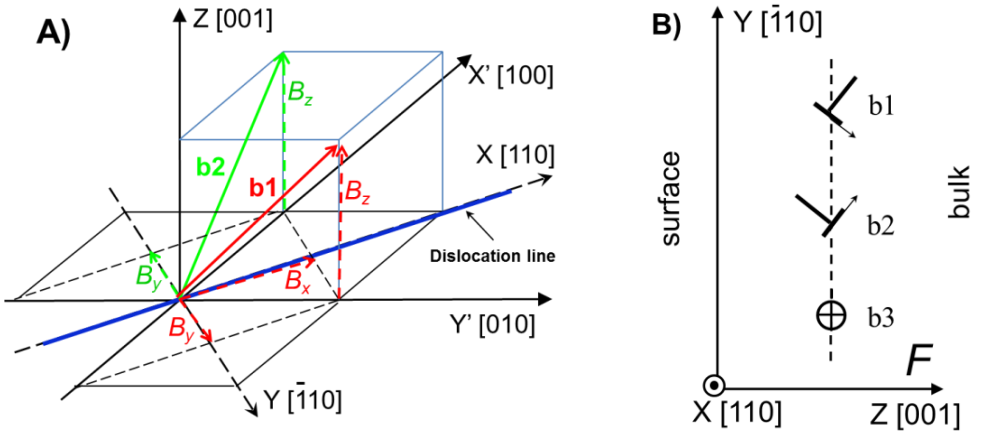

Figure 2.2 (A) Rotation of the dislocation coordinate system around *z* axis by the angle of 45° in order to fit the natural crystal coordinate system. Dislocation line and the Burgers vectors of 60^0 dislocations of *b1* and *b2* orientations (solid arrows) and their projections on the corresponding axes (dashed arrows) are shown. (B) Projections of perfect 60° (*b1*, *b2*) and screw (*b3*) dislocations on (110) plane. Dashed line indicates the projection of DN plane (001). Metal electrode is located on the left side of DN plane, semiconductor bulk – on the right. Electrical field *F* is directed along *z* axis.

$$\varepsilon_{yy} = -\frac{B_y}{4\pi r(1-\nu)}\left(\cos\theta\left\{(1-2\nu)+2\sin^2\theta\right\}\right)+\frac{B_z}{4\pi r(1-\nu)}\left(\sin\theta\left\{(1-2\nu)-2\cos^2\theta\right\}\right)$$

$$\varepsilon_{zz} = -\frac{B_y}{4\pi r(1-\nu)}\left(\cos\theta\left\{(1-2\nu)-2\sin^2\theta\right\}\right)+\frac{B_z}{4\pi r(1-\nu)}\left(\sin\theta\left\{(1-2\nu)+2\cos^2\theta\right\}\right) \qquad (2.7)$$

$$\varepsilon_{zy} = \frac{B_y}{4\pi r(1-\nu)}\left(\sin\theta\left\{1-2\cos^2\theta\right\}\right)-\frac{B_z}{4\pi r(1-\nu)}\left(\cos\theta\left\{1-2\sin^2\theta\right\}\right)$$

$$\varepsilon = Sp(\varepsilon_{ii}) = \frac{(1-2\nu)}{2\pi r(1-\nu)}\left(B_z\sin\theta - B_y\cos\theta\right)$$

where B_x, B_y and B_z are the projections of the Burgers vectors on the corresponding axes (Fig. 2.2a) and ν is Poisson ratio (ν = 0,27 for Si). For pure screw dislocations $B_x = B = 0{,}384$ nm, for 60° dislocation $B_x = B/2$, $B_z = 0{,}707B$, whereas B_y is either $-B/2$ or $+B/2$ corresponding to those two possible orientations of 60^o dislocation with respect to the (001) plane which are marked as *b1* and *b2* in Fig. 2.2b, respectively.

The calculations of the dislocation deformation potential have to be performed in the natural crystal coordinate system that for the cubic lattices is *x'*= [100], *y'*= [010] and *z*= [001]. This can be done by 45° rotation of the dislocation coordinate system around *z* axis [42], see Fig. 2.2a.

Deformation tensor for the dislocation with an arbitrary Burgers vector in natural crystal system could be obtained then following the rule of second-rank tensor and the resulting deformation tensor will be [44]:

$$\begin{pmatrix} \varepsilon_{yy}/2+\varepsilon_{xy} & \varepsilon_{yy}/2 & \frac{\sqrt{2}}{2}(\varepsilon_{zy}+\varepsilon_{zx}) \\ \varepsilon_{yy}/2 & \varepsilon_{yy}/2-\varepsilon_{xy} & \frac{\sqrt{2}}{2}(\varepsilon_{zy}-\varepsilon_{zx}) \\ \frac{\sqrt{2}}{2}(\varepsilon_{zy}+\varepsilon_{zx}) & \frac{\sqrt{2}}{2}(\varepsilon_{zy}-\varepsilon_{zx}) & \varepsilon_{zz} \end{pmatrix} \tag{2.8}$$

where for screw dislocations only the strain components specified in Eq. 2.6 have to be considered and all other components are zero, while for edge dislocations – components which are derived in Eq. 2.7. Corresponding strain tensor for 60° dislocations could be obtained by combination of strain components of screw and edge dislocations taken with the appropriate Burgers vector projections.

Following the deformation potential theory, the valence band in silicon at Γ-point exhibits a shift due to hydrostatic component and splits into two sub-bands due to shear components of deformation tensor [45]. Taking into account the explicit form of deformation tensor Eq. 2.8 the resulting deformation potential of the dislocation at Γ-point can be written as:

$$V_{1,2} = a\varepsilon \pm \left(\begin{array}{l} \frac{b^2}{2}[(2\varepsilon_{xy})^2+(\varepsilon_{zz}-\frac{\varepsilon_{yy}}{2}+\varepsilon_{xy})^2+(\varepsilon_{zz}-\frac{\varepsilon_{yy}}{2}-\varepsilon_{xy})^2]+ \\ +\frac{d^2}{2}((\varepsilon_{zy}+\varepsilon_{zx})^2+(\varepsilon_{zy}-\varepsilon_{zx})^2+\frac{\varepsilon_{yy}^2}{2}) \end{array} \right)^{1/2} = \frac{\Psi_v}{r} \tag{2.9}$$

where sub-indexes 1, 2 correspond to the sign + and –, respectively, and the numerical values of deformation potential constants for the valence band in Si are: a= –5,1 eV, b= –2,2 eV and d= –5,1 eV [5]. For screw dislocations Eq. 2.9 includes only the shear components since $Sp(\varepsilon_{ii})$=0, whereas for 60° dislocations – both shear and non-uniaxial components.

The expressions for the deformation potential of 6-fold X-minima of the conduction band in silicon have the following explicit forms [5, 45]

$$\begin{aligned} V_{(100)} &= \Xi_u(\varepsilon_{yy}/2+\varepsilon_{xy})+\Xi_d\varepsilon = \Psi_{(100)}/r \\ V_{(010)} &= \Xi_u(\varepsilon_{yy}/2-\varepsilon_{xy})+\Xi_d\varepsilon = \Psi_{(010)}/r \\ V_{(001)} &= \Xi_u\varepsilon_{zz}+\Xi_d\varepsilon = \Psi_{(001)}/r \end{aligned} \tag{2.10}$$

with the deformation constants Ξ_d = –6 eV and Ξ_u = 7,8 eV. Potentials expressed by Eq. 2.9 and Eq. 2.10 give per se the desired Ψ-factor introduced in Eq. 2.1 since the $1/r$ term can be taken out of the brackets. Thus, the angular dependence of Poole-Frenkel coefficient $\beta(\theta)$ can be calculated by Eq. 2.5.

Angular dependences of the deformation potential Ψ_v around the screw and 60° dislocations show a significant splitting of the valence band caused by the shear deformations and the formation of the attractive potential by lower sub-band in some specific directions that would cause Poole-Frenkel effect, see Fig. 2.3a. The shapes of the corresponding potentials for two possible orientations of 60° dislocation are similar to each other but shifted by the angle of about 70°.

Figure 2.3b shows $\beta(\theta)$ dependence calculated for the valence band at screw, at both types of 60° dislocations as well as for 3D Coulomb potential. As one can see in Fig. 2.3b, the enhanced emission occurs in the space angles sector (–90°;90°) for screw and 60° *b2* dislocations – similar to 3D Coulomb potential, whereas only in the limited sector (–14°;90°) for 60° dislocations of *b1* orientation.

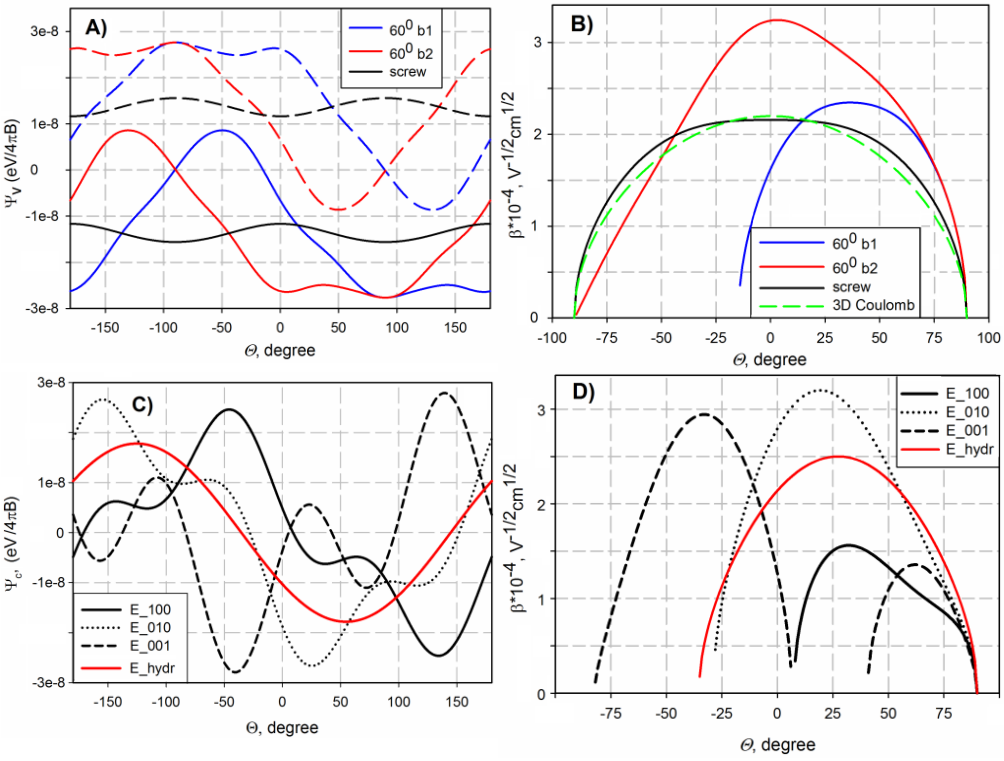

Figure 2.3 (A) Angular dependences of deformation potential (Ψ-factor) and (B) of the Poole-Frenkel coefficients calculated for screw and for 60° dislocations with the *b1* and *b2* orientations at Γ-point (valence band). Solid lines correspond to the sign "plus" in the Eq. 2.10, dashed lines – to the sign "minus". (C) and (D) – corresponding dependences calculated for 60° dislocation of *b2* orientation at each sub-band of X-conduction band together with the curve corresponding to the hydrostatic component only. Angle θ is counted from [001] direction that coincides with the direction of the electric field.

The angular dependence of deformation potential around 60° dislocation calculated for conduction band according to Eq. 2.10 also exhibits a strong impact of shear strain components, see the results of the calculations for 60° *b2* dislocation in Fig. 2.3c. Being considered for each sub-band separately, the sectors of enhanced emission where the deformation potential has an attractive character are rather narrow – Fig. 2.3d. But the joint action of all X-band minima leads to the considerable increase of the favorable angular interval making it wider than in case of hydrostatic component only.

To calculate the enhancement of the emission rate by external electric field the integration of corresponding $\beta(\theta)$ dependences over space angle θ have to be performed:

$$\frac{e(F)}{e_0} = \frac{1}{2\pi}\sum_i \int_{\phi 1i}^{\phi 2i} \exp\left\{\frac{\delta E_i(\theta)}{kT}\right\} d\theta + 1 - \frac{\phi_{2i} - \phi_{1i}}{2\pi} \qquad (2.11)$$

where *i*- counts the X-band minima (*i*=1 for valence band), angles ϕ_{1i}, ϕ_{2i} define the sector where an enhanced emission takes place (Fig. 2.3b and 2.3d). The last two terms make the expression equal to unity in the absence of the electric field. The integration of Eq. 2.11 succeeds only numerically [43, 44].

Differentiation of the numerically calculated $e(F)/e_0$ curves by the square root of electric field gives the dependences of the Poole-Frenkel coefficients β on $\sqrt{F}$, which are presented in Fig. 2.4a for the valence band and in Fig. 2.4b for conduction band. At sufficiently high electric field values all obtained curves can be well fitted with Poole-Frenkel law Eq. 2.4 (in Fig. 2.4 that corresponds to the horizontal part of the curves). Calculated values of β-coefficients are summarized in Table 2.1.

The largest value of $\beta \approx 3{,}1\times10^{-4}$ (in $cm^{1/2}\ V^{-1/2}$ units) was obtained for *b2* orientation of 60° dislocation for the valence band (p-type) as well as for screw and 60° *b2* dislocations for conduction band (n-type). Note, that $\beta \approx 3\times10^{-4}$ just corresponds to an effective electron charge q^*=2,7 of centered attractive potential – exactly as the value used by Hedemann et al [23] in the simulations of DLTS peak shape due to $NiSi_2$ nanoprecipitates.

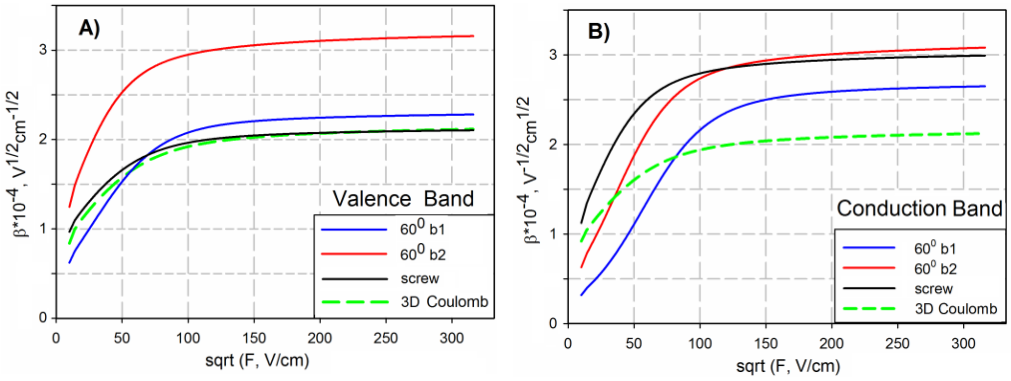

Figure 2.4 Poole-Frenkel coefficients calculated for the valence band (A) and for the conduction band (B) at screw and 60° dislocations of *b1* and *b2* orientations. Poole-Frenkel coefficient calculated for 3D Coulomb potential is also shown for comparison.

Table 2.1. Numerically calculated values of dislocation related Poole-Frenkel coefficients β (in 10^{-4} $cm^{1/2}$ $V^{1/2}$ units) for emission towards the valence and conduction bands for sufficiently high electric fields so that $\sqrt{F} > 100$.

	valence band	conduction band
screw	2,1	3,0
60° *b1*	2,3	2,6
60° *b2*	3,1	3,1

Somewhat smaller values were derived for 60° dislocations of *b1* orientation $\beta \approx 2{,}3\times10^{-4}$ (valence band) and $\beta \approx 2{,}6\times10^{-4}$ (conduction band) due to the less optimal orientation of the attractive part of deformation potential relative to the electric field direction. The smallest value $\beta \approx 2\times10^{-4}$ was obtained for screw dislocations in p-type Si, which is rather similar to that for 3D Coulomb potential, see Fig. 2.4a.

Thus, except the β-value for screw dislocations in p-type Si, all other values of Poole-Frenkel coefficient due to elastic strain fields of dislocations exceed well the value for Coulomb-like potential of singly charged point defect. It should be also underlined that for obtained β-values the Poole-Frenkel radius r_{max} (Eq. 2.2) would be of the order of few till 10-15 nm that is large enough to use the approximation of the effective mass and dielectric constant but small enough not to consider the effect of screening with the charged dopants as their inter-distances are larger than the r_{max}-values by at least one order of magnitude.

2.3 Strain field localization in dense DN

In the bonded samples with dense dislocation network the interaction of elastic strain fields of the neighboring dislocations must be taken into account, what generally results in the localization of the dislocation strain field [42, 46]. Figures 2.5a and 2.5b represent the sketches of two dislocation structures consisting of a parallel array and of a square mesh of dislocations with the interdislocation distances *D*.

For the screw dislocations array that expands in *y* direction (Fig. 2.5a) the elastic strains are [42]:

$$\varepsilon_{xz} = \frac{B}{4D}\frac{\sin 2\pi Y}{\cosh 2\pi Z - \cos 2\pi Y}$$

$$\varepsilon_{xy} = \frac{B}{4D}\frac{\sinh 2\pi Z}{\cosh 2\pi Z - \cos 2\pi Y} \qquad (2.12)$$

where $Z=z/D$, $Y=y/D$ are the reduced variables. Asymptotic behavior of Eq. 2.12 at $Y=0$ (i.e. at the exact dislocation position in a row) when $Z\rightarrow 0$ corresponds to the strain of an isolated dislocation

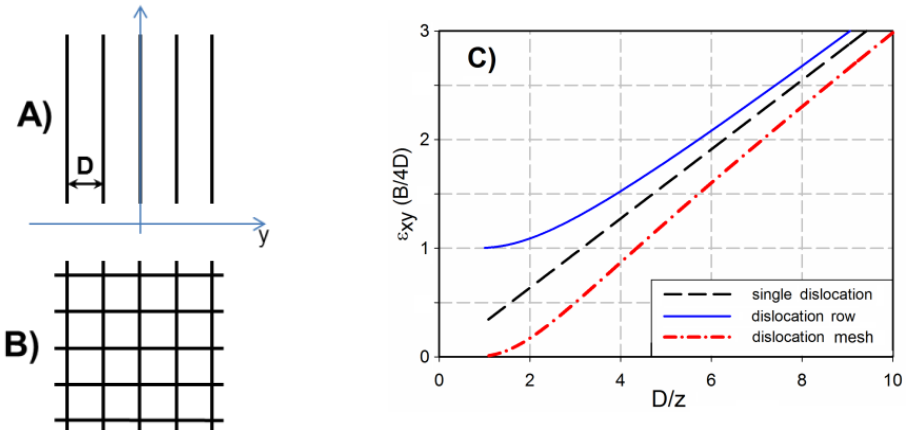

Figure 2.5 Row of parallel dislocations (A) and square mesh of dislocations (B) with the interdislocation distance *D*. *Z*-axis is perpendicular to the pictures plane. (C) Deformations of an isolated dislocation, the dislocations row and the square mesh as a function of inverse distance *D/z* from DN plane. For the square mesh *z*-coordinate is going through the center of dislocation segments between the nodes.

$$\varepsilon_{xy} \to \frac{B}{4\pi z}, \tag{2.13}$$

whereas for $Z\to\infty$ ε_{xz} disappeared, but ε_{xy} reaches a stationary value of B/4D, indicating thereby the presence of long-rang stress field for the row of dislocations. The deformation components for the screw dislocation network consisting of two rows of dislocations that are going along *x* and *y* (Fig. 2.5b) will be equal to [42, 46]

$$\begin{aligned}
\varepsilon_{xz} &= \frac{B}{4D}\frac{\sin 2\pi Y}{\cosh 2\pi Z - \cos 2\pi Y} \\
\varepsilon_{yz} &= \frac{B}{4D}\frac{\sin 2\pi X}{\cosh 2\pi Z - \cos 2\pi X} \\
\varepsilon_{xy} &= \frac{B}{4D}\sinh 2\pi Z\left(\frac{1}{\cosh 2\pi Z - \cos 2\pi Y} - \frac{1}{\cosh 2\pi Z - \cos 2\pi X}\right)
\end{aligned} \tag{2.14}$$

The presence of the second dislocation row makes $\varepsilon_{xy}=0$ far from the plane of the network ($Z\to\infty$) providing the pure rotation of the matrix in the vicinity of the square network without long-range field. Besides, according to Eq. 2.14, ε_{xy} along the network diagonals (X=Y) would be zero including the points of dislocations intersection, but remains practically constant along the most part of the segments between the knots, see Fig. 2.6.

Figure 2.5c compares the deformations ε_{xy} of an isolated dislocation, of the row and of the square mesh of dislocations as a function of inverse distance from the DN plane. The main effect of the dislocation interaction is a significant shortening of the deformation

field radius. At the distances from the dislocation interface of about one period of the dislocations in a row or network strain ε_{xy} reaches a spatially independent value that is *B/4D* for dislocation row and nearly zero for dislocation network.

One may also note in Fig. 2.5c, that the significant difference of the strains from *1/r* law starts at the distances larger than about *D/4* and *D/2* for dislocation row and dislocation network, respectively. This imposes a restriction on the realization of the Poole-Frenkel effect due to elastic strain field of dislocations. Obviously, dislocation-related Poole-Frenkel effect can be observed under the application of the electric field above the value F_{min} so that the correspondent Poole-Frenkel radius r^* (Eq. 2.2) would be of about *D/4* or *D/2*:

$$F_{\min} > \left(\frac{(2 \div 4)\beta}{2D} \right)^2 \tag{2.15}$$

where the numbers 2 or 4 relate to the dislocations mesh or to the row, respectively.

In the same way, the estimations can be made for D_{min} when the theory for isolated dislocation is valid:

$$D_{\min} > \frac{(2 \div 4)\beta}{2\sqrt{F_{\min}}} = (2 \div 4) \cdot r^* \tag{2.16}$$

Similar estimation can be done for the row of edge dislocations as well [42]. Thus, following the theoretical calculations presented in this and in the previous paragraphs it can be concluded that β-coefficients of dislocation-related Poole-Frenkel effect depend strongly on type, orientation and on the density of dislocations in the DN.

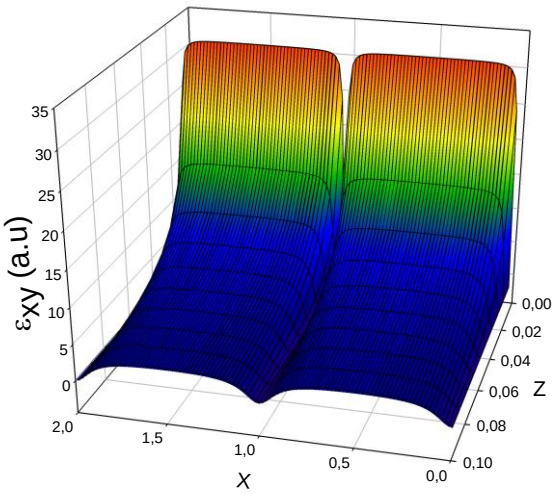

Figure 2.6 Decreasing of the strain field ε_{xy} while moving away from the DN plane which corresponds to *Z=0*. Integer numbers of *X* correspond to the positions of dislocation lines, according to the sketch Fig. 2.5.

2.4 Influence of dislocation own charge

General condition for the realization of the dislocation-related Poole-Frenkel effect implies that the traps are located within the attractive part of dislocations deformation potential. In this case the own electric field of the dislocation line charge cannot be neglected anymore. The non-screened repulsive Coulomb potential of the dislocation line can be written as [47]

$$\begin{aligned} \phi_l &= -B\ln\frac{r}{r_{core}} \\ B &= \frac{qN_l}{2\pi\varepsilon} = \frac{qN_sD}{2\pi\varepsilon} \end{aligned} \tag{2.17}$$

where r is the distance from the dislocation line, r_{core} is the radius of dislocation core, N_l is the number of electrons captured per unit length of dislocation, N_s is the averaged density of the electrons per unit area, D is the mean interdislocation distance at the bonded interface. The resulting total potential will be then a sum of three components – dislocation deformation potential (Fig. 2.7a curve 2), Coulomb potential of charged dislocation line (Fig. 2.7a curve 1) and the potential of external electric field:

$$V(r) = -q\left(\frac{\Psi(\theta)}{r} + B\ln\frac{r}{r_{core}} + Fr\cos\theta\right) \tag{2.18}$$

When the external electric field is absent F=0, the sum of dislocation deformation potential and the potential of charged dislocation line (Fig. 2.9a curve 4) would have a maximum at the position of

$$r_d = \frac{\Psi(\theta)}{B} \tag{2.19}$$

and the corresponding value of the potential lowering (vertical dashed arrow in Fig. 2.7) is then:

$$\delta E_d = -qB\left(\ln\frac{r_d}{r_{core}} + 1\right) = -q\frac{qN_l}{2\pi\varepsilon}\left(\ln\frac{2\pi\varepsilon\,\Psi(\theta)}{qN_l\,r_{core}} + 1\right) \tag{2.20}$$

Simple analysis of Eq. 2.20 shows that the reduction of the potential barrier for electron emission should increase with dislocation line charge N_l, since the linear dependence on N_l in the prefactor grows stronger than the decreasing term under the logarithm (see Fig. 2.8b and also Fig. 3.10 in paragraph 3.7). This leads to an important conclusion about the emission enhancement with the increase of the dislocation line charge, the property that was previously ascribed to the ‘band-like’ character of the electronic spectrum of some extended defects like $NiSi_2$ nanoprecipitates [22].

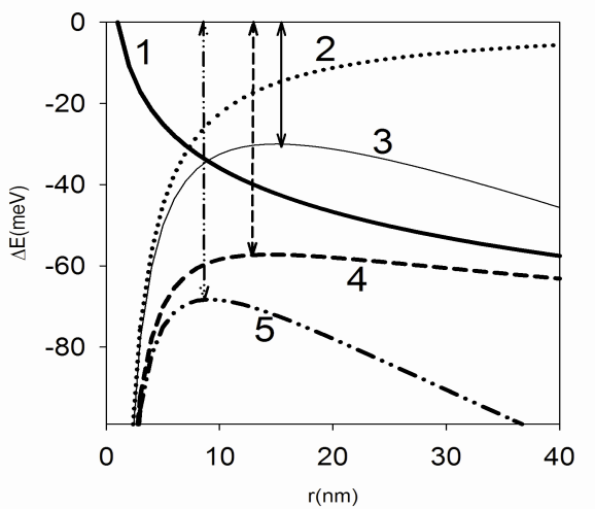

Figure 2.7 Variations of the potentials with distance r from DN plane: (1) repulsive Coulomb potential of the charged line with a line density of 6×10^5 cm^{-1}, (2) dislocation deformation potential, (3) sum 2 + external electric field of 10^4 V/cm, (4) sum 1 + 2, (5) sum 1 + 2 + external electric field of 10^4 V/cm. Space angle θ =0.

In the presence of external electric field (Fig. 2.7a curve 5) the radius corresponding to the potential maximum becomes equal to

$$r_F = \left(\frac{B}{2\Psi(\theta)} + \sqrt{\left(\frac{B}{2\Psi(\theta)} \right)^2 \pm \frac{F\cos(\theta)}{\Psi(\theta)}} \right)^{-1} \tag{2.21}$$

and the reduction of the potential barrier for electron thermoemission (Fig.2.7a, dashed-double dot arrow) is given by:

$$\delta E_\Sigma = -q\left(\pm F r_F \cos(\theta) + B\ln\frac{r_F}{r_{core}} + \frac{\Psi(\theta)}{r_F} \right) \tag{2.22}$$

where sign + or – in Eq. 2.21 and 2.22 corresponds to the usual direction of the electric field towards the semiconductor bulk or to the inverted direction towards the surface, respectively. Equation 2.22 defines explicitly the reduction of the potential energy for carrier thermoemission as the function of dislocation line charge and the applied electric field and would be further considered in paragraph 3.7 to make the comparisons with the experimental data.

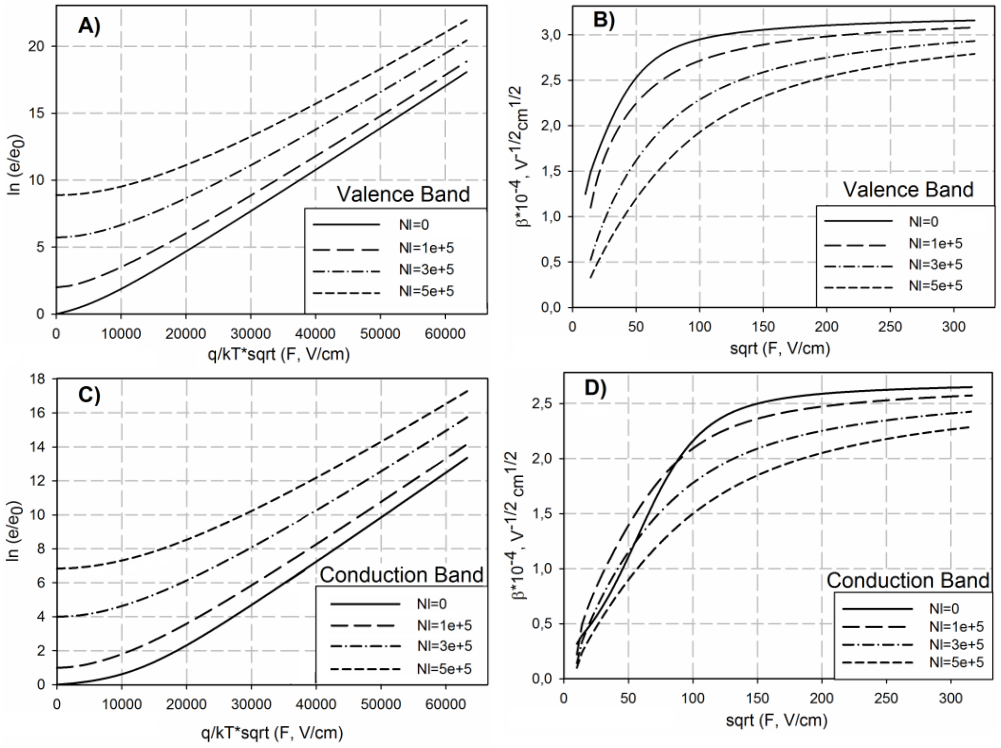

Figure 2.8 Results of numerical calculation of field enhanced carrier emission towards the valence band (A) and towards the conduction band (C) as calculated for 60° *b2* and 60° *b1* dislocations, respectively, with the diverse dislocation line charge N_l shown in the legend. kT=5 meV. (B) and (D) Corresponding variations of the Poole-Frenkel coefficients β.

The impact of the own dislocation line charge on the field dependence of the emission rate is demonstrated in Fig. 2.8a and 2.8c which show the results of exact numerical calculation for 60° dislocations of *b2* orientation for emission towards the valence band and of *b1* orientation for emission towards the conduction band. It follows from these plots that with increase of the dislocation line charge the emission rate increases at zero as well as at all the field values, but the slope of the corresponding dependences – i.e. β-coefficients – decreases, see Fig. 2.8b and 2.8d. Besides, the range of electric field where the Poole-Frenkel law becomes valid is shifted towards the higher field values. As a result, one may expect the variation of the experimentally derived values of the Poole-Frenkel coefficient with a number of charge carriers captured on the dislocation states.

2.5 Summary of the theoretical part

The results of the theoretical calculations presented in this Chapter have demonstrated that:

- the interaction of dislocation deformation potential with the external electric field leads to the barrier lowering for carrier thermoemission in the way similar to the Poole-Frenkel effect for charged Coulomb centers.
- the resulting values of the Poole-Frenkel coefficients for dislocation deformation potential appeared to be significantly higher than the value for Coulomb-like potential of singly charged point defect and depend strongly on the dislocations type, orientation of the Burgers vector relative to the electric field and on the distances between the neighboring dislocations
- the own electric field of charged dislocation line gives rise to the additional barrier lowering with the increase of the number of captured carriers but simultaneously to the decrease of the corresponding β-values.

3. EXPERIMENTAL RESULTS

3.1 Samples and experimental details

The samples for the investigations were fabricated by hydrophilic bonding of (001)-oriented silicon wafers of n- and p-type conductivity doped to 10^{14} cm^{-3} with phosphorus and 10^{15} cm^{-3} with boron, respectively. Hydrophilic bonding process implies that the wafers were covered initially by the native oxide layer which was completely dissolved during the post-bonding annealing at 1200°C for 2 hours in high purity conditions leading to the restoration of direct Si-Si covalent bonds [48].

Wafers were bonded with different twist angles α_{TW} between 1° and 3°. A typical tilt angle of α_{TI} ~ 0.5°-0.7° arose as a result of non-uniformity of wafers polishing. Interdislocation distances were determined by means of transmission electron microscopy (TEM) measurements and are encoded in the samples notations, see Table 3.1 and TEM images in Fig. 3.1. Unlike to the straight screw dislocations which form a well-defined square network with the definite interdislocation distances, 60° dislocations look wavy with the interdislocation distances varying typically from 20 to 60 nm. DN interface is lying parallel to the front surface at the depth of ~160 nm, being thus inside the space-charge region (SCR) of the Schottky diodes even at zero bias voltage. This means that the free carrier density at the permitted bands is negligible at DN depth and the local DN-related electronic states in the band gap are empty at zero and at all reverse bias voltages.

Schottky contacts were produced by evaporation of 100 nm-thick gold/titanium dots with 1.5 mm diameter on the front surface of n-type/p-type samples, respectively. Ohmic contacts were prepared by rubbing of AlGa on the rear side of the samples. Control samples were prepared by Schottky contacts evaporation on the mirror-polished rear surface of the bonded wafers.

Experimental investigations were performed by various methods of junction spectroscopy – deep level transient spectroscopy (DLTS), isothermal DLTS (ITS) and by capacitance-voltage and current-voltage (CV/IV) characterization. DLTS is a capacitance transient thermal scanning method applied for detection of electrically active defects in semiconductors [15]. The technique displays the spectrum of the traps in a crystal where the height of the peak is proportional to the trap concentration and the temperature position is uniquely determined by the thermal emission properties of the trap. Note, as the DLTS spectra of extended defects (dislocations, precipitates, etc.) exhibit broadened DLTS peaks, the standard single level model developed for point-like defects does not allow reliable determination of the trap density and activation enthalpy from Arrhenius-plot analysis [1, 22, 31].

Table 3.1. Samples notations and corresponding mean interdislocation distances. *DN of p-/60 sample doesn't contain screw dislocations and consists of uni-directional 60° dislocations (I set D ~ 60 nm) disturbed by the curved 60° dislocations (II set D ~ 100-200 nm), issuing in the triple knots formation in the intersection points, see TEM image in Fig. 8 of included article PII.

	n-16/42	n-6/37	p-8/30	p-/60*
D_{screw}, nm	16	6	8	-
$D_{60°}$, nm	42	37	30	60

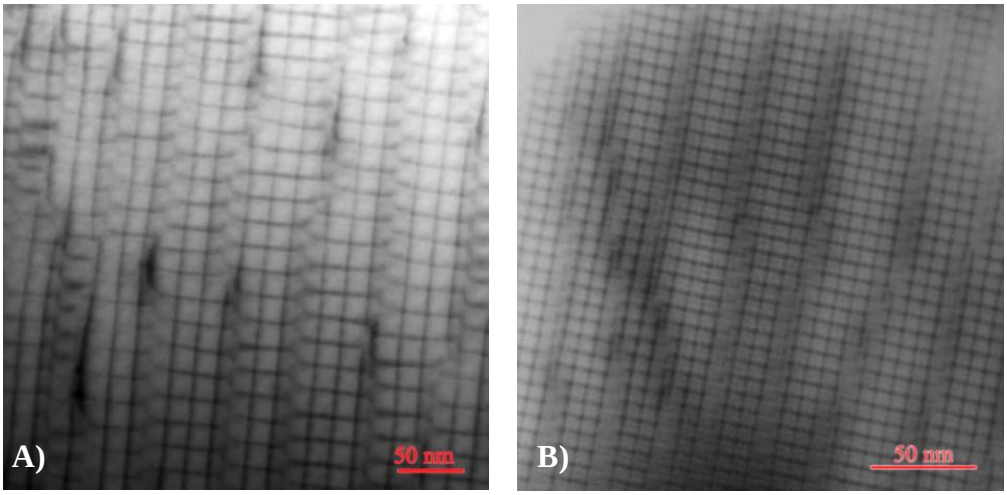

Figure 3.1 Multibeam TEM plan-view images of DN in n-16/42 (A) and p-8/30 (B) sample showing the regular square network of screw dislocations which is intercepted by the array of 60° dislocations going vertical on these images. Co-existence of screw and 60^0 dislocations at the bonded interface causes a zigzag reaction [49] giving rise to the displacements of the screw dislocations by about half network spacing 0,5* D_{screw}.

ITS method is similar to DLTS one in using the same correlation procedure and the sequence of voltage pulses but the measurements are performed at the constant temperature under the gradually increasing rate window period t_w [44]. Position of the ITS peak gives straightforwardly the emission time constant τ at the measurement temperature.

DLTS, ITS and CV/IV measurements were performed by means of transient Fourier spectroscopy system DL-8000 (Accent) equipped with the closed cycle cryostat (temperature range 20-320K) with red light emitting diode (LED) mounted inside.

3.2 Band bending diagram from CV and IV data

In order to define the energy-band structure of the Schottky diode with the DN located inside its space charge region, a set of capacitance-voltage (CV) and current-voltage (IV) measurements was performed at various temperatures between 300K and 40K (the later corresponds to the appearance of dominating low temperature DLTS peak, see Fig. 3.4a) in darkness and under illumination by red LED.

At room temperature IV curves of all bonded samples demonstrate the appearance of forward current through the diode at similar small forward voltage – the same as the reference sample without DN. Whereas at low temperatures of 80K and 40K a detectable diode current appears at significantly larger forward voltages, i.e. an additional voltage drop appears on IV characteristics of all bonded samples with a certain dependence on the measurement temperature (being higher at 40K than at 80K) and DN structure (the dense the DN – the higher the voltage drop), but not on IV curves of the reference sample where

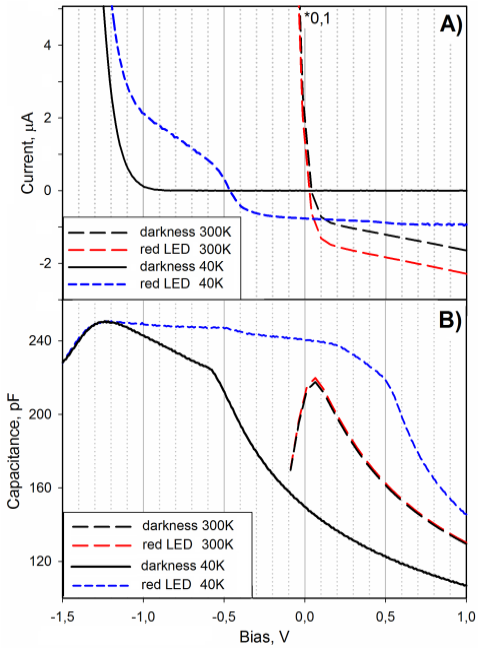

Figure 3.2 IV curves (A) and CV-curves (B) measured on p-8/30 sample at 300 K and 40 K in darkness and under red LED illumination. Assignments of the curves are shown in the legends. IV curves measured at 300K were multiplied by factor 0,1 to fit the scales.

the diode opening voltage remains small and independent on temperature [44]. Examples of IV curves measured at p-8/30 sample in darkness at 300K and 40K are shown in Fig. 3.2a.

Obviously, the voltage drop at low temperatures is caused by the non-compensated positive/negative charge collected by DN-related traps in p-/n-type bonded samples and which is absent when the traps are neutral in empty state at 300K – as it follows from identical IV curves measured at this temperature. By cooling DN traps become filled with charge carriers giving rise to the formation of the potential barrier along DN so that the current flow in the range of forward biases of 0V... –1V is defined by this DN-barrier. The potential at DN depends on the number of charge carriers captured by DN-states, whereas the later – on the dislocations density in the network. At measurement temperature of 80K DN-barrier arises due to the charge collected by rather deep traps only, while at 40K by deep and relatively shallow traps. Consequently, DN traps located in the lower part of band gap which are neutral when empty and positively charged when filled with holes should be identified with donor-like traps, whereas the traps in the upper part which become negatively charged when filled with electrons – with the acceptor-like traps.

IV and CV measurements at low temperature under red LED illumination have confirmed explicitly the presence of the potential barrier along DN at low temperatures [50]. While no considerable effect of illumination was detected at 300 K except the higher reverse current due to the flux of minority photo-generated carriers, the inversion of photocurrent sign was detected at low temperatures by exceeding some threshold voltage,

see Fig. 3.2a where this voltage is U_{th}= –0,45 V for p-8/30 sample. Below the threshold voltage the current direction corresponds to the minority carrier flux from semiconductor bulk towards the SCR of the diode, i.e. in the direction expected for usual diode. The opposite direction of photocurrent indicates the inversion of electric field direction – what can occur only when the potential barrier φ_{DN} at the DN becomes higher than the barrier at the metal-semiconductor interface φ_S, i.e. the field inversion occurs in the layer between the bonded interface and the sample front surface.

CV measurements have revealed a considerable increase of sample capacitance under illumination at 40K. Other particular features of CV-curves at 40K are the regions of nearly constant capacitance step at –0,55V... –1,25V on CV curve measured in darkness and at 0,5V... –1,25V on CV curve measured under illumination, see Fig. 3.2b. More detailed interpretation of these observations can be done with the help of band diagram presented in Fig. 3.3.

Without illumination at 0 V (Fig. 3.3a) the potential at metal-semiconductor interface is higher than that at DN which is defined at this voltage by the charge of deep levels remaining filled with majority carriers at 40K even at reverse biases. With the increase of forward bias barrier φ_S decreases, but φ_{DN} is stabilized at first by the charge of deep levels and then, at U_f= –0,55 V, the filling of the shallow states begins (Fig. 3.3b), giving rise to the appearance of the step on CV curve measured in darkness as a result of the Fermi-level pinning. The fact that the inversion of the photocurrent direction occurs at slightly lower forward bias voltage than the CV step implies that the charge of the deep traps on DN defines the barrier φ_{DN} at the moment of current inversion.

Illumination leads to the lowering of the DN barrier height due to the flux of minority carriers which are attracted towards the SCR by the electric field and some of them will be captured by the DN states and recombine with the trapped majority holes. This will cause the increase of sample capacitance, just as it follows from the equation for Schottky diode with DN inside [44]

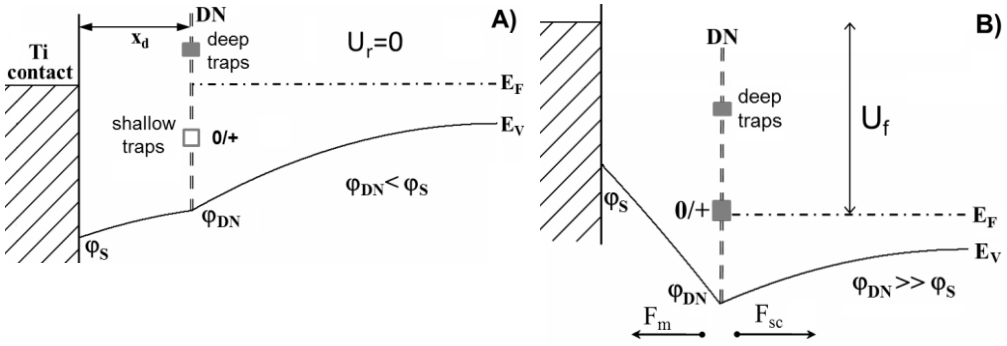

Figure 3.3 Sketches of band diagrams of the p-type Schottky diode with the DN lying inside the SCR at the distance of x_d from the surface in darkness at *0V* (A) and at forward bias voltage (B) when the DN-barrier φ_{DN} is higher than Schottky barrier φ_S and controls the current through the diode. Fermi level is pinned by the shallow traps and its position at the bonding interface defines the filling grade of the states. The inversion of the electrical field direction occurs in the layer between the sample front surface and DN when $\varphi_{DN} > \varphi_S$.

$$C = \frac{\varepsilon S}{w} = S\sqrt{\frac{q\varepsilon N_A}{2U + 2Q_s x_d/\varepsilon}} \tag{3.1}$$

and could be seen on CV curve measured under illumination in Fig. 3.2b. Here U is the applied bias voltage, w is the SCR width, ε is the dielectric constant, N_D is the doping level, Q_s is the charge collected by DN traps located at the depth x_d and S is the diode area. When the reverse bias voltage approaches zero, holes from the carrier tail and those generated inside the SCR would refill the interface states restoring the barrier height. This induces a strong pinning of Fermi level at the defect states, which is observed as a long capacitance step on the "illuminated" CV curve in Fig. 3.2b.

As the concentration of light-induced minority electrons is limited in caser of low excitation condition, they would unable to compensate the DN-charge completely. Thus, the further increase of forward bias would lead to the increase of φ_{DN} and decrease of φ_S so that the most of majority electrons generated inside the sample top layer would be accelerated by the inverse electric field towards the metal contact giving rise to the majority carrier current appearance. Finally, at higher forward biases, the barrier along the dislocation network will disappear and the forward current branches on the IV curves measured in darkness and under illumination will join each other.

3.3 DLTS spectra of the DN-related electronic states

DLTS measurements have revealed the similar features for all n- and p-type bonded samples studied here, namely the broadened low temperature peak STn/STp dominating the spectra and a set of unresolved peaks appearing at 100-250K and consisting of at least four peaks in p-type samples and of 1-2 peaks of noticeably smaller magnitudes in n-type samples. Examples of the DLTS spectra measured on n-16/42 and p-8/30 samples are shown in Fig. 3.4a where the vertical scale represents the surface density of captured carriers (electrons or holes) N_s that was calculated from DLTS signal amplitude, dC, according to [44]:

$$N_s = -\frac{S^2\varepsilon^2}{x_d} N_D \frac{dC}{C^3} \tag{3.2}$$

Traps density profiles were calculated as derivative of the dependences of DLTS signal on the refilling pulse voltage measured at selected temperatures corresponding to the peak maximum with fixed reverse bias voltages U_r and under the gradually increased filling pulses U_p. Resulting narrow profile peaks reflect the "plane-like" (2D) distribution of the traps, see examples for STp and DTp-0,48 traps in p-8/30 sample presented in Fig. 3.4b. Note, that the profile peak for STp traps appears at approximately the same forward voltages as the capacitance step on CV curve of p-8/30 sample measured at 40K, confirming that this step is really caused by the Fermi-level pinning during the capturing process onto the shallow STp traps. The approximation of the depth position of the trap plane, calculated conventionally from the depletion region width, trap level energies estimated from Arrhenius plots and the doping concentration gives the value of ~ 200 nm that is very close to the thickness of the top layer, i.e. ~160 nm [44]. No DLTS peaks were

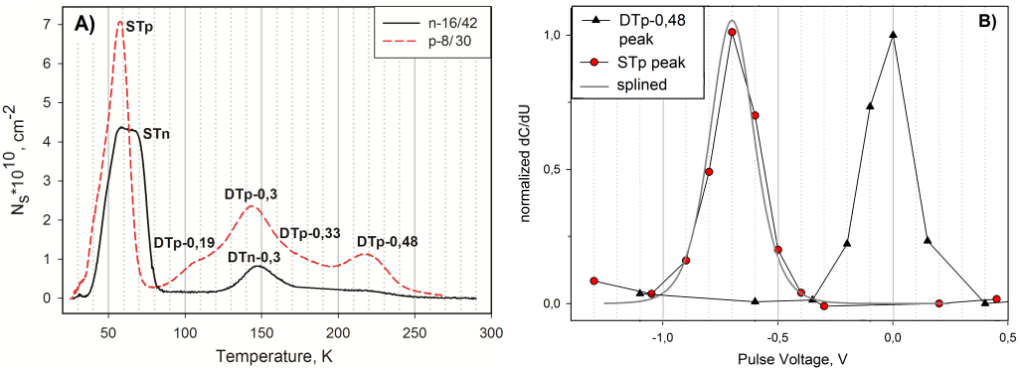

Figure 3.4 (A) DLTS spectra of n-16/42 and p-8/30 samples. Activation enthalpies for carrier thermoemission are shown as a part of the corresponding peak notation. DLTS-scan parameters: filling pulse duration t_p= 100μs, reverse bias U_r=1V, forward filling pulse voltage U_p= –1V, rate window t_w=20ms. (B) Traps density profiles for STp and DTp-0,48 traps normalized to their maximum value. The voltage difference between the profile peaks (~0.7 V) is due the difference of their activation enthalpies[44].

detected on the control samples without DN. Thus, it could be concluded that all detected DLTS peaks are directly related with the defect states introduced by DN.

A good correspondence was found between the Arrhenius graphs for DTp-0,19, DT-0,33 and DTp-0,48 DLTS peaks and those for the peaks H.21, H.33 and H.49, respectively, observed by Kisielowski and Weber in the plastically deformed p-Si samples [18]. These deep traps in the plastically deformed p-Si were attributed to the point defects or point defect clusters at or close to the dislocations, but not to the dislocation core states. However, no clear correlation with known defects was found for DTp-0,3 and DTn-0,3 traps.

Hydrogenation of similar p-type bonded samples in HF acid solution has resulted in a strong reduction of the amplitude of all DTp peaks due to deep DN-related traps but not of the low-temperature STp peak [51]. It is well-known that hydrogen passivation treatments can reduce the concentration of electrically active localized electronic states caused by vacancies or impurity atoms incorporated into the dislocation core or distributed in the defect cloud around the dislocation, however hydrogenation could not affect the one-dimensional 1D energy bands caused by dislocation elastic strain field [2]. Thus, deep DN-traps could be indeed attributed to the point defects or point defect clusters – most probably related with interstitials and oxygen atoms arose during the buried oxide layer dissolution upon annealing, whereas the shallow STp/STn traps – to the deformation induced shallow 1D dislocation states.

Recent minority carrier transient spectroscopy (MCTS) study [52] has confirmed that two shallow bands exist simultaneously in the opposite parts of band gap in both n- and p-type bonded samples. Consequently, shallow STn and STp traps are indeed the traps inherent to dislocations. So, this is the second time after the experiments of Castaldini et al [29] as the shallow dislocations-related levels were detected by DLTS method. Obviously, the high density of dislocations inside the SCR of Schottky diode located parallel to the sample surface minimizing thus the carriers drift along the dislocation lines outside the SCR allowed us to get a strong DLTS signal.

3.4 Impact of external electric field on carrier thermoemission from shallow DN-related states

Figures 3.5a and 3.5b represent the set of DLTS spectra of p-8/30 and n-16/42 samples recorded with the different reverse biases U_r and a constant forward filling pulse voltage. It is clearly visible in Fig. 3.5a, that the temperature position of low-temperature STp peak shifts towards the lower temperatures with the increase of the applied reverse bias, i.e. with the increase of the electric field. In n-16/42 sample a broadened rectangular-shaped DLTS peak with a very flat top appeared at low U_r voltages. With the increase of applied reverse bias the right shoulder of STn peak shifts towards the lower temperatures. Low-temperature shift indicates the enhancement of carrier thermoemission from both shallow STn and STp traps with the increase of the external electric field F. Another particular feature of STn peak is the shift of its left shoulder towards the higher temperatures with the increase of the reverse bias, leading to the DLTS peak narrowing with simultaneous growth of its amplitude.

Broadened shape of low-temperature DLTS peaks in p- and especially in n-type samples affects the precision of their activation enthalpies E_a determination from the Arrhenius plots, so the ITS method was applied to quantify the field enhanced emission from STp/STn traps. The advantage of the ITS method over DLTS is that by measuring the ITS spectra at different reverse bias voltages one may trace the variation of emission rate e with the electric field directly, without the determination of activation enthalpies from the Arrhenius plots. To plot the dependence of emission rate on the electric field one may use the emission rate values e_{max} corresponding to the ITS peaks maxima, or simply to plot the dependence using the e values taken at the similar height on the right-side shoulder of the ITS peaks recorded with the different reverse bias voltages (as shown by the horizontal line in Fig. 3.6a) – what can be useful for analysis of broadened ITS peaks like in n-16/42 sample. Since the response of the DLTS correlator is the function of the product of the emission rate e and the correlator period t_w, the dependence of e on the electrical field as obtained at every certain level of ITS signal (i.e. keeping the product $et_w = const$) will be shifted relatively to the analogous dependence derived for e_{max} points, preserving the slope which gives the β constant [44]. Afterwards, this shift can be corrected to fit the true values of the emission rate.

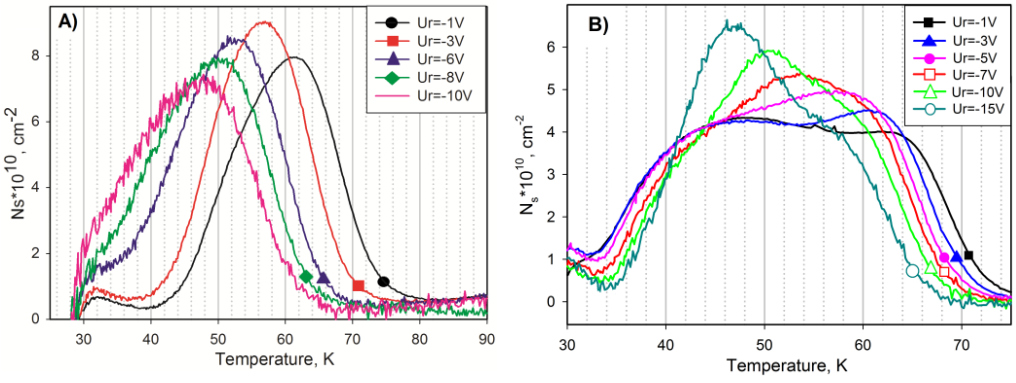

Figure 3.5 Low-temperature peaks STp in p-8/30 (A) and STn in n-16/42 (B) samples measured with different reverse bias voltages U_r shown in the legends. Refilling pulse voltage –1,5V, pulse duration 1 ms, rate window period t_w= 200 ms for n-16/42 and t_w= 20 ms for p-8/30.

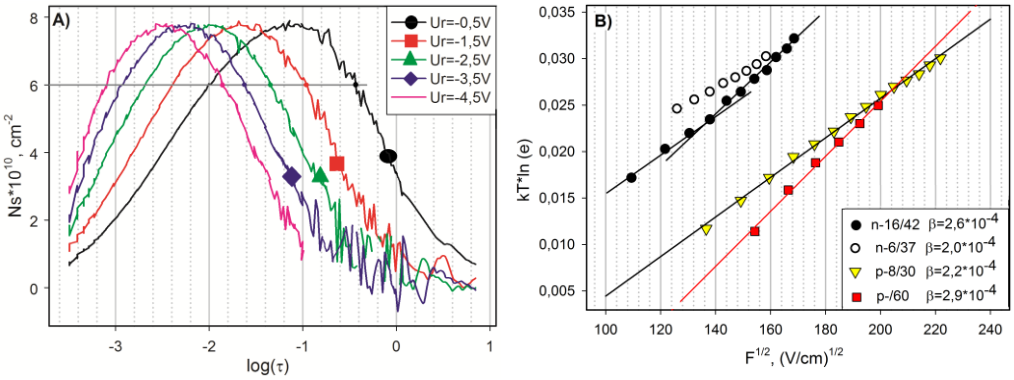

Figure 3.6 (A) Set of ITS spectra of p-8/30 sample showing the variations of ITS peak due to STp shallow traps with increase of the reverse bias voltages U_r. Ordinate axis shows the surface density of captured holes, abscissa axis – common logarithm of the emission time constant. Measurement temperature was 53K, filling pulse duration t_p=*1 ms*, filling pulse voltage U_p= –1,5 V. (B) *kT*-corrected logarithms of emission rate as the functions of square root of electric field *F* for shallow STp/STn traps in n- and p-type bonded samples. The symbols correspond to the experimental data obtained from the cutoff on the same level on the right shoulder of ITS peaks after their re-normalization to represent the true values of emission rates, the lines represent the best linear fits.

Examples of ITS spectra for STp peak in p-8/30 sample measured with different reverse bias voltages are presented in Fig. 3.6a (another examples of DLTS/ITS spectra measured with different U_r can be found in the included article PII Fig. 5-6). The increase of the electric field in the SCR results in a shift of ITS peak position towards the lower values of emission time constant. Similar set of ITS measurements was performed for the n-type samples, too.

The electric field at the position of the DN (x_d ~160nm below the sample surface) for each reverse bias voltage was calculated using the standard equation

$$F = qN_D(w - x_d)/\varepsilon \tag{3.3}$$

where the doping level N_D and SCR-width w were calculated from CV data. Generally, the charge collected by the DN-related states should be included in the calculations of the electric field, too. However, the simplified formula is valid when the traps occupation is low, so that the total charge of the doping impurities inside the space charge region qN_Dw is larger than the charge collected by DN traps, i.e. $qN_Dw > qN_{DN}$. This condition holds when the emission rate values are defined at the same level on the right-side shoulder of the ITS peaks corresponding to the high τ values, so that most of trapped carriers would be already emitted from the shallow traps.

Using the values of the emission rate e derived from ITS measurements and the calculated values of electric field corresponding to the actual bias voltage, the dependences of the logarithm of emission rates on the square root of electric field were plotted for STp/STn traps in p-8/30 and n-16/42, as well as in p-/60 and n-6/37 samples (Table 3.1) – see Fig. 3.6b. One can see that the dependences obtained for the STp peak in p-type bonded samples could be well approximated by the straight lines, thus following

the Poole-Frenkel law given by Eq. 2.4. The slope of the curves defines the Poole-Frenkel coefficients β which are also listed in the legend of Fig. 3.6b (in $cm^{1/2}V^{1/2}$ units). In contrast to the linear dependences obtained for p-type samples, those derived for n-type samples could not be well approximated by the single straight line, showing rather super-linear dependence with the slope coefficient β increasing with electric field. Best linear fit for the high electric field parts gives $\beta = 2{,}6\times10^{-4}$ for n-16/42 and $\beta = 2\times10^{-4}$ for n-6/37 sample. Not also in Fig.3.6b, that the samples with denser DN and, accordingly, larger magnitudes of low-temperature STp/STn peaks, exhibit higher emission rates at lowermost electric fields.

3.5 Comparison of experimental and calculated Poole-Frenkel coefficients

Neutral charge in empty state of shallow STn/STp states as defined from CV/IV measurements agrees with the theory of 1D deformation induced dislocation states [2, 6]. This also implies that the observed emission enhancement from STn/STp traps could not be ascribed to the classical Poole-Frenkel phenomenon due to attractive Coulomb potential [41]. For the neutral traps emission enhancement can occur only by the phonon-assisted tunneling mechanism (Fig. 2.1) which is characterized by the squared electric filed linear dependence of the emission rate [30] that is not observed in our case.

The fact that the obtained Poole-Frenkel coefficients demonstrate a particular dependence on DN structure and density (Fig. 3.6b) as well as on the electric field strength argues in favor of the dislocation-strain-related origin of the observed phenomenon. Experimentally defined β-values in p-type samples $\beta_{p\text{-}/60} \approx 2{,}9\times10^{-4}$ and $\beta_{p\text{-}8/30} \approx 2{,}2\times10^{-4}$ correspond well with the theoretically predicted values for 60° dislocations with *b2* and *b1* orientations, respectively. Also, $\beta_{p\text{-}8/30}$ is close to the calculated β-coefficient for the screw dislocations. The mean Poole-Frenkel coefficient obtained on n-16/42 sample $\beta_{n\text{-}16/42} \approx 2{,}6\times10^{-4}$ is in a perfect agreement with the calculated one for 60° dislocations with *b1* orientation, see Table 2.1.

The critical interdislocation distances D_{min} estimated according to Eq. 2.16 for the lowest electric field in p-type samples of ~20 kV/cm and experimentally derived β-values appeared to be of about 16-18 nm for the mesh and ~30-40 nm for the row of dislocations. In n-type samples with the lowest field of ~14 kV/cm the corresponding distances D_{min} were estimated as 18-22 nm and 35-40 nm, respectively. Hence, the validity of the theory for isolated dislocation is satisfied for the row of 60° dislocations, but not for the square network of screw ones. This implies that the screw dislocations could not be responsible for the observed Poole-Frenkel effect. Additional argument for that is the dislocation-related Poole-Frenkel effect observed on p-/60 sample as its DN doesn't contain screw dislocations at all. Thus, the detected shallow STn/STp traps can be associated with the shallow 1D states of 60° dislocations.

On the other hand even the lowest values of Poole-Frenkel radius, which are ~5-6 nm for p-type and ~7-8 nm for n-type samples as estimated for the highest electric fields used in the experiments, exceed the typical dissociation width of 3-5 nm between the partial dislocations [39]. Therefore, the direct comparison of the Poole-Frenkel coefficients β calculated theoretically for the perfect dislocations with those obtained from ITS

experiments is correct even if the 60° dislocations at the bonding interface are indeed dissociated in two partials like it was observed previously for the screw dislocations.

The predominant *b1* or *b2* orientation in the investigated bounded samples could be realized due to an asymmetry of the tilt misorientation between the handle and the top wafers when, for example, the handle wafer has exact (100) orientation and the tilt between the bonded wafers appears due to misorientaion of the top wafer only or instead, when both wafers have had a particular tilt misorientaion component before the bonding process. Since the tilt angle was not controlled during the bonding process and arose as the result of wafers polishing inaccuracy, the formation of 60° dislocations with different orientations is probable at the bonding interface.

Theoretical calculations in paragraph 2.4 (Fig. 2.8b) have shown that with increase of the dislocation own charge the horizontal parts on $\beta(\sqrt{F})$ dependences are shifted towards the higher electric fields. Due to the low doping (10^{14} cm^{-3}) of n-type wafers, the relevant diapason of electric fields (Fig. 3.6b) falls into the region of $\sqrt{F}$ ~100-140, where the calculated $\beta(\sqrt{F})$-dependences just show an increase from ~2×10^{-4} to $2{,}5\times10^{-4}$ in Fig. 2.8d. This explains the super-linear increase of the emission rate from shallow STn traps (Fig. 3.6b) and relatively low value of β coefficient in n-6/37 sample with considerably higher density of states. Whereas in p-type samples (doping 10^{15} cm^{-3}) relevant diapason of electric fields falls into the region of nearly constant $\beta(\sqrt{F})$-dependences (Fig. 2.8b). Also, the higher emission rates at lowermost electric fields observed in the samples with higher STn/STp peaks magnitudes (i.e. with higher dislocation line charges) confirm that DN charge increases the emission rate as it was supposed in paragraph 2.4.

Similar combination of factors (low doping and high dislocation own charge) explains also the shift of low-temperature shoulder of STn peak towards the higher temperatures (Fig. 3.5b). The smaller value of Poole-Frenkel coefficient β calculated in paragraph 2.2 for 60^0 dislocations of *b1* orientation implies that the attractive part of dislocation deformation potential directed predominantly towards the metal, i.e. against the direction of electric field F_{sc} (Fig. 3.3). Just after the end of the filling pulse, the occupation of shallow traps is high (especially at T= 40-50K corresponding to the appearance of low-temperature shoulder of STn peak), so they are under the action of both their own and external electric fields. In such a case Eq. 3.3 is not valid anymore and the DN charge has to be accounted (see Eq. 3.8).

At small reverse biases when external electric field is weak but the traps occupation is high so that the electric field in the top layer of the structure exhibits an inversion with respect to its bulk part (fields F_m and F_{sc} in Fig. 3.3), the enhanced carrier emission proceed both towards the metal and towards the semiconductor bulk (i.e. in the full sector of angles where the deformation potential has an attractive character) via the potential barrier lowered by the own DN charge. With the increase of the reverse bias the field F_{sc} increases but F_m in the top layer decreases, thus the emission to the left side of DN plane (Fig. 3.3) occurs via higher potential barrier leading to the high-temperature shift of the low-temperature shoulder.

3.6 Impact of DN-related states occupancy on thermoemission barrier

As it was pointed out earlier, the direct retrieval of energy distribution of shallow state density immediately from broadened DLTS peaks is not possible. To define the exact energy position of dislocation-related STn/STp states with respect to the conduction/valence band we utilized the fact that under the application of forward bias voltages U_f the investigated structures behave similar to the grain boundaries, where the Fermi level position at the interface during the DLTS measurements controls both the upper energy level till which the traps can be filled with charge carriers during the application of a filling pulse of $U_f + \Delta U$ as well as the lower energy level till which the traps will be emptied after the restoration of the initial bias voltage U_f (band diagram in Fig. 3.3). Keeping the difference between the pulse and the bias voltages small, the interface traps can be filled within the narrow energy interval. This method is known as "energy-resolved DLTS" (ER-DLTS) and was successfully applied previously for the investigation of the semiconductor-insulator interface states [53].

The results of ER-DLTS measurements on n-16/42 sample are presented in Fig. 3.7a where the set of narrow DLTS peaks obtained at different forward bias voltages and a constant pulse amplitude ΔU=50 mV is shown together with the standard DLTS spectrum. One can note in Fig. 3.7a that the temperature ranges of ER-DLTS peaks passed exactly between the right- and the left- shoulders of the broadened STn peak.

The analysis of ER-DLTS peak shapes revealed that they can be well fitted by the theoretical model developed for the emission from single levels, thus confirming the reliability of energy values retrieved from the Arrhenius plots that are shown in Fig. 3.7b. The thermoemission enthalpies of ER-DLTS peaks vary in a wide interval from E_c –150 meV down to E_c – 60 meV. Note that the sharp turn of DLTS signal at 35-40 K is caused by the free carrier freeze-out, thus making the precise determination of the lower energetic limit impossible.

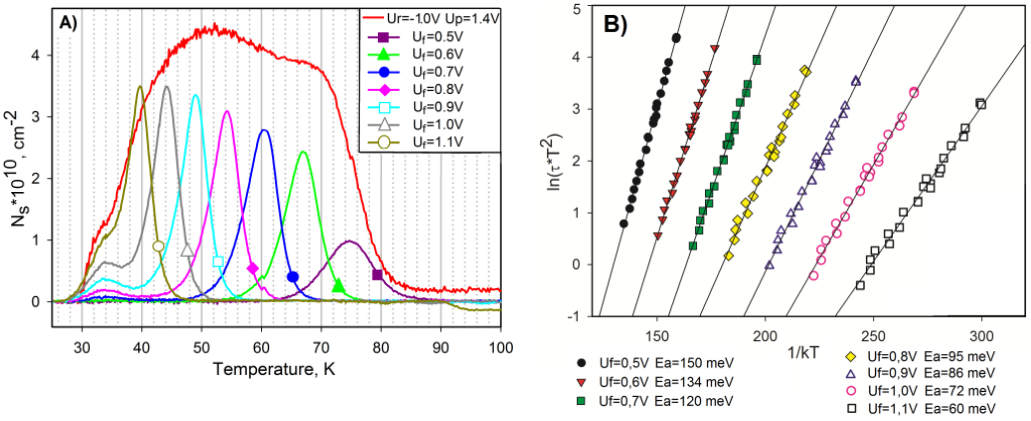

Figure 3.7 (a) Set of ER-DLTS spectra of n-16/42 sample measured with forward bias voltages U_f (shown in the legend) and filling pulse height of ΔU= 50 mV. For comparison, standard DLTS spectrum measured with U_r= –1 V and U_p=1,5 V is shown, too. (b) Arrhenius plots for the corresponding ER-DLTS peaks with the calculated values of activation enthalpy.

However, the magnitudes of ER-DLTS peaks do not reflect the true density of states [53]. In order to obtain the carrier density N_s captured by DN electronic states responsible for the Fermi-level pinning observed as a step on CV curves at 40K, the relation obtained from the solution of Poisson equation for Schottky diode with the charged interface at the depth x_d was used (see Eq. 3.1)

$$\frac{\varepsilon S^2}{C^2} = \frac{2}{qN_D}(U + \frac{qN_s}{\varepsilon} x_d) \tag{3.4}$$

The last term in the brackets is negligible at sufficiently high reverse biases but becomes significant at forward bias voltages when Fermi level is pinned by the DN interface states. Hence, carrier density N_s can be extracted from the voltage difference ΔU between the experimental $1/C^2$ curve measured in full voltage ranges and the straight-line extrapolation in the region of bias voltages when N_s=0, see Fig. 3.9a. Required values of N_s can be found then as

$$N_s(U_f) = \frac{\varepsilon \Delta U(U_f)}{qx_d} \tag{3.5}$$

The results of the calculations derived from a set of $1/C^2$ curves measured in a temperature range of 40-60K were combined with the $E_a(U_f)$ dependence obtained from ER-DLTS Fig. 3.7b to represent the energy distribution of the captured electrons.

The result for n-16/42 sample is depicted in Fig. 3.8b, showing that the number of electrons at DN-related states increases linearly when the state energy goes towards the bottom of conduction band and reaches finally the value of $1{,}8\times10^{11}$ cm^{-2} (what is approximately 4-5 times higher than the values estimated from the amplitude of broadened STn peak). This conclusion is in accordance with previous data obtained on the same samples by admittance spectroscopy technique [54]. In both cases, however, the upper energy limit of density of states could not be reached.

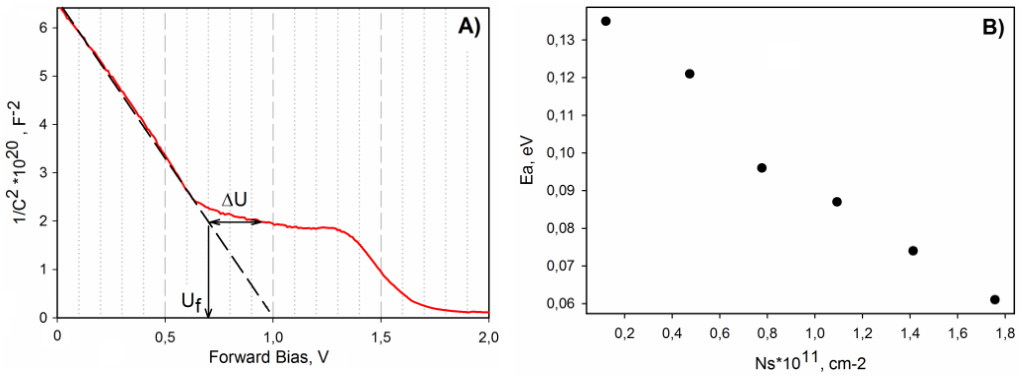

Figure 3.8 (A) $1/C^2$ curve of n-16/42 sample as measured at T=40K. (B) Energy distribution of electrons captured at shallow states in n-16/42 sample as retrieved from $1/C^2$ and ER-DLTS results.

3.7 “Band-like” behavior of DLTS peaks

Since the Fermi level position at the bonding interface defines the filling grade of the DN-related states, the population of shallow DN-traps can be controlled by the variation of the filling pulse magnitude U_p instead of the filling pulse duration as in case of bulk distribution of traps [22]. Figure 3.9 represents the DLTS spectra of p-8/30 and n-16/42 samples measured with different magnitude of filling pulse voltage U_p and constant reverse bias voltage. One can see that with the increase of filling pulse voltage from 0,5 V till 0,9 V along with increase of STp peak amplitude its temperature position shifts towards the lower temperatures, whereas the high-temperature shoulders almost coincide. Similarly, the shift of the maximum position was observed for STn peak as well (Fig. 3.9b). Further increase of the pulse voltage led to the significant broadening of the STn peak (and less pronounced broadening of STp peak) from the low-temperature side keeping the magnitude nearly the same until the saturation occurs at U_p ~1,5 V. Such kind of behavior unambiguously implies that the activation energy for carrier thermoemission decreases with the increase of the state occupancy. Previously, similar variation of DLTS spectrum was reported for nickel silicide precipitates and was attributed to the ‘band-like states’, i.e. to a band of electronic states with rapid interstate exchange [22].

Theoretical calculations discussed in paragraph 2.4 suggest another interpretation for the observed phenomenon: the “band-like” behavior of DLTS line can be a result of the thermoemission barrier lowering with the increase of the dislocation line charge. Following this supposition the theoretical calculations of the barrier lowering for electron thermoemission were performed for n-type Si. Due to the radial symmetry of electrostatic potential of charged dislocation line (Eq. 2.17) and the particular shape of dislocation deformation potentials for conduction band which has rather broad angular interval of attractive behavior (~250° in Fig. 2.4c when considering for all three sub-bands), in the first approximation one can neglect the angular dependence of Ψ_c and use its effective value that can be taken approximately

$$\Psi = \frac{\Xi_d \boldsymbol{B}}{4\pi} = 2 \cdot 10^{-8}\ \text{cm/V} \qquad (3.6)$$

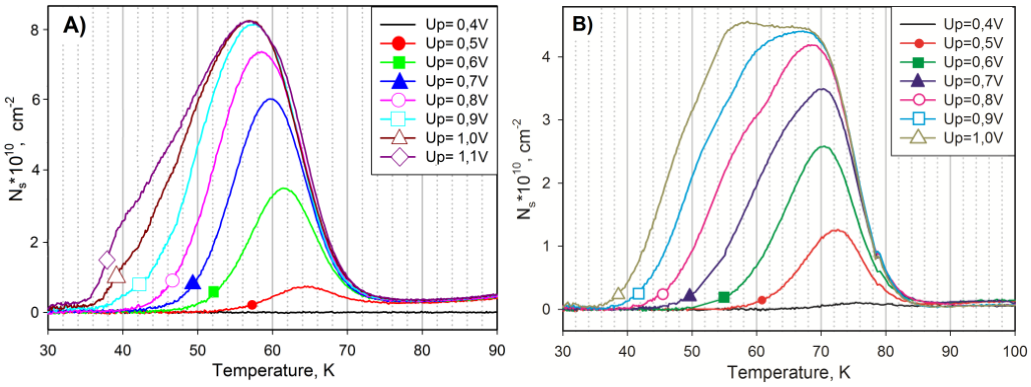

Figure 3.9 Variations of low-temperature STp peak in p-8/30 (A) and STn peak in n-16/42 (B) samples with the increase of the filling pulse voltage U_p. Reverse bias U_r= *–1V*, pulse duration 1 ms, rate window t_w= 20 ms.

or from the experimentally derived β-value, what gives generally the same result

$$\Psi = \frac{\beta^2}{4} \approx 1,7 \div 2 \cdot 10^{-8}\ \text{cm/V} \tag{3.7}$$

Following Eq. 2.20 barrier lowering was calculated as a function of dislocation line charge N_l for the case of F=0 (see Fig. 3.10 dashed curve) and in the presence of electric field by Eq. 2.22 as a function of applied forward bias (Fig. 3.10 solid curve). General expression for the electric field at the position of DN can be obtained by solving the Poisson equation taking into account the charge Q_s collected by DN-states,

$$F_0(\Delta U) = \sqrt{2\frac{qN_D}{\varepsilon}(V + \frac{qN_s x_d}{\varepsilon})} - \frac{qN_D}{\varepsilon} x_d - \frac{qN_s(\Delta U)}{\varepsilon} \tag{3.8}$$

The second term in the equation can be neglected for n-type samples (N_D~10^{14} cm^{-3} and x_d ~160 nm). Further, for the electric field in the range of forward biases when the DN-barrier is stabilized by the Fermi-level pinning on shallow states the last term in Eq. 3.8 can be replaced by Eq. 3.5 so that

$$F_{0\,forward}(\Delta U) = \sqrt{2\frac{qN_D}{\varepsilon} E_t} - \frac{\Delta U}{x_d} \tag{3.9}$$

where E_t ~ 0,15 eV is the approximate DN barrier height as follows from the deepest energy level derived from ER-DLTS measurements. The results of the calculations together with the experimental data of ER-DLTS are presented in Fig. 3.10.

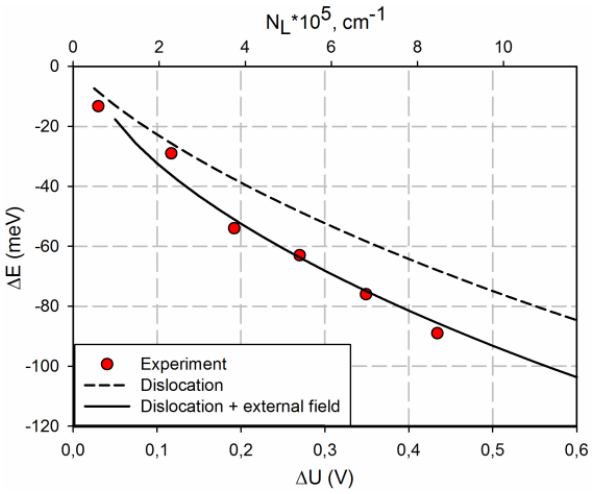

Figure 3.10 The reduction of the activation energy for electron thermoemission from the local electronic states in the core of 60° dislocation as a function of number of electrons in the dislocation core and of applied forward bias to the Schottky diode with the bonded interface at the depth of 160 nm. Dashed line – was calculated according to the model of negatively charged dislocation line with an attractive deformation potential; solid line – the same but with adding of external electric field of the diode; dots – the data of ER-DLTS.

Experimental values of the line charge of dislocations at the bonded interface were obtained as interface charge density per cm^2 from capacitance-voltage data Fig. 3.8 multiplied by the interdislocation distance of 60° dislocations obtained from TEM, whereas the reduction of the barrier height as a difference of $E_t - E_a(\Delta U_f)$ where $E_a(\Delta U_f)$ were obtained combining the results of ER-DLTS and trap density calculation Eq. 3.5.

Careful examination of Fig. 3.10 reveals that at low bias voltages the experimental points coincide well with the theoretical curve calculated for the own dislocation field only, whereas with the further increase of forward bias (i.e. with increase of the dislocation line charge) they become closer to the curve calculated by taking into account the external electric field as well. Note, that the theoretical curves were obtained without any fitting variables, by taking as an input parameters the literature values of deformation potentials for X-band in Si, the experimentally determined depth of the interface and a reasonable value for r_{core}=1 nm.

This suggests that the 'band-like' behavior of STp/STn peaks and their broadened shape can be a result of continuous lowering of the potential barrier for carrier thermoemission with increase of the occupation rate of the dislocation core states. Since the broadened DLTS peak in Si samples with nickel silicide nanoprecipitates was ascribed to the core states of the dislocation ring bounding the flat precipitate [25], generally similar effect of the barrier lowering might be expected for such kind of defects, too.

4. CONCLUSIONS

As a result of theoretical calculations and experimental investigations of n- and p-type bonded samples with various structures of dislocation networks, the following novel facts were established:

- the theory of the dislocation-related Poole-Frenkel effect that is the barrier lowering for carrier thermoemission from the core states of dislocations due to the superposition of the attractive part of dislocation deformation potential and the potential of external electric field was developed based on the general theory of deformation potential in semiconductors. Detailed calculations were made for hole and electron emission from the states of screw and 60º dislocations to the valence and conduction band of Si, respectively. It was found that the corresponding values of Poole-Frenkel coefficient exceed the value predicted for singly charged Coulomb center.

- an additional lowering of the potential barrier for carrier thermoemission was shown to occur due to the presence of the own electric field of charged dislocation line

- DLTS measurements have revealed the presence of deep and shallow DN-related states in the upper and the lower parts of Si band gap. Deep states were identified with point defects or defect clusters (probably interstitials and oxygen related) in the vicinity of dislocations, whereas shallow STn/Stp traps – with the deformation induced shallow 1D dislocation states. Donor-like behavior was found for the defect levels in the lower half of band gap and acceptor-like – for the levels in the upper half.

- an enhancement of carrier thermoemission in external electric field following the Poole-Frenkel law was found for STp/STn shallow traps in all investigated bonded samples and the experimentally determined values of the Poole-Frenkel coefficient agreed well with the calculated ones for 60° dislocations.

- the dependence of the activation energy for carrier thermoemission on the occupancy degree of shallow STn/STp states was revealed by experiments and a good agreement with the results of the theoretical calculations was established. This fact suggests an alternative explanation for the broadening of the DLTS peak towards the lower temperatures with the increase of dislocation-related states occupancy degree.

- reduction of the thermoemission barrier both with increase of the trap occupancy with charge carriers and in external electric field due to the Poole-Frenkel effect may serve as a fingerprint of electronic states located in a close vicinity from the dislocation core.

REFERENCES

[1] W. Schröter and H. Cerva, Solid State Phenomena 85-86 (2002) 67.
[2] V. Kveder and M. Kittler, Materials Science Forum 590 (2008) 29.
[3] M. Seibt, R. Khalil, V. Kveder, and W. Schröter, Applied Physics A 96 (2009) 235.
[4] B. Sopori, V. Mehta, S. Devayajanam, M. Seacrist, G. Shi, J. Chen, A. Deshpande, J. Binns, and J. Appel, Solid State Phenomena 205-206 (2014) 55.
[5] J.-L. Farvacque and P. Francois, Physica status Solidi B 223 (2001) 635.
[6] S. Marklund, phys. stat. sol. (b) 85 (1978) 673.
[7] M. Brohl, M. Dressel, H. W. Helberg, and H. Alexander, Philosophical Magazine B 61 (1990) 97.
[8] V. Kveder, Y. Osipian, and A. Shalynin, JETP 61 (1985) 182.
[9] M. Kittler, X. Yu, T. Mchedlidze, T. Arguirov, O. Vyvenko, W. Seifert, M. Reiche, T. Wilhelm, M. Seibt, O. Voss, W. Fritzsche, and A. Wolff, Small 3 (2007) 964.
[10] Электронные свойства дислокаций в полупроводниках, под редакцией Ю.А. Осипьяна, Издательство:Эдиториал УРСС (2000)
[11] A. Bondarenko, O. Vyvenko, I. Kolevatov, I. Isakov, and O. Kononchuk, Solid State Phenomena 178-179 (2011) 233.
[12] V. Kveder, M. Badylevich, W. Schröter, M. Seibt, E. Steinman, and A. Izotov, physica status solidi (a) 202 (2005) 901.
[13] M. Kittler and M. Reiche, ADVANCED ENGINEERING MATERIALS 11 (2009) 249.
[14] M. Reiche, M. Kittler, M. Krause, and H. Übensee, Phys. Status Solidi C 10 (2013) 40.
[15] D. V. Lang, Journal of Applied Physics 45 (1974) 3023.
[16] P. Omling, E. R. Weber, L. Montelius, H. Alexander, and J. Michel, PHYSICAL REVIEW B 32 (1985) 6571.
[17] V. V. Kveder, Y. A. Osipyan, W. Schröter, and G. Zoth, Physica Status Solidi A 72 (1982) 701.
[18] C. Kisielowski and E. R. Weber, PHYSICAL REVIEW B 44 (1991) 1600.
[19] D. Cavalcoli, A. Cavallini, and E. Gombia, PHYSICAL REVIEW B 56 (1997) 10208.
[20] L. C. Kimerling and J. R. Patel, Applied Physical Letters 34 (1979) 73.
[21] A. Castaldini, D. Cavalcoli, A. Cavallini, S. Binetti, and S. Pizzini, Applied Physical Letters 86 (2005) 162109.
[22] W. Schröter, J. Kronewitz, U. Gnauert, F. Riedel, and M. Seibt, PHYSICAL REVIEW B 52 (1995) 13726.
[23] W. Schröter, H. Hedemann, V. Kveder, and F. Riedel, J. Phys.: Condens. Matter 14 (2002) 13047.
[24] P. Omling, L. Samuelson, and H. G. Grimmeiss, JOURNAL OF APPLIED PHYSICS 54 (1983) 5117.
[25] F. Riedel and W. Schröter, Physical Review B 62 (2000) 7150.
[26] V. Kveder, M. Kittler, and W. Schröter, PHYSICAL REVIEW B 63 (2001) 115208.
[27] V. Kveder, A. Shalynin, E. Steinman, and A. Izotov, Solid State Phenomena 57-58 (1997) 299.

[28] V. V. Kveder, E. A. Steinman, S. A. Shevchenko, and H. G. Grimmeiss, PHYSICAL REVIEW B 51 (1995) 10520.
[29] A. Castaldini, D. Cavalcoli, A. Cavallini, and S. Pizzini, PHYSICAL REVIEW LETTERS 95 (2005) 076401.
[30] S. D. Ganichev, E. Ziemann, W. Prettl, I. N. Yassievich, A. A. Istratov, and E. R. Weber, PHYSICAL REVIEW B 61 (2000) 10 361.
[31] H. Hedemann and W. Schröter, Solid State Phenomena 57-58 (1997) 293.
[32] F. Riedel, H. Hedemann, and W. Schröter, Nuclear Instruments and Methods in Physics Research A 476 (2002) 596.
[33] J. Frenkel, PHYSICAL REVIEW 54 (1938) 647.
[34] M. Shimbo, K. Furukawa, K. Fukuda, and K. Tanzawa, Journal of Applied Physics 60 (1986) 2987.
[35] M. Reiche, Materials Science Forum 590 (2008) 57.
[36] M. Reiche, Physica Status Solidi C 6 (2009) 633.
[37] W. Bollmann, Crystal Defects and Crystalline Interfaces, Springer Verlag, New York, Heidelberg (1970)
[38] K. Rousseau, J. L. Rouviere, F. Fournel, and H. Moriceau, APPLIED PHYSICS LETTERS 80 (2002) 4121.
[39] J. L. Rouviere, K. Rousseau, F. Fournel, and H. Moriceau, Applied Physics Letters 77 (2000) 1135.
[40] J. L. Hartke, JOURNAL OF APPLIED PHYSICS 39 (1968) 4871.
[41] W. R. Buchwald and N. M. Johnson, JOURNAL OF APPLIED PHYSICS 64 (1988) 958.
[42] J. P. Hirth and J. Lothe, Theory of dislocations, McGraw-Hill, New York (1970)
[43] M. Trushin, O. Vyvenko, V. Vdovin, and M. Kittler, Journal of Physics: Conference Series 281 (2011) 012009.
[44] M. Trushin, Ph.D. thesis BTU Cottbus http://nbn-resolving.de/urn:nbn:de:kobv:co1-opus-22841 (2011)
[45] G. L. Bir and G. E. Pikus, Symmetry and deformation effects in semiconductors, Wiley, New-York (1974)
[46] A. Romanov, P. Petroff, and J. Speck, Applied Physics Letters 74 (1999) 2280.
[47] H. Veth and M. Lannoo, Philosophical Magazine B 50 (1984) 93.
[48] O. Kononchuk, F. Boedt, and F. Allibert, Solid State Phenomena 131-133 (2008) 113.
[49] T. Akatsu, R. Scholz, and U. Gosele, JOURNAL OF MATERIALS SCIENCE 39 (2004) 3031.
[50] M. Trushin, O. Vyvenko, T. Mchedlidze, M. Reiche, and M. Kittler, Physica Status Solidi C 8 (2011) 1371.
[51] A. Loshachenko, A. Bondarenko, O. Vyvenko, and O. Kononchuk, Phys. Status Solidi C 10 (2013) 36.
[52] I. Isakov, A. Bondarenko, O. Vyvenko, V. Vdovin, E. Ubyivovk, and O. Kononchuk, Journal of Physics: Conference Series 281 (2011) 012010.
[53] N. M. Johnson, J. Vac. Sci. Technol. 21 (1982) 303.
[54] I. Kolevatov, M. Trushin, O. Vyvenko, M. Kittler, and O. Kononchuk, Phys. Status Solidi C 10 (2013) 20.

INCLUDED ARTICLES

PI

ELECTRONIC STATES OF OXYGEN-FREE DISLOCATION NETWORKS PRODUCED BY DIRECT BONDING OF SILICON WAFERS

M. Trushin, O. Vyvenko, T. Mchedlidze, O. Kononchuk, M. Kittler.

Published in: *Solid State Phenomena 156-158, p. 283, 2010.*

Solid State Phenomena Vols. 156-158 (2010) pp 283-288
online at http://www.scientific.net

Electronic States of Oxygen-free Dislocation Networks Produced by Direct Bonding of Silicon Wafers

M. Trushin[1,a], O. Vyvenko[1,2,b], T. Mchedlidze[1,c], O. Kononchuk[3] and M. Kittler[1,4]

[1] IHP/BTU Joint Lab, Konrad-Wachsmann-Allee 1, 03046 Cottbus, Germany

[2] V. A. Fok Institute of Physics, St. Petersburg State University, Ulyanovskaya 1, 108594 St. Petersburg, Russia

[3] SOITEC, Parc des Fontaines, F-38560 Bernin, France

[4] IHP microelectronics, Im Technologiepark 25, 15236 Frankfurt (Oder), Germany

[a] trushmax@tu-cottbus.de, [b] vyvenko@gmail.com, [c] teimuraz.mtchedlidze@tu-cottbus.de

Keywords: Dislocation networks, electronic states of dislocations, DLTS, Pool-Frenkel effect, photoluminescence

Abstract. The results of experimental investigations of the dislocation-related DLTS-peaks originated from the dislocation networks (DN) are presented. Samples with DNs were produced by direct bonding of p-type silicon wafers and no enhancement of oxygen concentration was detected near the DN plane. Origins of the DLTS peaks were proposed and a correlation with the dislocation-related photoluminescence data was established based on known dislocation structure of the samples. Two types of shallow DLTS peaks exhibited Pool-Frenkel effect, which could be linked to the dislocation deformation potential. One of the shallow DLTS peaks was related to straight parts of screw dislocations and another - to the intersections of the dislocations.

Introduction

The dislocation networks (DN) produced by the direct bonding of silicon wafers recently attract an increasing interest due to their potential application in microelectronics as effective light emitters and as perfect conductors (for review see [1]). On the other hand, the DN with the structure pre-determined by the bonding conditions could be used as a model for deeper understanding of properties of dislocations in silicon. Indeed, the density and the types of dislocations in DN are well defined by a misorientation of the surfaces, i.e. by twist and tilt angles between the bonded wafers.

For the case of the investigations by means of deep-level transient spectroscopy (DLTS) method, DNs have special advantages in comparison with the samples containing randomly distributed dislocations (see e.g. [2] and references therein): (i) the DN is strictly parallel to the sample surface; (ii) the distance between the DN and the sample surface can be controlled. Therefore, in combination with the known structure of DN these allow straightforwardly interpret DLTS-results and compare them with the data obtained by other experimental methods, such as photoluminescence.

In previous reports the investigated samples contained large density of oxide precipitates ("oxide islands") at the bonding interface besides the DN itself (see [1] and references therein). The presence of the precipitates complicated investigation of DN properties due to their influence on the electro-physical properties of the material. The experimental results reported in the present work were obtained on the samples where the oxygen concentration at the DN was the same as in the bulk and where the oxide precipitates were not detected by transmission electron microscopy (TEM).

Samples and experimental

Samples were fabricated by direct bonding of 200 mm p-type Si wafers (WB) with (001) surface orientations in hydrophilic process, i.e. the surfaces of the wafers were covered with native oxide layer before the bonding process [3]. Doping level of the wafers was ~10^{15} atoms/cm^3 of boron. Detailed description of the bonding procedure can be found elsewhere [3-5]. After the bonding and a thinning procedure of the top layer, a dislocation network was located at the depth of 170 nm from the sample surface. In order to dissolve the interfacial native oxide layer (INOL), samples were annealed at 1200°C in high purity conditions [3]. After the annealing SIMS investigations did not reveal any variations of oxygen concentration near to the bonding interface.

Wafers were bonded with different twist angles (α_{TW}). A small tilt angle (α_{TI}, ~0.5°) was a result of non-uniformity of wafers polishing. Exact values of tilt and twist angles were defined from X-ray diffraction measurements. The average distance between dislocations in the network as a function of the misorientation angle can be estimated according to the expression [5]:

$$d \sim b / \sin\vartheta , \qquad (1)$$

where b is the Burgers vector of a dislocations and ϑ is the misorientation angle. For the dislocations in Si, b = a/2 <110> holds with a = 0.543 nm. The characteristics of the investigated DNs with distances between screw and edge dislocations as well as their average densities calculated from Eq. 1 are presented in Table 1. It should be noted that while a good correspondence between the distances calculated from Eq. 1 and TEM data was found for the small, i.e. 1-3°, misorientation angles, application of Eq. 1 for the larger angles (6° and 30° in our case) is ambiguous due to disturbances of dislocation network caused by the overlapping of the dislocation strain fields.

To produce Schottky contacts for DLTS measurements, 100 nm-thick titanium dots with 1.5 mm diameter were evaporated on the oxide free front surface of all samples. Ohmic contacts were prepared by rubbing of InGa on the rear side of the samples. DLTS measurements were performed by means of transient Fourier spectroscopy system DL-8000 (Accent). Principles of the method and the system can be found elsewhere [6].

Photoluminescence was excited by an Ar-ion laser emitting at 514 nm wavelength with excitation power of 100 mW and the beam was focused to a spot of 100 μm in diameter. The excitation beam was chopped at ~30 Hz frequency for lock-in detection. The emitted light was analyzed with a monochromator and detected by a liquid-nitrogen cooled Ge detector system. More details about PL measurements on these samples can be found elsewhere [7].

Sample	α_{TW}	α_{TI}	D_{SC} 10^6 cm^{-1}	D_{ED} 10^6 cm^{-1}	D_{tot} 10^6 cm^{-1}	d_{SC} nm	d_{ED} nm
L1	1°	0.54°	0.46	0.25	0.71	22	41
L2	3°	0.5°	1.4	0.22	1.62	7.3	44
L3	5.8°	0.67°	2.6	0.31	2.91	3.8	33
L4	29.9°	0.45°	13.4	0.2	13.6	0.7	49

Table 1. Abbreviation used: α_{TW}, α_{TI} - the twist and tilt misorientation angles; D_{SC}, D_{ED}, D_{tot} -densities of screw, edge dislocations and their sum; d_{SC}, d_{ED} - average distances between screw and edge dislocations.

Results and Discussion

PL measurements. PL spectra measured from the samples are presented in Fig.1. The strongest dislocation related luminescence (DRL) spectra consisting mainly of D1 peak at ~0.8 eV was observed from L2 sample. D1 peak was less intensive in L1 sample and was under detection limits in L3 and L4 samples. Extremely weak DRL (mainly D2 and D3 peaks) was found in L3 sample.

Band-to-band (BB) luminescence showed non-monotonic behavior as a function of the twist angle. It was found to be the maximal in L4 sample. Detailed description of PL results for the samples and their interpretation can be found elsewhere [7].

DLTS results. Examples of the DLTS spectra obtained on L1-L4 samples are shown in Fig. 2. DLTS signal-profiling measurements revealed that the origin of the signal in the entire temperature region was located within a narrow region near to the sample surface. An example of such profiling is presented in Fig. 3. In the case under consideration the distribution of the traps is two-dimensional and the relation between the surface density of emitted holes, p_s, and the DLTS signal, dC, is given by:

$$p_s = -\frac{A^2\varepsilon^2}{x_d} eN_A \frac{dC}{C^3}, \qquad (2)$$

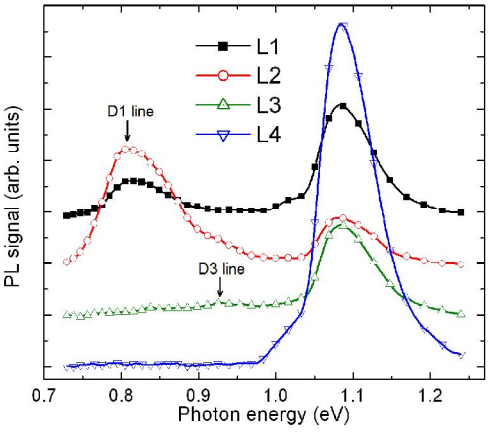

Figure 1. PL spectra detected from L1-L4 samples at 300 K and at 200 mW excitation power. Assignments of the curves are shown in legend.

where ε is dielectric constant, e is elemental charge, x_d is the depth of the dislocation network, C is the diode capacitance, A is the diode area and N_A is the net shallow acceptor density. To account for the Eq. 2, the DLTS signals presented below are normalized to C^3- value.

The low twist-angle samples L1 and L2 showed similar features in DLTS spectra (Fig. 2, left): a low temperature peak and a set of unresolved peaks at 100-250K. The maximum of the main peak in L1 sample, labeled as SL in Fig. 2, is located at a temperature which is 10 K lower than that for the peak QD in L2 sample. Careful examination of the DLTS spectrum of L1 sample reveals that the high temperature side of SL peak has a shoulder just at the position of the QD peak indicating that the QD peak is also presented in the spectrum of L1 sample (see also Fig. 4). The ratio of the magnitudes of the QD peak in L1 and L2 samples is approximately 1:10.

The part of L1 and L2 DLTS spectra between 100 K and 250 K is composed of a set of at least four peaks with the similar or close positions of maximums on temperature scale for both samples.

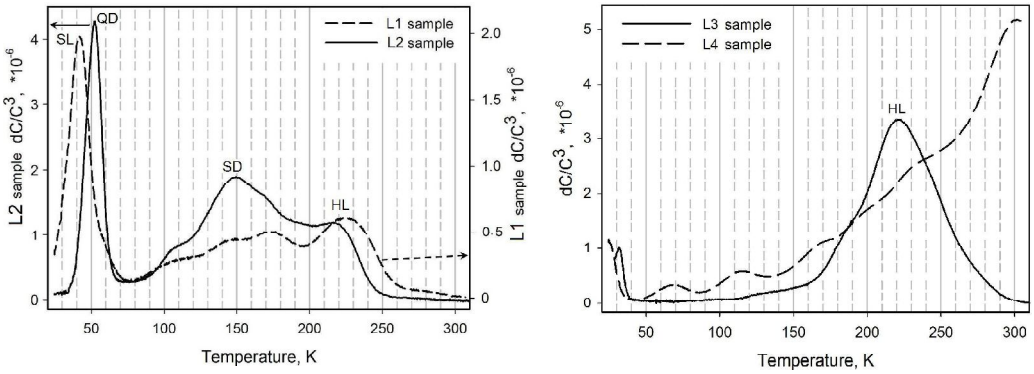

Figure 2. DLTS spectra of L1 and L2 samples (left), and of L3 and L4 samples (right). DLTS-scan parameters: filling pulse duration t_p=100μs, reverse bias U_b=1V, filling pulse voltage U_p= –1V, rate window t_w=20ms. Note different vertical axis scales for the curves in the left figure.

The main difference in the spectrum in this temperature region is the enhancement of the magnitude of the peak marked as SD with the increase of the twist angle from 1° to 3°. Unfortunately, strong overlapping of the peaks complicates determination of their emission characteristics.

DLTS spectra of the large twist-angle samples L3 and L4 differ significantly from that of the low twist-angle samples L1-L2 (see Fig. 2, right). The main feature of DLTS spectrum of L3 sample is an unresolved peak HL, located at around 220 K that could be also recognized in the spectra of L1 and L2 samples. The magnitude of this peak increases with the twist angle. The spectrum for L4 sample shows a set of overlapping DLTS peaks with continuously growing magnitude up to 300 K. The positions of low temperature peaks in L3 and L4 samples are shifted to the lower temperatures with respect to the position of SL and QD peaks in L1-L2 samples and are close to the temperature of freeze-out of shallow acceptors.

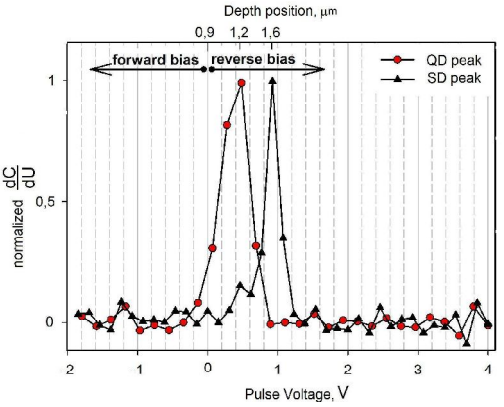

Figure 3. Traps density profiles normalized to their maximum value derived from the refilling pulse voltage dependence of the magnitude of DLTS peaks at T=53 K (QD peak) and at T=150K (SD-peak) in the sample L2. The voltage difference of the profile peaks (~0.4 V) is due the difference of the energetic level positions in band gap. Applied bias voltage was U_b=5 V.

Traps density profiles calculated as the derivative of the dependence of the DLTS signal on the refilling pulse voltage are presented in Fig. 3. The width of the profile peaks is very close to the Debye screening length in the investigated samples, reflecting "plane-like" distribution of the traps. The depth scale at the top Fig. 3 corresponds to the depletion region width, calculated from the stationary capacitance values. The approximation of the depth position of the trap plane, calculated conventionally from the trap energy level and the doping concentration [8] gives the value of ~ 700 nm that is significantly larger than the thickness of the top layer before the thermal treatment, i.e. 170 nm. The reason of this discrepancy is under investigation. As a supposition we could propose a local drop of the hole potential at the interface.

Pool-Frenkel effect. It was found that SL and QD peak positions detected in L1 and L2 samples were shifted toward the lower temperatures with the increase of applied reverse bias, i.e. with the increase of the electric field in the depletion region (see Fig. 4). Detailed examination of the shapes of DLTS peaks and their changes under bias voltage variation confirmed that DLTS signal was composed mainly from two broadened peaks SL and QD.

The activation enthalpies for the hole thermo-emission ΔE_a calculated from the Arrhenius plots at various reverse bias voltages as a function of electrical field followed Pool-Frenkel law for the both levels (see Fig. 5). The dependences could be approximated by expressions:

$$\Delta E_a(QD)=0.12 - 2.45e\text{-}4 \sqrt{E(V/cm)} \quad (3)$$

and

$$\Delta E_a(SL)=0.13 - 3.78e\text{-}4 \sqrt{E(V/cm)} \quad (4)$$

for QD and SL peaks consequently, giving practically the same value of the trap level position in the bandgap at zero field but showing different slopes.

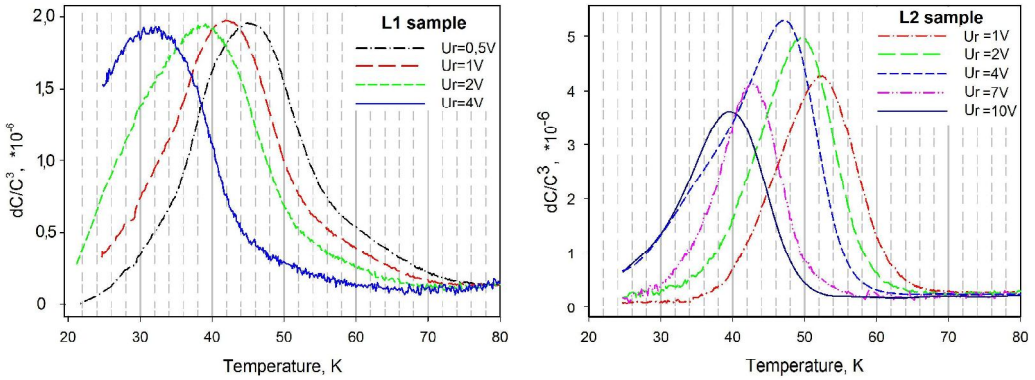

Figure 4. Low temperature part of DLTS spectra of L1 sample (left) and L2 sample (right) measured with different reverse bias voltages. DLTS-scan parameters: filling pulse duration t_p=100μs, filling pulse voltage U_p= –1V, rate window t_w=20ms, reverse bias voltages U_r are shown in the legends.

Possible origins of the DLTS peaks

The magnitude of the SD-peak in L2 sample was approximately three times larger than that in L1 sample, correlating with a threefold larger density of screw dislocations in L2 sample in comparison with L1. The ratio of the magnitudes of QD-peaks between L1 and L2 samples was of about ten, i.e. was equal to square of the screw dislocation density ratio between the samples. From this correlation we can suppose, that SD and SL peaks are related to regular segments of screw dislocations while QD-peak is related to intersections of screw dislocations.

The presence of Pool-Frenkel-like dependence for $\Delta E_a(E)$ indicates that the defects responsible for QD and SL DLTS-peaks exhibit an attractive potential for the holes that is inversely proportional to the distance from the trap. According to the theory [8, 9], the pre-factor of the field dependence for the Coulomb potential increases from 1.1e-4 $V^{-1/2}cm^{1/2}$ for three-dimensional (3D) case to 4.4e-4 $V^{-1/2}cm^{1/2}$ for one-dimensional (1D) case. Previously reported pre-factor values for the impurities with the Coulomb potential (see [9] and references therein) were close to the theoretical value for 3D case. The fact that pre-factor values found in this work for SL and QD levels are significantly larger than the later can be explained by a non-Coulombic origin of the potential. We suggest this could be due to a deformation potential of a dislocation that is also inversely proportional to the distance from its core.

The difference between the pre-factor values for SL and QD levels can be explained then to be due to the different dimensionality of the potential within the regular dislocation segments and of intersections of the dislocations. The intersections can be considered as a kind of quantum dots (QD – quantum dot) that have higher dimensionality of its potential (3D) and, accordingly, a lower pre-factor value than the 2D regular dislocation segments. That is in accordance with the suppositions made above.

The zero-field values of the activation energy for the hole emission from SL and QD levels is noticeably larger than that calculated theoretically for the shallow hole states, confined in deformation potential of

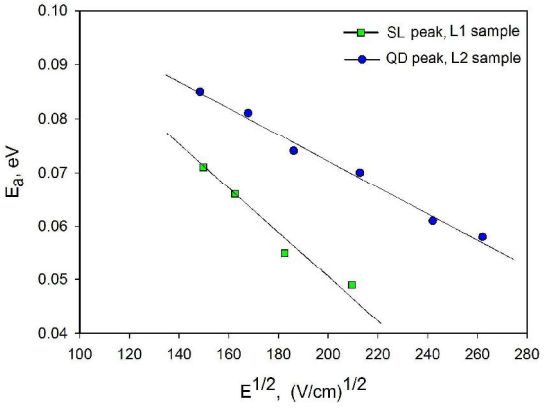

Figure 5. Activation energies for hole thermo-emission from SL and QD traps versus square root of the electrical field in the structure.

screw dislocation (47 meV) [10] and observed experimentally (70 meV) in plastically deformed samples [11]. Accordingly, these levels could originate from the some defects in the dislocation core that are neutral in the empty state. Another possibility is that the states of individual dislocations become deeper due to the effect of the overlapping of their strain fields. Theoretical calculations of the deformation potential levels of the dislocations within a dense dislocation network and of Pool-Frenkel effect for dislocation deformation potential are necessary to clarify this problem.

A correlation could be seen between PL and DLTS results for the L1 and L2 samples. The magnitudes of SL and SD DLTS-peaks and the intensity of D1 peak in PL spectra have similar differences between L1 and L2 samples indicating that all that features are related to the same kind of dislocation related defects. Moreover, shallow levels dominating in these samples can not serve as an effective channel for non-radiative recombination, but rather might be the levels responsible for D1 luminescence.

With the increasing of the twist angle to 6° and further to 30°, defects having deep levels become dominating in DLTS-spectra and that is accompanied with the drastic reduction of DRL D1 peak. The reduction of D1 is not related to increase of the non-radiative recombination, since the enhancement of BB luminescence was observed in these samples, see Fig. 1 and [7]. On the other hand, the density of the edge dislocations is practically the same in all our samples (see Table 1), thus redistribution of DRL could not be the reason as well. Therefore, the possible reason of the changes in the trap level content and of the disappearance of DRL should be a destruction of specific structures in the core of screw dislocations that give rise to D1 DRL. As a further confirmation of cardinal changes in the DN structure with increase in the twist angle could be the correspondence of the energy distribution of hole trap states observed in L4 sample with that known for large angle grain boundaries [12]. Similar distribution was attributed in [12] to defects possessing deep levels in the bandgap, formed or segregated due to the large lattice mismatch.

References

[1] M. Kittler, X. Yu, T. Mchedlidze, T. Arguirov, O. Vyvenko and W. Seifert, M. Reiche, T. Wilhelm, M. Seibt, O. Voss, W. Fritzsche, A. Wolff, Small, Vol. 3 (2007), p. 964.

[2] W. Schröter, H. Hedemann, V. Kveder and F. Riedel, J. Phys.: Condens. Matter, Vol. 14 (2002), p. 13047.

[3] O. Kononchuk, F. Boedt and F. Allibert, Sol. St. Phenom., Vol. 131-133 (2008), p.113.

[4] M. Reiche, Mat. Sci. Forum, Vol. 590 (2008), p.57.

[5] T. Wilhelm, T. Mchedlidze, X. Yu, T. Arguirov, M. Kittler and M. Reiche, Sol. St. Phenom., Vol. 131-133 (2008), p. 571.

[6] S. Weiss and R. Kassing, Solid-State Electronics, Vol. 31 (1988), p. 1733.

[7] T. Mchedlidze, O. Kononchuk, T. Arguirov, M. Trushin, M. Reiche and M. Kittler, proceedings of this conference, GADEST 2009.

[8] P. Blood and J. W. Orton, *The electrical characterization of semiconductors: majority carriers and electron states*. 1992, London: Academic Press.

[9] P.A. Martin, B.G. Streetman, K.Hess, J. Appl. Phys., Vol. 52 (1981), p. 7409.

[10] J.-L. Farvacque and P. Francois, Phys. Stat. Sol. (b), Vol. 223 (2001), p. 635.

[11] A. Castaldini, D. Cavalcoli, A.Cavallini, S. Pizzini, Phys. Rev. Lett., Vol. 95 (2005), p. 076401.

[12] G. C. McGonigal, D. J. Thomson, J. G. Shaw and H. C. Card, Phys. Rev. B, Vol. 28 (1983), p. 5908.

PII

GIANT POOLE-FRENKEL EFFECT FOR THE SHALLOW DISLOCATION-RELATED HOLE TRAPES IN SILICON

M. Trushin, O. Vyvenko, V. Vdovin, and M. Kittler.

Published in: *Journal of Physics: Conference Series 281, p. 012009, 2011*.

Journal of Physics: Conference Series **281** (2011) 012009 doi:10.1088/1742-6596/281/1/012009

Giant Poole-Frenkel effect for the shallow dislocation-related hole traps in silicon

M Trushin[1], O Vyvenko[2], V Vdovin[2] and M Kittler[1,3]
[1] Joint Lab IHP/BTU, Konrad-Wachsmann-Allee 1, 03046 Cottbus, Germany
[2] V.A. Fok Institute of Physics, St. Petersburg State University, Ulyanovskaya 1, 198504 St. Petersburg, Russia
[3] IHP microelectronics, Im Technologiepark 25, 15236 Frankfurt (Oder), Germany

E-mail: vyvenko@gmail.com

Abstract. The results of a theoretical calculation of the Pool-Frenkel effect due to the strain field of screw and 60º dislocations upon the valence band in silicon, and of a detailed DLTS study of the electrical field impact on carrier emission from the dislocation-related states of two types of bonded samples are presented and discussed. A good agreement between the theory and experiment was established. It is concluded that the large Pool-Frenkel coefficient value that significantly exceeds the value for a Coulomb-like potential is a new distinguishing feature of the hole thermo-emission from dislocation-related levels in silicon.

1. Introduction

During the last few decades, dislocation-related electronic states in the band gap of silicon were intensively studied by means of deep level transient spectroscopy (DLTS) and numerous data were collected (for review see [1]). The main well-known features of the dislocation-related DLTS-signal are the broadening of the DLTS peaks and the logarithmic dependence of their magnitude on the refilling pulse duration. Very recently it was reported [2] that the main hole traps in p-type silicon with a dislocation network (DN) exhibited a strong field-enhanced thermal emission. A linear dependence of the activation energies for the hole emission on the square root of the electric field (the Pool-Frenkel effect) was established. In addition, the Pool-Frenkel coefficient value was found to be different in samples with different dislocation structures, and to exceed the theoretical value for the Coulomb potential. That led to the assumption [2] of a dislocation-strain-related origin of the phenomenon observed.

In this work we performed theoretical calculations of the Pool-Frenkel effect due to the strain field of screw and 60º dislocations for the valence band in silicon, and more detailed experimental investigations of the impact of the electrical field on the carrier emission from the dislocation-related states of similar types of samples produced by silicon direct wafer bonding by means of diverse techniques of capacitance-transient analysis and of transmission electron microscopy (TEM). A good agreement between the theory and experiment was established. From this fact we conclude that giant Pool-Frenkel coefficient value is a new distinguishing feature of 60º dislocations in silicon.

2. Theory of Pool-Frenkel effect due to elastic strains of dislocations

2.1. Isolated dislocations

The Pool-Frenkel effect is a lowering of the potential barrier for carrier thermoemission from a deep level as the result of the composition of its attractive, Coulomb-like potential that is inversely proportional to the distance, r, and of the potential of a uniform electrical field, F (see figure 1).

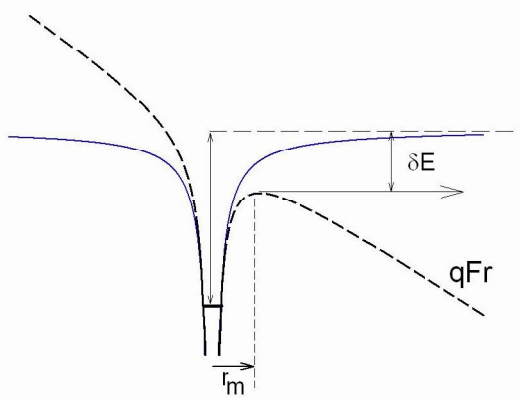

Figure 1. Coulomb attractive potential (solid line) and its changes in the presence of a uniform electric field (dashed line).

The resulting potential is three dimensional (3D) and depends on the angle θ between F and r as:

$$V(r) = -q(\frac{A}{r} + Fr\cos\theta) \tag{1}$$

It exhibits a maximum at the distance (see figure 1):

$$r_m = \sqrt{\frac{A}{F\cos\theta}} = \frac{\beta}{2\sqrt{F}}, \tag{2}$$

giving rise to the reduction of the emission activation energy by

$$\delta E_T = -q\beta\sqrt{F} \tag{3}$$

where

$$\beta = 2\sqrt{A\cos\theta} \tag{4}$$

is the Pool-Frenkel constant and q is the elemental charge.

For a Coulomb potential $A=q/4\pi\varepsilon$ that gives the maximum β-value of $2.22\times10^{-4}V^{-1/2}cm^{1/2}$ for $\cos(\theta)=1$ corresponding to the one-dimensional (1D) case. The calculation of the field-enhanced emission in the 3D-case needs the integration over spatial angles [3] that can be performed analytically and gives rise to a lower β-value of about $2\times10^{-4}V^{-1/2}cm^{1/2}$.

The deformation potential of dislocations is also inversely proportional to the distance [4]. Thus, a qualitatively similar field effect on the thermal emission of the carriers from electronic states located close to the dislocation cores can be expected. In the following we perform calculations of the Pool-Frenkel effect for the hole emission from the dislocation-related level to the valance band (Γ-point) in silicon. For this zone point, the theory [5] predicts that both uniaxial and shear components of dislocation deformation tensor can contribute to the deformation potential.

The components of the deformation tensor are usually expressed in the dislocation coordinate system where x coincides with the dislocation line which is [110] for both screw and 60° dislocations

in silicon. Two other coordinates directions are arbitrary and we will take z to be along [001] and y to be along [1-10] directions.

In this coordinate system, the deformation tensor for screw dislocations consists of two non-diagonal components ε_{xy}, ε_{zx}:

$$\begin{aligned}\varepsilon_{xz} &= -\frac{B_x}{4\pi r}\sin\theta \\ \varepsilon_{xy} &= \frac{B_x}{4\pi r}\cos\theta\end{aligned} \tag{5}$$

For edge dislocations, the tensor consists of three components that also contain hydrostatic deformation ε:

$$\begin{aligned}\varepsilon_{yy} &= -\frac{B_y}{4\pi r(1-\nu)}\left(\cos\theta\left\{(1-2\nu)+2\sin^2\theta\right\}\right)+\frac{B_z}{4\pi r(1-\nu)}\left(\sin\theta\left\{(1-2\nu)-2\cos^2\theta\right\}\right) \\ \varepsilon_{zz} &= -\frac{B_y}{4\pi r(1-\nu)}\left(\cos\theta\left\{(1-2\nu)-2\sin^2\theta\right\}\right)+\frac{B_z}{4\pi r(1-\nu)}\left(\sin\theta\left\{(1-2\nu)+2\cos^2\theta\right\}\right) \\ \varepsilon_{zy} &= \frac{B_y}{4\pi r(1-\nu)}\left(\sin\theta\left\{1-2\cos^2\theta\right\}\right)-\frac{B_z}{4\pi r(1-\nu)}\left(\cos\theta\left\{1-2\sin^2\theta\right\}\right) \\ \varepsilon &= Sp(\varepsilon_{ii}) = \frac{(1-2\nu)}{2\pi r(1-\nu)}\left(B_z\sin\theta - B_y\cos\theta\right)\end{aligned} \tag{6}$$

where B_x, B_y and B_z are the projections of the Burgers vectors along corresponding directions, r is the distance from dislocation, the angle θ is counting out from z axis and ν is the Poisson ratio (ν=0.3 for Si).

The calculations of the dislocation deformation potential have to be performed in the natural crystal coordinate system that for cubic lattices is x'=[100], y'=[010], z'=[001] [5]. In this system the deformation tensor for the dislocation with an arbitrary Burgers vector can obtained by a 45° rotation of the dislocation coordinates around the z-axis and has the general form as follows:

$$\begin{pmatrix} \varepsilon_{yy}/2+\varepsilon_{xy} & \varepsilon_{yy}/2 & \frac{\sqrt{2}}{2}(\varepsilon_{zy}+\varepsilon_{zx}) \\ \varepsilon_{yy}/2 & \varepsilon_{yy}/2-\varepsilon_{xy} & \frac{\sqrt{2}}{2}(\varepsilon_{zy}-\varepsilon_{zx}) \\ \frac{\sqrt{2}}{2}(\varepsilon_{zy}+\varepsilon_{zx}) & \frac{\sqrt{2}}{2}(\varepsilon_{zy}-\varepsilon_{zx}) & \varepsilon_{zz} \end{pmatrix} \tag{7}$$

Following the deformation potential theory [5] the valence band in silicon at the Γ-point exhibits a shift due to the hydrostatic component, and a splitting into two sub-bands due to shear components of deformation tensor. Taking into account the explicit form of deformation tensor (7), the resulting deformation potential of the dislocation can be written as:

$$\begin{aligned}&V_{1,2} = aSp(\varepsilon_{ii})\pm \\ &\pm\left(\frac{b^2}{2}[(2\varepsilon_{xy})^2+(\varepsilon_{zz}-\frac{\varepsilon_{yy}}{2}+\varepsilon_{xy})^2+(\varepsilon_{zz}-\frac{\varepsilon_{yy}}{2}-\varepsilon_{xy})^2]+\frac{d^2}{2}((\varepsilon_{zy}+\varepsilon_{zx})^2+(\varepsilon_{zy}-\varepsilon_{zx})^2+\frac{\varepsilon_{yy}^2}{2})\right)^{1/2}\end{aligned} \tag{8}$$

where numerical values of the deformation potential constants for the valence band in silicon are a=5.1eV, b=2.2eV and d=5.1eV.

Using equation (8) together with the explicit form of the deformation components (5) and (6), we calculated the parameters $A=Vr/qB$ and β that quantify the Pool-Frenkel effect. In the calculations the electrical field was directed along z. For a pure screw dislocations we took $B_x = B = 0.384$ nm. For the 60° dislocation, $B_x = B/2$, $B_z = 0.707B$, whereas B_y was either $+B/2$ or $-B/2$ corresponding to those two possible orientations of the 60° dislocation with respect to the (001) plane marked as b1 and b2 in figure 2A, respectively.

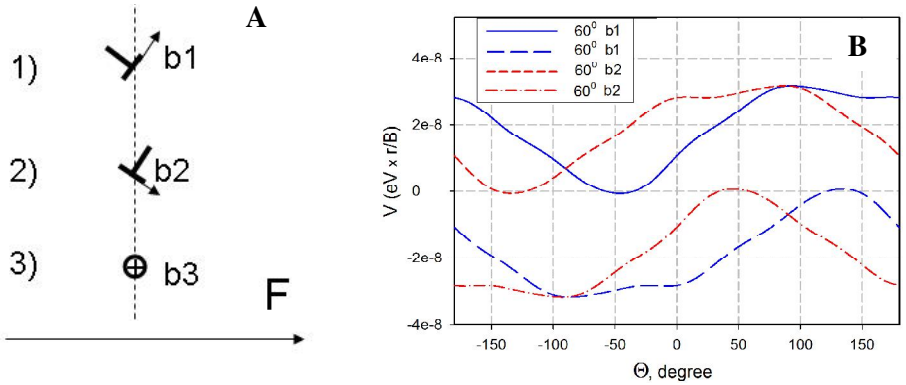

Figure 2. (A) Orientations of 60° (b1, b2) and screw (b3) dislocations in the projection on (110) plane. Dashed line shows the projection of the (001) plane with the dislocation network. Electric field F is directed to [001]. (B) shows the theoretical angle dependence of deformation potential (A-factor) for 60° dislocations with the orientations b1 and b2 shown in figure 1A. The angle is counted from the direction [001] that coincides with the direction of electric field.

Figure 2B represents the angle dependences of A-factor for 60° dislocations with two possible orientations in the DN plane depicted in figure 2A. The main features of the dependences are: 1) significant splitting of the valence band around the dislocations caused by shear deformations; 2) the lower sub-band forms an attractive potential for most directions that can cause a Pool-Frenkel effect; 3) the shapes of the corresponding potential for the two dislocation orientations are close to each other but shifted by the angle of about 70°.

Figure 3A shows $\beta(\theta)$ calculated for the lower valence band V_2 at the screw, at both types of 60° dislocations as well as for a 3D Coulomb potential. One can note that the $\beta(\theta)$ for screw dislocation is rather similar to the one for the Coulomb potential, while for 60° dislocations it has a larger maximum value especially for the b1 orientation.

The calculation of the field enhanced emission rate for dislocations was performed making use the integration according to:

$$\frac{e_p(F)}{e_{p0}} = \frac{1}{2\pi}\left(\alpha \int_{-\pi/2}^{\pi/2} d\theta \exp[\frac{\delta E_t(\theta)}{kT}] + 1 - \alpha\right) \qquad (9)$$

where α is the ratio of the angles where enhanced emission takes place (α is 0.5 for screw and 60° dislocation b1, but is 0.325 for 60° dislocation b2).

The results of numerical integration of equation (9) for all dislocations as well as the previously reported [3] expression for the 3D Coulomb are presented in figure 3B. At sufficiently high electric fields, all of the curves can be well fitted with the Pool-Frenkel law: $e_p(F)/e_{p0} = \exp(\beta_{\text{eff}}\sqrt{F})$. The curves for the Coulomb potential and for the screw dislocation deformation potential for the valence band coincide practically with each other giving $\beta_{\text{eff}} \approx 2\times10^{-4}\text{V}^{1/2}\text{cm}^{-1/2}$. The values for 60° dislocations are $\beta_{\text{eff}}(\text{b1}) \approx 3.2\times10^{-4}\text{V}^{1/2}\text{cm}^{-1/2}$ and $\beta_{\text{eff}}(\text{b2}) \approx 2.4\times10^{-4}\text{V}^{1/2}\text{cm}^{-1/2}$.

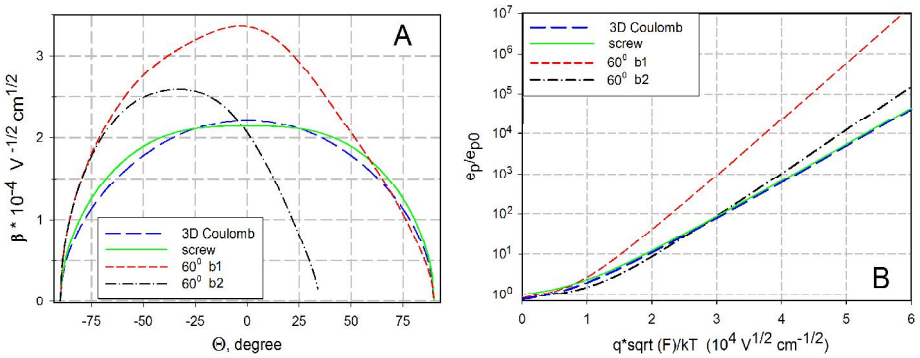

Figure 3. Angle dependence of Pool-Frenkel coefficient (A) and relative enhancement of the hole thermoemission under applied electric field (B) for 3D Coulomb (blue dashed line) and for deformation potential of screw (green solid line), 60 º dislocation with two orientations depicted in figure 2A: b1 –red short-dashed line, b2- black dashed-dotted line).

2.2. Dislocation network

For the samples under investigation, the interaction of the elastic strains between the dislocations in a network must be taken into consideration that generally results in strain field localization.

Detailed examination of the contribution of different components of deformation tensor to the Pool-Frenkel constant for screw dislocations showed that the most important component is ε_{xy}. Using the explicit expression for the elastic strains of a dislocation row given in [4], we plotted the dependence for this component as a function of the reciprocal distance from the plane of dislocation row (figure 4A) and DN (figure 4B) and compared them with that for the isolated dislocation. The results are presented in figure 4C.

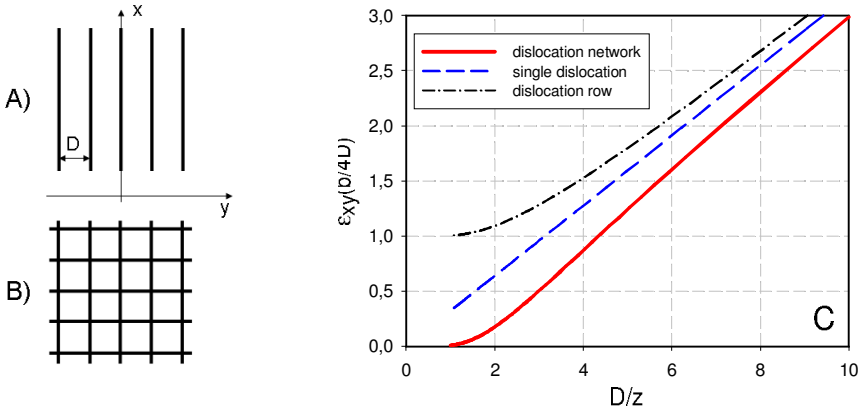

Figure 4. (A) Dislocation row and (B) square dislocation network. (C) shows the deformation of isolated dislocation (long dashed), dislocations in a row A (dashed-dot) and in a square network B (solid). For the DN, the *z*-coordinate goes through the centre of dislocation segments between the nodes.

One can see that the significant difference of the strains ε_{xy} from $1/r$ law starts at the distances larger than z_{crit} being of about $D/5$ and $D/2$ for dislocation row and for DN respectively. Obviously, the Pool-Frenkel law can be observed under application of the electric field above the value F_{min} that corresponds to Pool-Frenkel radius (r_m , equation 2) of about z_{crit}.

The latter value allows one to estimate F_{min} as a function of D by using relation:

$$F_{\min} > \left(\frac{\beta}{2 z_{crit}} \right)^2 \tag{10}$$

or estimate D_{min} for the given electric field ranges:

$$D_{\min} > (2 \div 5) \frac{\beta}{2\sqrt{F}} \tag{11}$$

where the numbers 2 or 5 relate to DN or to the row, respectively. By using these expressions [4], it can be shown that similar estimates are valid for the row of edge type dislocations as well.

3. Samples and experimental technique

Samples were fabricated by direct bonding of 200 mm, p-type Si wafers with (001) surface orientations in a hydrophilic process, i.e. the surfaces of the wafers were covered with native oxide layer before the bonding process [6]. The doping level of the wafers was ~10^{15} atoms/cm^3 of boron. A detailed description of the bonding procedure can be found elsewhere [6],[7]. After the bonding and a thinning procedure of the top layer, a dislocation network was located at the depth of 160 nm from the sample surface. In order to dissolve the interfacial native oxide layer, samples were annealed at 1200°C in high purity conditions [6]. After the annealing neither secondary ion mass spectrometry nor TEM investigations revealed any variations of oxygen concentration near to the bonding interface. Wafers were bonded with two different twist angles of about 1 and 3 ° and are denoted as Gr-1 and Gr-3 respectively. Both samples have the same small tilt angle of about 0.5° that was a result of wafer polishing.

To produce Schottky contacts for DLTS measurements, 100 nm-thick titanium dots with 1.5 mm diameter were evaporated on the oxide free front surface of all samples. Ohmic contacts were prepared by rubbing of InGa on the rear side of the samples. DLTS measurements were performed by means of transient Fourier spectroscopy system DL-8000 (Accent).

4. Experimental results

DLTS spectra of both samples investigated possess similar features: the main, low-temperature peak (labelled as ST1 in Gr-1 and as ST3 in Gr-3) dominates the spectrum and a set of strongly overlapped DLTS peaks appear at temperatures of 100-250K (for details see [2]). It was also found, that the temperature positions of the ST1 and ST3 peaks were shifted toward lower temperatures with the increase of applied reverse bias, i.e. with the increase of the electric field in the depletion region, as shown in figure 5. Note that the sets of DLTS spectra for Gr-1 and Gr-3 samples presented in figures 5A and 5B were measured with the same refilling pulse voltage, U_p= -1V.

Detailed analysis of the shape of the ST1 and ST3 DLTS peaks revealed that their shapes differed from expected for point-like defects. The broadening of DLTS peaks can generally affect the precision of the E_a definition and can be caused either by the widening of the electronic spectrum or by spatial or transient variation of the electric field. That is why we performed another type of the experiment to evaluate the Pool-Frenkel coefficient value, that is isothermal relaxation Spectroscopy (ITS).

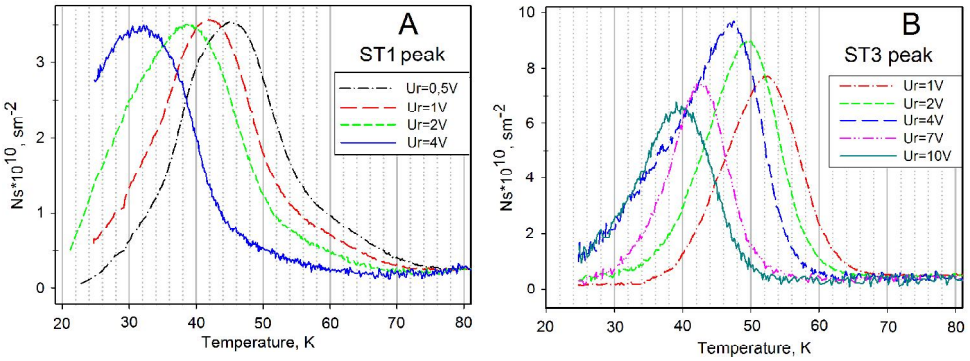

Figure 5. The low temperature part of the DLTS spectra of Gr-1 (5A, left) and Gr-3 (5B, right) samples, measured with different reverse bias voltages. DLTS-scan parameters: filling pulse duration t_p=100μs, filling pulse voltage U_p= –1V, and rate window T_w=20ms. Reverse bias voltages, U_r, are shown in the legends.

ITS measurements were performed at constant temperature under the gradually increasing rate window period using the same correlation procedure as DLTS. Since the response of the DLTS correlator is a function of the product of the emission rate, e_p, and the correlator period, τ, the dependence of τ on the electrical field obtained at a specific level of ITS signal (i.e. keeping the product $e_p\tau$ = constant) will be inversely proportional to the dependence on e_p. Thus, when the broadening of a DLTS line is caused by a widening of the electronic spectrum, the dependence of $\ln(e_p)$ on the square root of electric field must have the same slope, β, for all the ITS signal level. Alternatively, when the broadening is caused by electric field variations β might vary dependent on the ITS signal level.

Examples of ITS spectra of the Gr-1 and Gr-3 samples measured with different reverse bias voltages, U_r, and the same filling pulse voltage U_p =-1V are presented in figure 6. Measurement temperatures were chosen to be 40K for Gr-1 sample and to be 53K for Gr-3 sample that allowed one to use the largest interval U_r voltages for the ITS spectra acquisition inside the usable rate window ranges of our transient recorder.

The electric field at the position of the DN (d = 160nm below the front sample surface) for every reverse bias voltage was calculated using the standard relation $F = qN_a(w-d)/\varepsilon$, where N_a is the net acceptor concentration, and w is the SCR-width calculated from capacitance data at the DLTS/ITS measurement temperature. Generally, the charge contained within DN states should be taken into account for the electric field calculations as well. Unfortunately, the ground charge state of the detected traps is not known precisely. Nevertheless, we believe the charge collected at the DN will not significantly modify the results of the field definition since the total charge of the doping impurity inside the space charge region, eN_aw, is much larger than the total concentration of all traps detected by DLTS, i.e. $eN_aw > e\sum N_{DLTS}$ for all used U_r voltages.

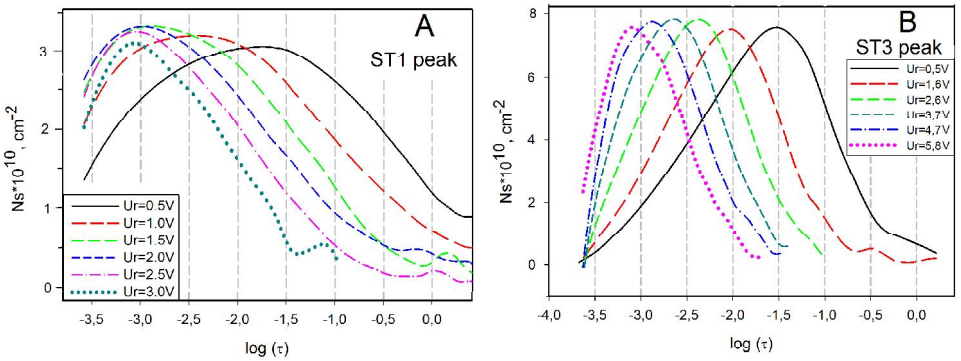

Figure 6. Sets of ITS spectra of (A) sample Gr-1 and (B) sample Gr-3, measured with different reverse bias voltages. Ordinate axes show the surface trap density, abscissa axes – the natural logarithm of the emission time constant τ. ITS-scan parameters: measurement temperatures are 40K for Gr-1 sample and 53K for Gr-3 sample, filling pulse duration t_p=100μs, and filling pulse voltage U_p= –1V. Reverse bias voltages, U_r, are shown in the legends.

Using the values of the electric field calculated in such a way, dependences of activation enthalpies E_a derived from the DLTS spectra, and $kT\ln(e_p)$ derived from the ITS measurements based upon the square root of electrical field $\sqrt{F}$ were plotted, as shown in figures 7A and 7B, respectively. One can see that all the dependences obtained for both ST1 and ST3 peaks could be well approximated by a straight line, and thus follow the Poole-Frenkel law.

The slopes of the linear dependences obtained, which correspond to Poole-Frenkel coefficients β, as well as the activation enthalpies, E_{a0}, at zero electric field approximated from DLTS data (figure 7A), are summarized in table 1. It should be noted also that β-values obtained from the ITS-data at different signal levels coincided within the measurement errors, indicating that the broadening of the DLTS spectra arises from the broadened spectra of the electronic states.

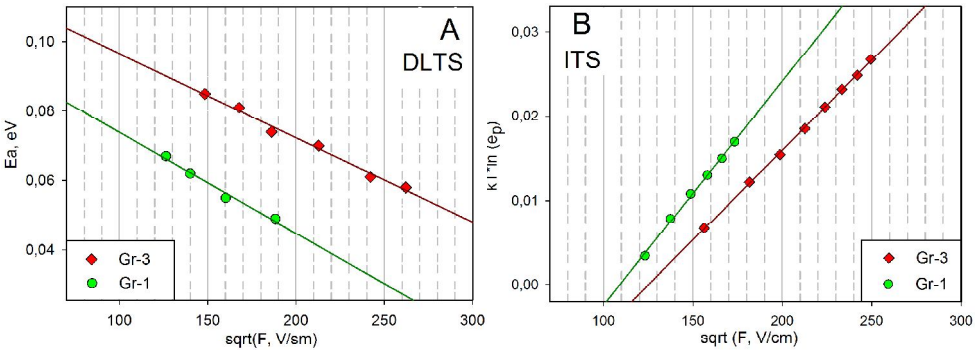

Figure 7. Dependences of the activation enthalpies, E_a, derived from (A) DLTS, and (B) the kT-corrected logarithm of emission rates derived from ITS dependence on the square root of electric field for the ST1 and ST3 peaks in Gr-1 and Gr-3 samples. Symbols show experimentally obtained values, and straight lines linear approximations.

The β–values are noticeably larger than those expected for a 3D Coulomb potential, especially for sample Gr-1. The values obtained from the DLTS measurements are slightly bigger than those from the ITS-data. The reason of this discrepancy is not known precisely and might be caused by a systematic error in temperature measurements affecting mostly the determination of the activation energies E_a from Arrhenius plots. The difference between the zero-field activation enthalpy, E_{a0}, for the ST1 trap level and that for the ST3 level at about 15 meV is close to the their definition error.

Table 1. Poole-Frenkel coefficient β and activation enthalpies E_{a0} at zero electric field for ST1 and ST3 peaks as derived from ITS and DLTS measurements.

		Gr-1 sample ST1 peak	Gr-3 sample ST3 peak
ITS	β, (10^{-4} cm$^{1/2}$V$^{-1/2}$)	2.8	2.1
DLTS	β, (10^{-4} cm$^{1/2}$V$^{-1/2}$)	3.0	2.4
	E_{a0}, (eV)	0.105	0.12

5. Discussion

Our theoretical calculations presented in section 2 showed that the β–coefficient value of the dislocation-related Pool-Frenkel effect depends strongly on the type, on the orientation and on the density of dislocations. Figure 8 shows TEM micrographs of the dislocation structure of the DN of both samples investigated.

Detailed analysis of the structure showed that most of the dislocations in sample Gr-1 (figure 8A) seemed to be 60^o dislocations, though the exact direction of Burgers vector could not be defined precisely from TEM data. The structure in figure 8A looks like a row of parallel dislocations separated by distances of about 60 nm rather than a square DN.

The electric field values used in the experiment with this sample started from 14 kV/cm. The minimal distance when the theory of isolated dislocation is still valid can be estimated according to equation (10) for that field is of about 40 nm. Thus, the theoretical conditions are satisfied and the predicted Pool-Frenkel coefficient value is expected to be about 3×10^{-4}V$^{1/2}$cm$^{-1/2}$ for the case of the most favourable orientation b1 of 60^0 dislocations in the DN shown in figure 2. This is in good agreement with the β–value for this sample (see table 1).

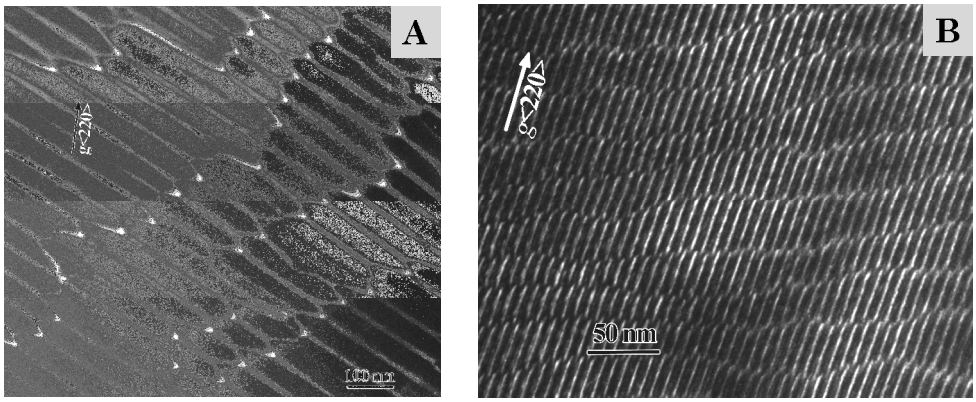

Figure 8. Dark field TEM images of the samples under investigation. (A) sample Gr-1 and (B) sample Gr-3.

The dislocation structure of sample Gr-3 consists of square mesh of perfectly straight screw dislocations (only one set of them is visible in figure 8B due to particular diffraction conditions) and the rows of curved 60° dislocations that are inclined to the screw dislocation lines on average at an angle of about 30°. The inter-dislocation distances for screw dislocations are of about 7 nm, while for the 60° dislocations they are varying from 30 to 50 nm. For the electric field ranges used in the experiments (see figure 7) the Pool-Frenkel radius is estimated to be of 8-14 nm for the mesh and 20-33 nm for the row. Hence, the validity of the theory for isolated dislocation is satisfied for 60° dislocations but not for screw dislocations. Thus, the screw dislocations have to be ruled out of the consideration as a possible origin for the observed Pool-Frenkel effect. The Pool-Frenkel coefficient value obtained from experiment $\beta \approx (2.1—2.4) \times 10^{-4} V^{1/2} cm^{-1/2}$ corresponds to the theoretically predicted value for 60° dislocation in the orientation b2 in figure 2.

The difference between the experimental β-value for the Gr-1 and Gr-3 samples can be then explained due to different crystallographic orientations of the handle and the top bonded wafers. The predominant 60° dislocation orientations b1 or b2 in figure 2 could be realized due to an asymmetry of the tilt misorientation between the handle and the top wafers, for example, when the handle wafer has exact (100) orientation and the tilt between the wafers is due to misorientaion of the top wafer only or vice versa. Since the tilt between the bonded wafers was not controlled during the bonding process and arose as the result of wafers polishing such an explanation seems to be reasonable. Nevertheless, one can not exclude that the lower β in the Gr-3 sample was due to the interaction of 60° dislocations with screw dislocations giving rise to a zigzag configuration of resulting dislocations [8]. Such a configuration, obviously, could have the strain field that differs significantly from that of a straight dislocation.

6. Conclusion

In conclusion we have demonstrated both theoretically and experimentally a new dislocation-related phenomenon that is the Pool-Frenkel effect caused be elastic strains of dislocations in silicon. We showed that Pool-Frenkel coefficient can reach the value that significantly exceeds the value for a Coulomb-like potential of a singly charged point defect. The presence of dislocations with different Burgers vectors and different orientations with respect to the electric field can cause a drastic broadening of DLTS-peaks.

Acknowledgements

The authors are grateful for helpful discussion to T. Mchedlidze and to O. Kononchuk.

References

[1] Schroeter W and Cerva H 2002 *Solid State Phenom.* **85-86** 67
[2] Trushin M, Vyvenko O, Mchedlidze T, Kononchuk O and Kittler M 2010 *Sol. St. Phenom.* **156-158** 283
[3] Hartke J L 1968 *J. Appl. Phys.* **39** 4871
[4] Hirth J P and Lothe J 1970 *Theory of dislocation*. (New York: McGraw-Hill)
[5] Bir G L and Pikus G E 1974 *Symmetry and deformation effects in semiconductors*. (Wiley, New York)
[6] Kononchuk O, Boedt F, and Allibert F 2008 *Sol. St. Phenom*. **131-133** 113
[7] Reiche M 2008 *Mater. Sci. Forum* **590** 57
[8] Föll H and Ast D 1979 *Philos. Mag. A* **40** 589

PIII

ENERGETIC SPECTRA OF DISLOCATION NETWORKS PRODUCED BY HYDROPHILIC BONDING OF SILICON WAFERS

I. Kolevatov, M. Trushin, O. Vyvenko, M. Kittler, O. Kononchuk.

Published in: *Physica Status Solidi C 10, p. 20, 2013*.

Phys. Status Solidi C **10**, No. 1, 20–23 (2013) / **DOI** 10.1002/pssc.201200396

physica status solidi c
www.pss-c.com
current topics in solid state physics

Energetic spectra of dislocation networks produced by hydrophilic bonding of silicon wafers

I. Kolevatov[*,1], **M. Trushin**[**,2], **O. Vyvenko**[1], **M. Kittler**[2], **and O. Kononchuk**[3]

[1] V.A. Fok Institute of Physics, St. Petersburg State University, Ulyanovskaya 1, 198504 St. Petersburg, Russia
[2] Joint Lab IHP/BTU, Konrad-Wachsmann-Allee 1, 03046 Cottbus, Germany
[3] SOITEC, Parc Technologique des Fontaines, 38560 Bernin, France

Received 20 June 2012, revised 13 August 2012, accepted 21 September 2012
Published online 3 December 2012

Keywords dislocation network, band-like states, DLTS, admittance spectroscopy

* Corresponding author: e-mail ilya.kolevatov@gmail.com, Phone: +78124284396, Fax: +78124284478
** e-mail trushmax@tu-cottbus.de, Phone: +49 355 69 3904, Fax: +49 355 69 4961

Electronic states of dislocation networks produced by Si wafers bonding was studied by means of deep level transient and admittance spectroscopy methods. A strong field-enhanced hole thermoemission was established for one shallow and one deep states in p-type Si that was explained in the framework of dislocation-related Poole-Frenkel-effect model. The shallow dislocation related states situated close to the valence as well as to the conduction band of silicon were found to be associated with the broad energetic bands with rapid interstate exchange.

1 Introduction Recently it was demonstrated [1-3] that for the goal of the investigation of electrical and optical properties of dislocations in semiconductors the samples containing dislocation network (DN) produced by wafer bonding [4] have special advantages over the samples containing randomly distributed dislocations introduced by plastic deformation: (i) DN is going strictly parallel to the front surface and could be placed at the desired depth suitable for the capacitance spectroscopy's methods, (ii) the density and types of dislocations composing the DN could be controlled by tilt and twist misorientation angles between the bonded wafers, (iii) the absence of the defects accompanied the dislocation motion during plastic deformation [6].

Recently, extensive studies of the dislocation-related states and optical spectra were performed on silicon bonded wafers [1-3 ,5 ,7]. Among other new data a strong field enhanced hole thermoemission was found for the shallow dislocation-related traps in p-type bonded samples that was attributed to Poole-Frenkel effect (PFE) due to the strain fields of 60° dislocations [5]. Besides, a new technique to establish the energy position of electrical level responsible for dislocation-related luminescence (DRL) was developed and the participation of the shallow states in D1 DRL was confirmed [7].

In this paper we report the results of a more detailed investigation of deep and shallow DN-related levels on a new set of bonded samples of both n- and p-type conductivity with the DN structure optimized for the highest D1 DRL efficiency. Since the presence of PFE in p-type samples hindered to obtain the reliable information about the entire spectrum of electronic states from deep-level transient spectroscopy (DLTS) and Isothermal relaxation Spectroscopy (ITS) data, an additional technique – admittance spectroscopy (AS) – was applied to measure directly the energy distribution of density of states (DOS) at nearly zero external field.

2 Experimental results

The samples were silicon hydrophilically bonded wafers of p-type doped to 10^{15} cm^{-3} with boron and of n-type doped to 10^{14} cm^{-3} with phosphorus. Details on the bonding procedure can be found elsewhere [4]. The thickness of the top layer was about 180 nm. Au for n-type and Ti for p-type were used as Schottky and Ga-Al eutectic was used as ohmic contacts.

2.1 Dislocation-related Poole-Frenkel effect

Figure 1 represents the set of DLTS spectra recorded on p-type bonded sample with different reverse bias voltages and a forward filling pulse voltage of -1 V. Forward-biased filling pulses were needed to refill the DN-related states since DN in the investigated samples was located close to the front surface. One may notice that the temperature positions of ST and SD peaks (but not of HL one) are shifting towards the lower temperatures with the increase of the applied reverse bias U_r, i.e. with the increase of the external electric field in the depletion region of Schottky diode. For the low-temperature peak ST such phenomenon was observed before on similar bonded samples and ascribed to the so-called dislocation-related Poole-Frenkel effect (PFE) [3, 5].

Classical Poole-Frenkel effect is a lowering of the potential barrier for the carrier thermoemission from a deep level as the result of the composition of its attractive, Coulomb-like potential and of the potential of uniform electric field F. In this case the theory gives a linear dependence of activation enthalpy (or of logarithm of emission rate) on the square root of electric field [8]. Dislocation-related PFE suggests a qualitatively similar influence of electric field on the carrier thermoemission from the defect states located inside or close to the dislocation core in the regions of high elastic strain field [5].

Figure 2 shows the dependences of the logarithm of emission rates for ST and SD traps as obtained from ITS measurements on the square root of electric field. In agreement with Poole-Frenkel law, both dependences could be well approximated by a straight line with nearly identical coefficients β_{ST} =2.4 and β_{SD} =2.2 in 10^{-4} $cm^{1/2}$ $V^{-1/2}$ units. These coefficients are noticeably larger than β_C predicted for Coulomb-like potential [8] but are in a good agreement with the value β_{60} =2.4 calculated theoretically for 60° dislocations [5]. Moreover, donor-like origin of these defects [3] implies the absence of Coulomb potential, i.e. the absence of the classical Poole-Frenkel effect.

Repeated observation of PFE on the shallow ST level on various bonded samples as well as our new result of the observation of this effect on the deep SD level and similar β-values confirm the validity of the proposed model [5]. An obvious conclusion from the above discussed statements is that both shallow ST and deep SD levels are directly related to 60° dislocations whereas the deepest level HL, which does not reveal any field-enhanced emission, should be attributed to the defects located somewhere far from the 60° dislocation cores.

When applying refilling forward voltage pulses larger than -1 V an additional shallow level (labelled as SN level) was found to appear as a shoulder on the low-temperature side of the dominant ST peak, see Fig. 3. By measuring the dependence of DLTS spectra on the reverse bias voltage with filling pulse voltage of U_p=-1.5 V, it was ascertained that only ST peak is moving towards the lower temperature with the increase of the electric field, whereas SN peak remains at the same temperature position, leading to the broadening of the resulting DLTS peak at its low-temperature side.

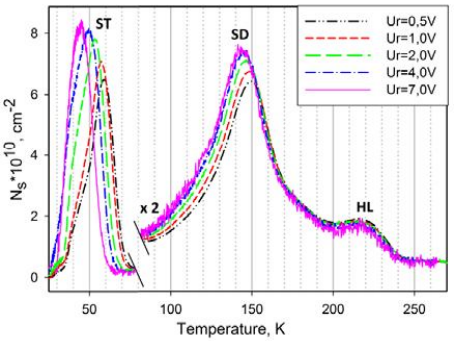

Figure 1 Set of DLTS spectra of p-type bonded sample measured with different reverse bias voltages U_r shown in the legend. The surface trap density was calculated according to [3]. DLTS-scan parameters: filling pulse duration t_p=1 ms, filling pulse voltage U_p= –1 V, rate window 20 ms. Magnitude of DLTS signal for T > 80 K was multiplied by a factor of 2 for better representation.

Since no PFE was revealed for SN traps, we conclude that the structural element responsible for SN peak is not related to 60° dislocations. One may tentatively ascribe this level to the dense array of screw dislocations which, as it was shown in [5], does not exhibit PFE due to mutual compensation of strain fields of individual dislocations.

In concordance with previous results [2] no PFE was observed for n-type bonded samples despite the theory predicts similar effect for 60°-dislocation-related states in the upper half of band gap as well. It is not clear at the moment whether the absence of PFE is due to the lower

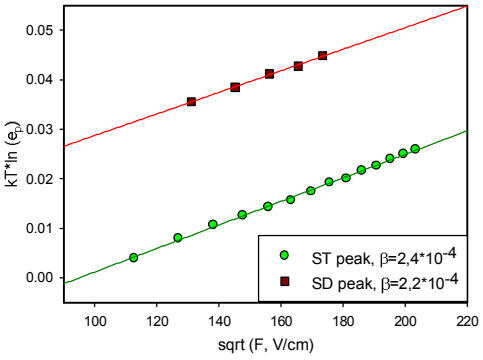

Figure 2 kT-corrected logarithms of emission rates e_p as the function of the square root of electric field for the DLTS peaks denoted as ST and SD in Fig. 1. The symbols correspond to experimental data obtained from the position of the ITS peaks, the lines represent the best linear data fits.

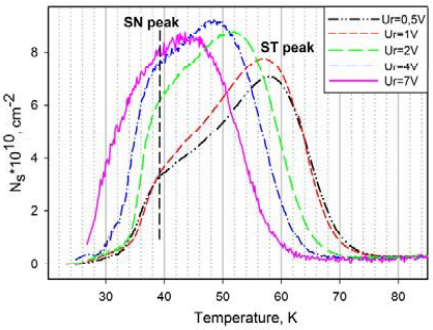

Figure 3 The low-temperature part of DLTS spectra measured at reverse bias voltages U_r shown in the legend. The filling pulse voltage was U_p = -1.5 V. Refilling pulse duration t_p = 1 ms, rate window T_w = 20 ms. The vertical dashed line shows the approximate temperature position of SN peak.

doping level and, accordingly, lower electric field that was not sufficient to register PFE, or the states in the upper half of band gap are not related to the cores of 60° dislocations.

2.2 Band-like structure of ST DLTS-peak According to [9] electronic states of extended defects can be classified either as "band-like" or as "localized-like" depending on the DLTS-peak shape behaviour upon increasing of their occupancy degree. For the defects uniformly distributed in the bulk the latter can be varied by the duration of the filling pulse t_p. The filling grade of the DN-related interfacial states is defined by relative position of the particular energetic level with respect to the Fermi level in the bulk material and can be controlled by variation of the magnitude of the refilling pulse voltage U_p.

Figure 4 represents the dependences of low-temperature DLTS peaks in p-type (upper plot) and in n-type (lower plot) bonded samples as a function of the magnitude of filling pulse voltage U_p. One can see that with the increase of filling pulse magnitude along with the increase of the height of DLTS peaks their positions shift towards the lower temperatures whereas the high-temperature tails of the peaks almost coincide. Such a behavior was reported previously [9] for nickel silicide precipitates and was attributed to "band-like states", i.e. to a band of electronic state with a rapid interstate exchange.

Though the energetic width of the band can't be retrieved from DLTS data immediately, we still made their rough estimation from the activation enthalpy of DLTS peaks derived from the Arrenius plot data. For p-type sample the activation enthalpy varied from 130 meV to 90 meV when the filling pulse magnitude changed from U_p = -0.2 V to U_p = -0.6 V, respectively. Thus, the width of the shallow DN-related band near the top of valence band can be estimated as about 40 meV.

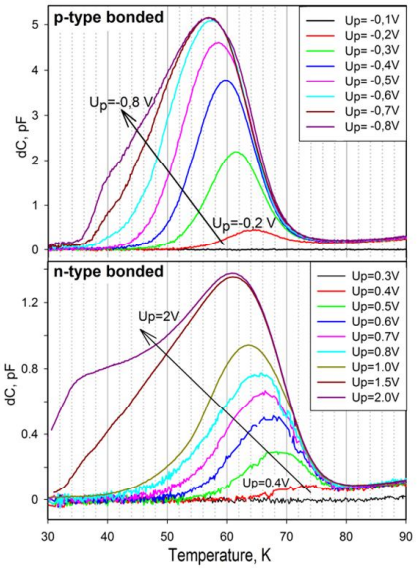

Figure 4 Low-temperature DLTS-peaks in p- and n-type bonded samples measured with different filling pulse voltages U_p shown in legends. Refilling pulse duration t_p = 1 ms, reverse bias U_r = 1 V (p-type) or -1 V (n-type), rate window T_w = 20 ms.

For n-type sample the activation enthalpy for U_p = 0.5 V was about 130 meV and about 80 meV for U_p = 1.5 V giving the estimation for the band width as close to 50 meV.

2.3 Energy distribution of DOS with AS Careful examination of DLTS spectra presented above shows that they exhibit a sharp turn at 35-40 K that is due to free carrier freezing. Besides, the retrieval of exact energy distribution of DOS from DLTS data is a tedious and ambiguous procedure [9]. In contrast to that AS is the technique that enables to get direct information about the energy distribution of DOS with the resolution of the order of kT. Moreover, AS registers the trap response at higher temperature than DLTS due to many orders of magnitude shorter rate windows allowing one to avoid the carrier freezing.

There are two approaches to retrieve DOS from immediate AS data developed for grain boundaries [10] and for the Schottky diode with a thin dielectric layer from the article [11]. The first one based on *ac* and *dc* conductance data. The second one uses a combination of capacitance and *ac* conductance data obtained at different frequencies of testing signal. Each of the models assumes the presence of the current over the potential barrier which is modulated by interface trap charge oscillating under the influence of an external testing *ac* voltage.

The energy position of the particular DOS with respect to the permitted band is determined in AS from the inter-

face barrier height values. That can be retrieved either from the current-voltage (IV) or from the capacitance-voltage (CV) data. A significant difference between barrier-voltage dependence obtained from IV and CV was found in our investigation. This disagreement might be caused by the electrical inhomogeneity of the grain boundary interface and we used the barrier values derived from IV-data at different temperatures.

The resulting spectra of shallow states near the edges of the permitted bands are shown in Fig. 5A for p-type and Fig. 5B for n-type samples, respectively. Both mentioned models gave coincident results. In p-type silicon DOS of DN increases smoothly from 200 meV towards the top of the valance band and at approximately 120 meV starts to go down. In n-type sample DOS exhibits more or less trapezium shape with a slow increasing top towards the conduction band bottom and a sharp drop to zero at about 75 meV. The lower edge of the band is close to but still above the Fermi level which is physical limit of AS measurements and which is shown as the dash-dotted line in Fig. 5B.

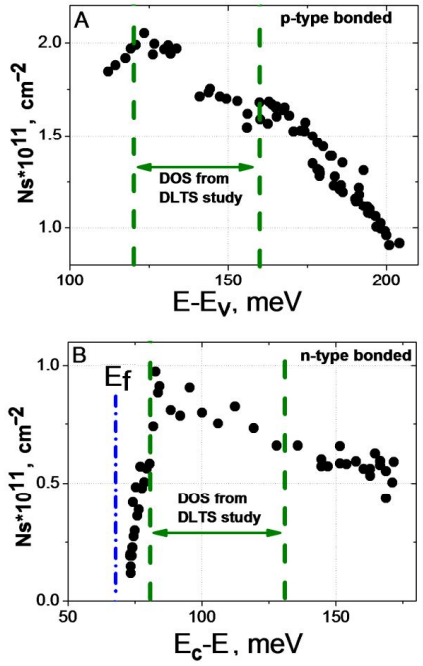

Figure 5 Density of shallow states in p- (A) and n-type (B) bonded samples retrieved from AS measurements. Green dashed lines reflect the band widths as obtained from DLTS data (for p-type sample with PFE the obtained activation enthalpy values were recalculated towards the zero electric field). Vertical dash-dotted line (B) depicts the position of Fermi level.

AS-width of both bands is not less than 100 meV for each type of silicon. One cannot exclude that in p-type it continued further towards the valence band. On the other hand, the width of the band from AS-data (that is significantly bigger than obtained from DLTS) might be overestimated due to non-homogeneity of the DN's potential barrier that was used to define the energy scale. Nevertheless, the result of AS confirms the presence of broad shallow dislocation-related bands in both p- and n-type silicon.

3 Conclusions The presence of dislocation-related PFE was confirmed on p-type samples for the shallow hole trap state ST and also found for the more deep SD level while two other levels SN and HL did not exhibit PFE. The presence or absence of PFE was used as a criterion to ascribe the levels to the states situated in the vicinity of the 60° dislocation cores or far from them.

The existence of shallow broad energy bands with rapid interstate exchange associated with DN was found near the edges of each permitted band. The position and the shape of DOS does not correspond to the theoretically calculated 1D dislocation states confined in the deformation potential of dislocations [6,12]. It might be a composition of 1D band and the deeper broad band related to unknown defects at dislocation cores.

Acknowledgements The authors acknowledge Saint-Petersburg State University for the research grant.

References

[1] M. Trushin, O. Vyvenko, T. Mchedlidze, O. Kononchuk, and M. Kittler, Solid State Phenom. **156-158**, 283 (2010).
[2] I. Isakov, A. Bondarenko, O. Vyvenko, V. Vdovin, E. Ubyivovk, and O. Kononchuk, J. Phys.: Conf. Ser. **281**, 012010 (2011).
[3] M. Trushin, Ph.D. thesis, Technische Universität Cottbus (2011); http://nbn-resolving.de/urn:nbn:de:kobv:co1-opus-22841.
[4] O. Kononchuk, F. Boedt, and F. Allibert, Solid State Phenom. **131-133**, 113 (2008).
[5] M. Trushin, O. Vyvenko, V. Vdovin, and M. Kittler, J. Phys.: Conf. Ser. **281**, 012009 (2011).
[6] V. Kveder and M. Kittler, Mater. Sci. Forum **590**, 29 (2008).
[7] A. Bondarenko, O. Vyvenko, I. Kolevatov, I. Isakov, and O. Kononchuk, Solid State Phenom. **178-179**, 233 (2011).
[8] J. Hartke, J. Appl. Phys. **39,** 4871 (1968).
[9] W. Schröter, J. Kronewitz, U. Gnauert, F. Riedel, and M. Seibt, Phys. Rev. B **52**, 13 726 (1995).
[10] J. Werner, K. Ploog, and H. Queisser, Phys. Rev. Lett. **57**, 1080 (1986).
[11] V.A. Stuchinsky and G.N. Kamaev, Semiconductors **34**, 1214 (2000).
[12] J.L. Farvacque and P. Francois, Phys. Status Solidi B **223**, 635 (2001).

PIV

IMPACT OF ELECTRIC FIELD ON THERMOEMISSION OF CARRIERS FROM SHALLOW DISLOCATION-RELATED ELECTRONIC STATES

M. Trushin, O. Vyvenko

Published in: *Solid State Phenomena 205-206, p. 299, 2014*.

Solid State Phenomena Vols. 205-206 (2014) pp 299-304
Online available since 2013/Oct/07 at www.scientific.net

doi:10.4028/www.scientific.net/SSP.205-206.299

Impact of Electric Field on Thermoemission of Carriers from Shallow Dislocation-Related Electronic States

M. Trushin[1,2,a], O. Vyvenko[1,b]

[1] V.A. Fok Institute of Physics, St. Petersburg State University, Ulyanovskaya 1, 198504, St. Petersburg, Russia

[2] Joint Lab IHP/BTU, Konrad-Wachsmann-Allee 1, 03046 Cottbus, Germany

[a]max_trushin@mail.ru, [b]vyvenko@gmail.com

Keywords: Dislocation networks, Poole-Frenkel effect, electronic states of dislocations, DLTS.

Abstract. Shallow dislocation-related electronic states near the bottom of the conduction band in n-type Si bonded sample have been investigated with deep-level transient spectroscopy (DLTS), isothermal transient spectroscopy (ITS) and energy-resolved DLTS. The effect of thermoemission (TE) enhancement in external electric field was found and the dependence of the TE activation energy reduction as a function of the filling grade was obtained for these states. A new model of dislocation-strain-related Poole-Frenkel effect that accounts for the own electric field of internal charge of dislocation line is suggested and compared with the experimental data.

Introduction

In spite of the fact, that initially the method of deep level transient spectroscopy (DLTS) has been developed for the investigation of the electrically active point-like defects in semiconductors [1], in the following it was widely applied for the investigation of the extended defects as well. The spectra of such extended defects in silicon like transition metal precipitates and dislocations introduced by plastic deformation consist of the broadened DLTS peaks, which could not be described satisfactorily by the standard model developed for point-like defects (see [2] for review).

Peaks broadening was explained as a result of the precipitates- and dislocations-related defect states spreading over a certain energy range $N(E)$. Another model assumed that the point self-induced defects and/or impurities are distributed around the dislocation line forming the so-called defect cloud. The first model leads to a symmetrical broadening of the DLTS peak which can be described by a Gaussian distribution centered around a mean value E_{a0} [3]. In the latter model, the energetic positions of the impurity levels in the clouds are shifted due to the influence of the dislocation elastic strain field, giving rise to the appearance of a low-temperature tail [2].

On the other hand, electron paramagnetic resonance EPR measurements have not identified the defects associated with density of states $N(E)$ in plastically deformed Si. All detected EPR active defects in Si with dislocations were ascribed either to the point-like defects in dislocations core or to the deformation-induced point defects [2]. These experimental findings of EPR measurements seem to be in conflict with the conclusions drawn from DLTS data analysis and this raises the question as to whether the fundamental ideas about the interpretation of extended defects electronic properties are really correct.

Recently, by investigation of the regular dislocation networks (DN) produced by Si wafer hydrophilic bonding we have found a strong field enhanced hole thermoemission for the shallow dislocation-related band located near the top of the valence band which obeyed square root dependence on the electric field (Poole-Frenkel effect, PFE) [4-5]. The values of the Poole-Frenkel coefficient were found to be different in samples with different DN structures and to exceed the theoretical value for the Coulomb potential. The presence of PFE-like dependence for hole thermoemission indicates that the states responsible for shallow dislocation-related bands are situated within an attractive potential for the holes that is inversely proportional to the distance from the trap. The dislocation deformation potential is also inversely proportional to the distance from the dislocation core. The theoretical calculations of PFE due to presence of 60° dislocation was found to be in a good agreement with experimental data on p-type samples [4].

Here we report for the first time about the observation of dislocation-related PFE in the n-type Si samples with DN. Detailed comparison of the new results with those obtained previously for p-type bonded samples [4-5] led us to the conclusion that the own dislocation charge has a significant influence onto the emission process.

Samples and Experimental Details

The sample for the investigations was fabricated by hydrophilic bonding of (100)-oriented silicon wafers of n-type conductivity doped to 10^{14} cm^{-3} with phosphorus. Details on the bonding procedure and oxide layer dissolution were described in [6]. Dislocation network (DN) forms at the bonding interface due to the mutual misorientation of the two wafers. In general, the twist component causes a square network of pure screw dislocations, while the tilt component is compensated by a periodic array of 60° dislocations.

Interdislocations distances were determined by TEM measurements. The most of the results presented here were obtained on n-type sample with the period of the screw dislocations of about *16 nm* and with the mean distance between 60° ones of around *42 nm*, so this sample is labeled as n-16/42. Bonding interface is lying parallel to the front surface at the depth of *~160 nm*, being thus inside the space-charge region (SCR) of Schottky diode even at zero applied bias voltage. The experimental results obtained on this n-type bonded sample are compared with the results obtained on analogous n- and p-type bonded samples produced by the same hydrophilic bonding method but with the different interdislocation distances, which are encoded in their notations.

To produce Schottky contacts for electrical measurements, 100 nm-thick gold dots with *1.5 mm* diameter were evaporated on the oxide free front surface of n-type samples. Ohmic contacts were prepared by rubbing of AlGa on the rear side of the samples. DLTS and isothermal DLTS (ITS) measurements were performed by means of transient Fourier spectroscopy system DL-8000 (Accent) equipped with the closed cycle cryostat.

Experimental Results

Dislocation-related Poole-Frenkel effect Figure 1a represents the set of DLTS spectra recorded with different reverse bias voltages U_r and a forward filling pulse voltage of U_p=*1,4 V*. At low U_r voltages a broadened rectangular-shaped DLTS peak with a very flat top was detected. With the increase of the applied reverse bias the right shoulder of this peak shifts towards the lower temperatures, thus, indicating the enhancement of carrier thermoemission from the shallow traps with the increase of external electric field in the depletion region of Schottky diode. Another particular feature of the peak is the shift of the left shoulder towards the higher temperatures with reverse bias increasing. As a result, the DLTS band is narrowed, peak shape becomes more cuspidal with simultaneous growth of the amplitude.

Detailed examinations of the electric field influence onto carrier thermoemission from the shallow traps were performed by means of ITS measurements (see [4] for details) whose spectra are not shown for brevity. The advantage of the ITS method over DLTS is that by measuring the ITS spectra at different reverse bias voltages one may trace the variation of electron emission rate e_n with the electric field at properly chosen temperature directly, without the determination of activation enthalpies E_a from Arrhenius plot data that was not possible in our case due to the particular behavior of DLTS peak. Figure 1b shows the dependences of the logarithm of emission rates for shallow traps as obtained from ITS spectra on the square root of electric field for n-16/42 sample, as well as for the n-6/37 sample and for two bonded samples of p-type conductivity p-8/27 and p-/60 (in the latter sample DN consisted of the rows of parallel 60° dislocations separated by the distances of about *60 nm*) from our previous articles [4-5]. The slope of the curves defines the PFE coefficients β which are also listed in the legend of Fig. 1b (in $cm^{1/2}$ $V^{1/2}$ units).

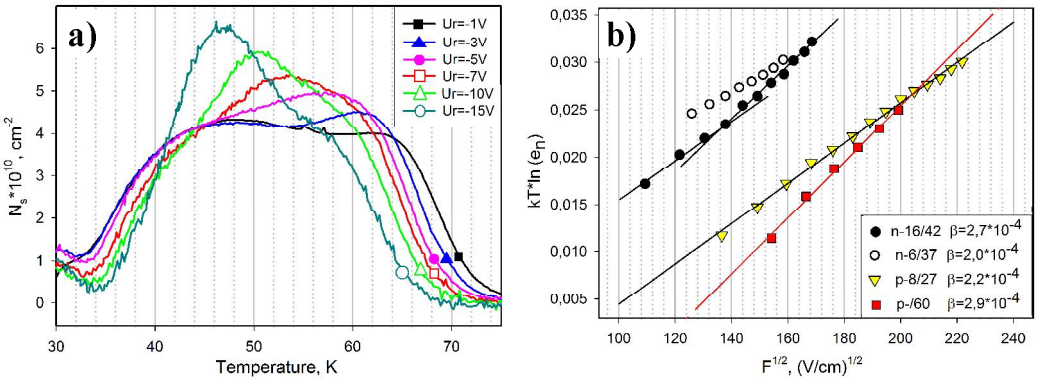

Figure 1. a) DLTS spectra of n-16/42 sample measured with different reverse bias voltages *Ur* as shown in the legend. Refilling pulse voltage was U_p=*1,4V*, pulse duration *1ms*, rate window period t_w=*200ms*. b) *kT*-corrected logarithms of emission rate as the functions of square root of electric field *F* for low-temperature DLTS peaks in n- and p-type bonded samples. The symbols correspond to the experimental data obtained from the position of ITS peaks, the lines represent the best linear fits.

In contrast to the simple linear dependences obtained for p-type samples, those derived for n-type samples could not be approximated by the single straight line, showing rather super-linear dependence with the slope coefficient β increasing with electric field, i.e. with U_r bias. Best linear fit for the high electric field parts gives β =2,7*10^{-4} for n-16/42 sample and β =2,0*10^{-4} for n-6/37.

Energy for electron thermoemission as a function of the state occupancy degree DLTS spectra for n-16/42 sample obtained by the variation of the magnitude of the filling pulse voltage U_p are presented in Figure 2a. The detectable DLT-spectrum appeared when the forward filling pulse voltage reached the level U_p=*0,5 V*, showing a small single maximum at T=78 K. At U_p=*0,6V* this initial single peak - along with the growing of its magnitude - shifts towards the higher temperatue of T=81K and the additional peak appeared on the left peak side (marked as I and II in Fig. 2a). The increase of the pulse voltage from *0,6 V* till *0,8 V* led to the subsequent growth of the signal magnitude accompained with the shift of the DLTS peak position towards the lower temperatures whereas the high-temperature side of the peaks almost coincided. Such a behavior was observed previously [5] in p-type bonded samples for the shallow dislocation related states in the lower part of band gap and, according to the criteria developed in [2], was attributed to "band-like states", i.e. to a band of electronic state with a rapid interstate exchange. Further increase of the pulse voltage till *1,4-1,5 V* led to the broadening of the peak from the low-temperature side keeping the magnitude nearly the same. No variation of the DLTS peak shape was observed at further increase of the pulse magnitude.

In order to define the exact energy position of the shallow dislocation-related states with respect to the conduction band we utilized the fact that under application of forward bias voltages U_f our structures behave similar to the grain boundaries or MIS structures where the filling grade of the interface traps is controlled by the potential at the interface. Thus, the method of so-called "energy-resolved DLTS" (ER-DLTS) [7] could be applied. In this method the Fermi level position corresponding to the bias voltage U_f controls the lower energy level till which the traps can be emptied after the application of a refilling pulse (see Fig. 2c). Keeping the difference between the pulse and the bias voltages small (*ΔU=50 mV*), the interface traps can be filled in the narrow energy interval.

The results of our ER-DLTS measurements are presented in Fig. 2b: a set of narrow DLTS peaks which shapes corresponded well with the theoretically predicted for the emission from single levels. Besides, their temperature ranges passed exactly between the right- and the left- shoulders of the broad DLTS peak obtained with U_p=*1,4 V*.

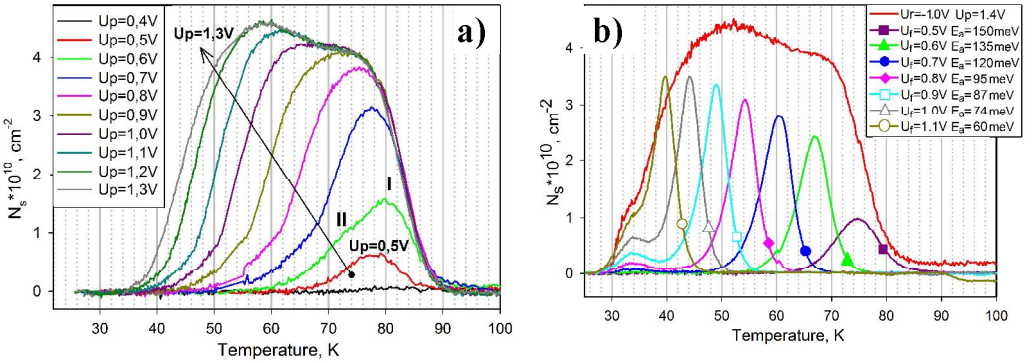

Figure 2. a) Variations of low-temperature DLTS peak in n-16/42 sample with increase of the pulse voltage U_p. Reverse bias U_r=*-1V*, pulse duration *1 ms*, rate window *1,3 ms*. b) Set of DLTS spectra measured with forward bias voltages U_f (shown in the legend) and filling pulse height of ΔU=*50 mV*. For comparison DLTS spectrum measured with U_r=*-1 V* and U_p=*1,4 V* is shown, too. c) Band diagram of the forward biased n-type Schottky diode with the DN lying inside the SCR. Fermi level is pinned by the shallow traps and its position at the bonding interface defines their filling grade.

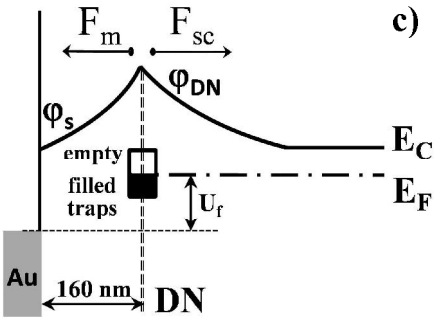

The values of their activation enthalpies E_a determined from the Arrhenius plots shown in the legend Fig. 2b vary from E_c-*150 meV* down to E_c-*60 meV*. Note, that the sharp turn of DLTS signal at 35-40 K is caused by the free carrier freeze-out, thus making it impossible to estimate the energy position of the lower edge of the shallow DN-related band precisely. One should also note that the magnitude of ER-DLTS peaks does not reflect the density of states, see [7] for details.

Discussion

The results of this work revealed the presence of PFE for the shallow dislocation-related states located near the bottom of the conduction band in n-type bonded samples. This fact, in addition to the previous observation of PFE for the shallow dislocation-related states located near the top of the valence band in p-type bonded samples, leads to an assumption that PFE is a general property of dislocation-related states.

Careful examination of the data obtained on different n- and p-type samples with DNs of different microstructures showed that other common features of DLT-spectra of shallow dislocation-related states are: (i) the broadening of the standard DLT-spectrum and the lowering of the thermoemission energy of ER-DLTS with the increase of the state filling grade, (ii) low temperature shift of high-temperature shoulder accompanied with the high-temperature shift of low-temperature shoulder of DLT- spectra observed with increase of external electric field, (iii) variation of PFE-coefficient value β in different samples and its increase with the increase of electric field in n-Si samples. In the following we will try to explain these particular features suggesting a new, more general model of the field-enhanced thermoemission from the dislocation related states that takes into account the own electric field of internal charge of dislocation line.

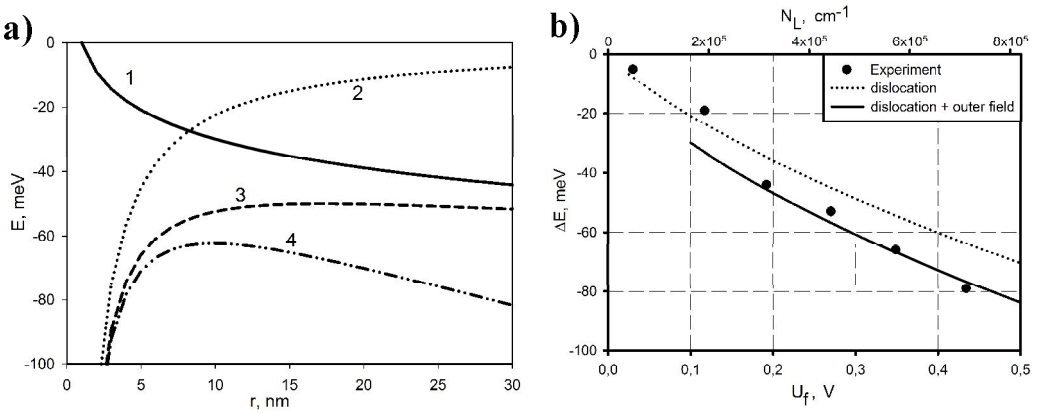

Figure 3. a) Variations of the potentials with the distance r from the DN plane (1) Coulomb potential of the charged line, (2) dislocation deformation potential, (3) sum 1 + 2, (4) sum 1 + 2 + external electric field of 10^4 *V/cm*. b) The reduction of activation energy for electron thermoemission from the local electronic states in the core of 60° dislocation as a function of number of electrons in the dislocation core and of applied forward bias to the Schottky diode with the bonded interface at the depth of *160 nm*: dotted line – was calculated according to the model of negatively charged dislocation line with an attractive dislocation deformation potential; solid line – the same but with adding of outer electric field of the diode; black dots – the data of energy resolved DLTS.

The own electric field due the non-screened Coulomb potential of dislocation line (Fig. 3a, curve 1) can be written as

$$\phi_l = -\frac{qN_l}{2\pi\varepsilon}\ln\frac{r}{r_{core}} = -\frac{qN_sD}{2\pi\varepsilon}\ln\frac{r}{r_{core}} \tag{1}$$

where q is elemental charge, ε is dielectric constant, N_l is the number of electrons per length unit of dislocation, r is the distance from dislocation, r_{core} is the radius of charged core, N_s is the averaged density of the electrons per area unit, D is the interdislocation distance in the bonded interface. The attractive part of deformation potential around the dislocation (Fig.3a, curve 2) can be written as

$$\phi_d = -\frac{A(\theta)}{r} \tag{2}$$

where $A(\Theta)$ is the expression derived from deformation potential theory containing a combination of deformation potential constants for silicon and angular dependence of deformation around the dislocation [4].

The potential of external field of the Schottky diode F_0 can be expressed by the standard formula of Schottky diode theory and is not cited here for brevity. By applying convenient procedure of PF theory (see for details [4]) we calculated the radius of the potential maximum equating to zero the total effective field:

$$F_\Sigma = F_0 + F_d + F_l = F_0 - \frac{A(\theta)}{r^2} + \frac{qN_l}{2\pi\varepsilon r} = 0 \tag{3}$$

then, calculate the reduction of the potential energy for electron thermoemission as the function of dislocation line charge density and the applied electric field (Fig.3a, curves 3 and 4). The results of the calculations together with the experimental data on ER-DLTS are presented in Fig. 3b. Experimental values of the line charge of the dislocations at the bonded interface were obtained as interface charge density per square cm from our capacitance-voltage data multiplied by the interdislocation distance obtained from TEM.

Careful examination of Fig. 3b reveals that at low bias voltages the experimental points coincide well with the theoretical curve calculated for the own dislocation field only, whereas with the further increase of forward bias (i.e. with the increase of the dislocation line charge) they become closer to the theory that takes into account the external electric field as well. Note, that the theoretical curves were obtained without any fitting variables by taking as an input parameters the literature values of deformation potentials for X-band in Si, the experimentally determined depth of the interface and a reasonable value for r_{core}=*1 nm*.

With the assumption of the dislocation-related internal PFE it is possible to explain all of the features (i-iii) listed above:

(i) the "band-like" behavior of DLTS line can be the result of the thermoemission barrier lowering with the increase of the dislocation charge;

(ii) there are two symmetric orientations of 60^0 dislocations with respect to the DN plane: with attractive deformation potential directed predominantly towards the metal and to the bulk (see [4]). These two types of dislocations are under the actions of both their own and external electric fields. Just after the application of the filling pulse the DN-interface charge density is so high that the external electric field in the top layer of the structure exhibits an inversion with respect to its bulk part (fields F_m and F_{sc} in Fig. 2c) and the lowering of the potential barrier for electrons thermoemission occurs towards the both sides of DN plane. With the increase of the reverse bias the field F_{sc} increases but F_m in the top layer decreases, thus the emission to the left side of DN plane occurs via higher potential barrier leading to the high-temperature shift of the low-temperature shoulder;

(iii) in the presence of the own electric field of dislocation the impact of external electric field on the carrier thermoemission would increase with increase of the applied reverse bias U_r giving rise to the superlinear dependence observed for n-type samples. Explanations in more detail will be published elsewhere.

Summary

We investigated the impact of externally applied voltage on thermoemission of electrons from the shallow dislocation-related states located on dislocation network produced by wafer bonding. An enhancement of carrier thermoemission under application of both reverse and forward bias voltages was found. A new model of the field-enhanced thermoemission from dislocation related states due to the presence of attractive dislocation deformation potential that also takes into account the own electric field of internal charge of dislocation line is suggested. A good quantitative agreement between the theoretically calculated and experimental data derived from the energy-resolved DLTS measurements was established. Other particular properties of the obtained DLT-spectra can be explained qualitatively in the frame of the suggested model.

References

[1] D. V. Lang, J. Appl. Phys. 45, (1974) 3014.

[2] W. Schröter and H. Cerva, Sol. State Phenom. Vols. 85-86 (2002) 67.

[3] P. Omling, L. Samuelson, H.G. Grimmeiss, J. Appl. Phys. 54, (1983) 5117.

[4] M. Trushin, O. Vyvenko, V. Vdovin, M. Kittler, Journal of Physics: Conference Series 281 (2011) 012009.

[5] I. Kolevatov, M. Trushin, O. Vyvenko, M. Kittler, O. Kononchuk, phys. stat. sol. (c) 10(1) (2013) 20-23.

[6] O. Kononchuk, F. Boedt, F. Allibert, Sol. State Phenom. Vol. 131-133 (2008) 113-118.

[7] N.M. Johnson, J. Vac. Sci. Technol. 21(2) (1982) 303.